Final Technical Report

A Hydrodynamic Model of Oil Containment by a Boom : Phase I

Submitted to :

U.S. Department of Transportation
Attn : John Putukian
Volpe National Transportation Systems Center
55 Broadway, Cambridge, MA 02142-1093
DOT Grant No. DTRS-5794-G-00076

August 15, 1994-February 15, 1996

Submitted by :
S. T. Grilli, Z. Hu, and M.L. Spaulding

Department of Ocean Engineering
University of Rhode Island
Narragansett Bay Campus, Narragansett, RI 02882

June 10, 1996

Contents

1 Introduction and literature review **1**
- 1.1 Overview of the Problem . . . 2
- 1.2 Literature review . . . 5
  - 1.2.1 Qualitative studies . . . 6
  - 1.2.2 Some related phenomena . . . 9
  - 1.2.3 Experimental results . . . 10
  - 1.2.4 Numerical Models . . . 13
- 1.3 Statement of the problem . . . 17

2 General equations for the dynamics of vortex sheets **22**
- 2.1 Velocity-vorticity equations for a vortex sheet . . . 22
- 2.2 Piecewise constant vorticity and point vortices . . . 23
  - 2.2.1 Point vortices . . . 23
  - 2.2.2 Piecewise constant vortices . . . 24
- 2.3 Vorticity dynamics equations for a vortex sheet . . . 25
  - 2.3.1 Circulation on a vortex sheet . . . 25
  - 2.3.2 Rate of change of circulation for a vortex sheet . . . 26
  - 2.3.3 Acceleration-rate of change of circulation equations for a vortex sheet 28
  - 2.3.4 Semi-infinite vortex sheets . . . 31

3 Equations for numerical model **34**
- 3.1 General model equations . . . 34
  - 3.1.1 Principle of computations . . . 34
  - 3.1.2 Non-dimensional model equations . . . 36
  - 3.1.3 Computation of acceleration terms in explicit scheme . . . 38
  - 3.1.4 Computation of geometry and tangential derivatives . . . 39
  - 3.1.5 Node regridding . . . 40
- 3.2 Computation of initial steady state slick shape . . . 42
  - 3.2.1 Principle of initialization . . . 42
  - 3.2.2 External flow calculation . . . 44
  - 3.2.3 Iterative calculation of slick shape . . . 45
  - 3.2.4 Friction coefficient calculation . . . 47

4 Model test and validation **48**
4.1 Principle of model validation 48
4.2 Periodic KH instability 49
4.2.1 Overview 49
4.2.2 Governing equations 50
4.2.3 Calculation of self-induced velocity contributions for piecewise constant element 52
4.2.4 Initial vorticity distribution 53
4.2.5 Summary of computational techniques 53
4.2.6 Computational results for interface evolution 54
4.3 Deep water headwave instability 59

5 Conclusions and future developments **64**

Bibliography **67**

Abstract

This report presents results obtained at the University of Rhode Island, Department of Ocean Engineering, as part of a research project titled : "A hydrodynamic model of oil containment by a boom : Phase I". This project was supported by Grant No. DTRS-5794-G-00076 of the Department of Transportation (United States Coast Guards District No. 1) FY 1994 Oil Pollution Research Grant Program. A 50% budget match was provided by the University of Rhode Island.

This project officially started on August 15th, 1994, originally for a period of one year, but was extended until November 15th, 1995 due to a late start. A second year grant was obtained as part of the same program with FY 1995 funding and is currently in progress. This report only covers developments and computations carried out during the first year of the project, using a numerical model hereafter referred to as *Phase I model*.

An extensive literature review was first conducted for problems of interfacial instabilities between two fluids and, more specifically, for oil containment failure problems. Based on this review, a hierarchy of modeling strategies was proposed both for this project and for its possible extensions. These are hereafter referred to as Phase I, II and III models. Phase I model was developed, implemented, and tested as part of the FY94 project. The Phase II model is being developed as part of the FY95 project. A summary of the literature review and proposed modeling strategies is given in Chapter 1.

The Phase I model is based on using piecewise-constant vortex sheets (VS) to represent the dynamics of the oil-water interface in a contained oil slick. Both finite and semi-infinite VS's are used in the model. Biot-Savart's law is used to calculate flow velocities induced by vorticity distributions in the VS's. Self-induced velocity contributions of VS elements are explicitly calculated in the model. This represents a significant improvement compared to most earlier approaches proposed for modeling interfacial instability using VS's. An evolution equation is derived for updating VS's vorticity which includes the effects of inertia, gravity, oil and water density differences, and surface tension at the interface. VS dynamics equations used in Phase I model are detailed in Chapter 2.

Higher-order modeling of the VS's geometry is introduced, based on 4th-order sliding polynomials and cubic spline elements, to accurately calculate tangential derivatives needed along VS's for expressing the evolution equation. Vortex regridding techniques are introduced and tested in the model to control model resolution in specific interfacial regions. Both implicit and explicit time updating schemes are developed, implemented, and tested for calculating new positions and vorticity of VS's at a later time. In the model, the initial quasi-steady shape of the oil slick is calculated based on satisfying both kinematic and dynamic conditions along the interface, for a flow velocity below the critical threshold. The numerical implementation of the Phase I model is detailed in Chapter 3.

Chapter 4 presents application cases used to test and validate the model. The idealized case of a periodic Kelvin-Helmholtz instability is first presented to test and validate the principal numerical algorithms. The pure headwave instability case (i.e., without a boom) is then presented. Model calculations are found to be both stable and accurate, without need

for smoothing or for other transformations of model outputs often used in earlier studies. In all cases, computations of interfacial instabilities can be pursued for a longer time than with earlier approaches. Computational results are qualitatively similar to other published material.

Applications of the model to more realistic cases for which experimental data is available or will be performed, will be addressed in Phase II of this project.

Chapter 1

Introduction and literature review

The present project is aimed at developing a hydrodynamic model of *oil containment* by a boom and to use the model to investigate oil containment failure mechanisms identified and studied in both the research and professional community over the past 25 years. In the objectives originally proposed for this project, it was envisioned that this model and its future improvements would help us gain fundamental insight into oil containment failure mechanisms and outline strategies and methods to limit the occurrence or the intensity of these failures in actual field situations. Due to both its more catastrophic nature and its dominance for high viscosity oils found in actual spills, the failure mode referred to as *critical accumulation* was selected as the main object of the study. Three technical tasks were proposed : (i) numerical model selection and design; (ii) model testing and validation; and (iii) application to critical accumulation failure.

Task (i) was achieved by conducting an extensive review and analysis of the oil containment literature, including theoretical, analytical, and numerical aspects (Subramanya and Grilli, 1994). At the conclusion of this review, a tentative numerical modeling strategy was identified, hereafter referred to as the *Phase I model* and a hierarchy of models was also proposed for future developments (hereafter referred to as Phase II and III models).

In this report, we present key elements of the literature review in Chapter 1. In Chapters 2 and 3, we detail and discuss equations and numerical procedures selected for the implementation of the Phase I model. Finally, in Chapter 4, we conduct the validation and testing of the Phase I model (Task (ii)) both for a purely interfacial instability problem (periodic Kelvin-Helmholtz instability) and for a headwave instability (i.e., without a boom). Detailed results for more realistic problems including critical accumulation failure of oil containment by a boom (Task (iii)) will be addressed in Phase II of this project, using an improved version of the model [1]. Preliminary qualitative results, however, are given in Section 5 that illustrate computations with the present model for a case involving both a headwave instability and a boom.

[1] It was indeed found while conducting this study that a more accurate numerical model than originally anticipated is needed to realistically address such problems.

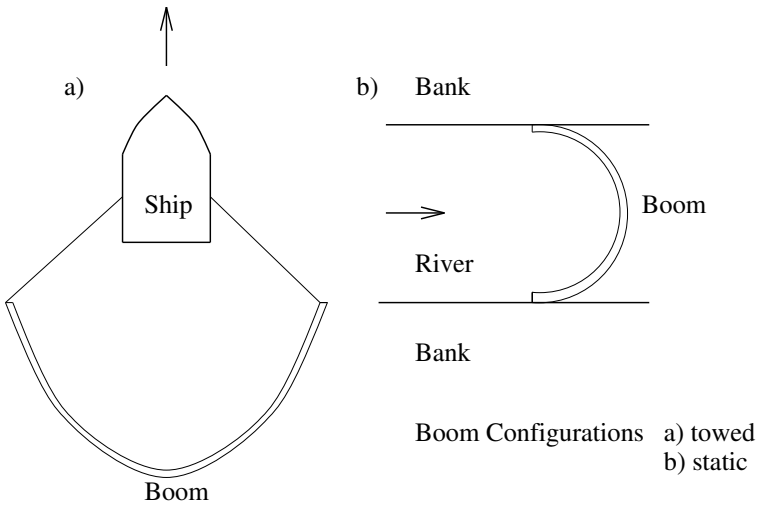

Figure 1.1: Planview of typical set-up for oil containment by : (a) a towed boom (ocean); or (b) a static boom (river).

1.1 Overview of the Problem

Oil booms or barriers are one of the most commonly used techniques to collect and contain oil on the sea surface, or to protect specific areas against slick spreading. In the collecting mode, such floating boom systems are usually set–up on the free surface in a U configuration and towed towards the oil slick.

The containment of oil by a boom is illustrated by the sketches in Fig. 1.1 which correspond to both an *ocean situation* in which a boom is towed by a boat at speed U over an essentially non-moving water mass (zero current), and a *river situation* in which a fixed boom is placed across a river flow with current U. In both cases, the boom takes a catenary shape and oil accumulates inside the boom. Maximum accumulation of oil occurs at the catenary's apex where maximum relative water velocity also occurs. Considering this and the small curvature of the boom geometry around the apex point, it is acceptable as a first approximation to simplify and analyze this essentially three-dimensional problem as a *two-dimensional* one in the vertical plane intersecting the boom at the catenary's apex (Fig. 1.2). It is also acceptable to assume that, for both cases in Fig. 1.1, the boom does not move and the water flows under the boom at a velocity U, equal to the relative boom-water velocity.

In order to collect as much oil as possible in the shortest possible time, it is desirable to have a tow velocity as large as possible. Various hydrodynamic instabilities at the oil–water interface, however, contribute to a fairly low practical limit on the tow velocity, on the order of 0.5 m/s.

For the idealized problem sketched in Fig. 1.2, observations show that interfacial waves start developing at the oil–water interface for relative current speeds, $U > U_{cr} \simeq 0.15$ m/s. For larger speed, these waves grow unstable and, in most cases, lead to substantial

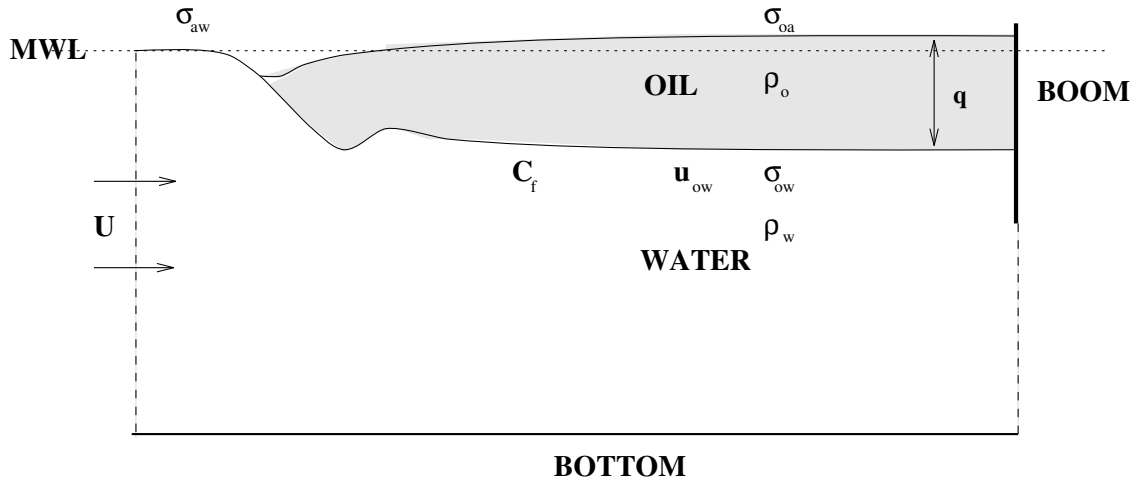

Figure 1.2: Sketch for initiation of oil containment failure by *critical accumulation*, with mention of important parameters : U, oil-water relative current velocity; $\mathbf{u}_{ow}$, oil-water relative velocity; ρ_o, ρ_w, oil and water density, respectively; σ_{ow}, σ_{oa}, σ_{aw}, interfacial tension coefficients for oil-water, oil-air, and air-water, respectively; C_f, oil-water interfacial friction coefficient; q, oil slick depth at the boom; MWL, Mean Water Level.

or even total loss of oil by entrainment of oil particles under the boom (e.g., Wicks, 1969; Wilkinson, 1972,1973; Lau and Kirchifer, 1974; Agrawal and Hale, 1974). In the literature, such instabilities are referred to as *boom containment failure modes* and three main types of containment failures have thus far been identified. These are defined in the following,

- **Drainage Failure** An increase in relative oil-water velocity U leads to an increase in interfacial friction stresses, causing a shortening and a thickening of the slick. An increase in slick thickness beyond the barrier draft d leads to drainage failure.

  Cross and Hoult (1971) studied the steady–state profiles of contained oil slicks and formulated an equation for the maximum slick length l as a function of barrier draft d,

  $$l = \frac{156.25\, g\,(1-s)}{U^2}\, d^2 \tag{1.1}$$

  where, $s = \rho_o/\rho_w$ (ρ_o being the oil density and ρ_w the water density). This equation is applicable only for low current speeds and smooth oil-water interfaces. If slick length is larger than l, containment failure will occur by drainage under the boom.

  For larger current speed, the oil-water interface is no longer smooth (see below) and the interfacial friction coefficient C_f increases. For such cases, Delvigne (1989) finds empirically that maximum slick length depends on oil volume Q as, $l \propto Q^{2/3}$.

- **Entrainment Failure** For high relative oil–water velocities and low viscosity oils ($\nu_o < 3,000$ cs), large interfacial stresses occur and induce shear instabilities of the

oil-water interface. Such instabilities are characterized by the formation of small fast-moving interfacial waves which, for sufficiently large U (on the order of 0.25 m/s), may become unstable and break, and lead to subsequent entrainment of oil droplets in the underlying flow. The droplets either reattach to the slick (if the slick is long enough) or pass under the barrier, leading to *progressive* containment failure by droplet entrainment.

Significant work on droplet entrainment was done by Agrawal and Hale (1974), Wilkinson (1972,1973), and Leibovich (1976).

Note that drainage and entrainment failure may simultaneously occur in some situations.

- **Critical Accumulation** Prior to Delvigne's (1989) experiments, entrainment failure was thought to be the primary dynamic failure mode for contained oil slicks. Delvigne, however, showed that for oils with large viscosities, $\nu_o \geq 3,000$ cs, another, more catastrophic, failure mechanism occurs at a lower velocity U than the other two modes. Previous studies did not reveal this failure mechanism because the oil viscosities used in the experiments were too low.

  In this failure mode, referred to as *critical accumulation*, the oil–water interface, when exposed to a relative oil–water flow velocity exceeding a certain critical velocity, $U_{cr} \simeq 0.15$ m/s, develops slow-moving large scale oscillations which eventually cause all of the oil to escape under the barrier, *independent* of barrier draft d.

  A more detailed analysis of Delvigne's experiments reveals that critical accumulation is characterized by the formation of a headwave at the front of the slick (Fig. 1.3) which grows in amplitude as a function of time and propagates downstream towards the boom, causing the slick to become both shorter and thicker and eventually leading to almost total loss of oil under the boom. Quite remarkably, for large enough viscosity, Delvigne's experiments showed a lack of dependence of U_{cr} on oil viscosity ν_o, density difference, $\Delta\rho_{ow} = \rho_w - \rho_o = \rho_w(1-s)$, oil volume Q, and water depth h.

  Finally, it should be emphasized that, due to weathering and emulsification, real slicks can quickly reach large viscosities, on the order of 10,000 cs (e.g., Johnston *et al.*, 1993) and, hence, their containment by a boom is likely to fail by critical accumulation, for tow velocities beyond the critical value.

Of the three failure modes mentioned above, for high viscosity oils that are found in actual slicks, critical accumulation seems to be the dominant failure mode for large tow or current speeds[2].

[2]Note that, in addition to these failure modes which occur in calm weather, the effectiveness of the boom in containing oil can be severely limited by the hydrodynamic behavior of both the boom and the slick under extreme weather conditions that may create high seas. These factors will not be considered in the present study.

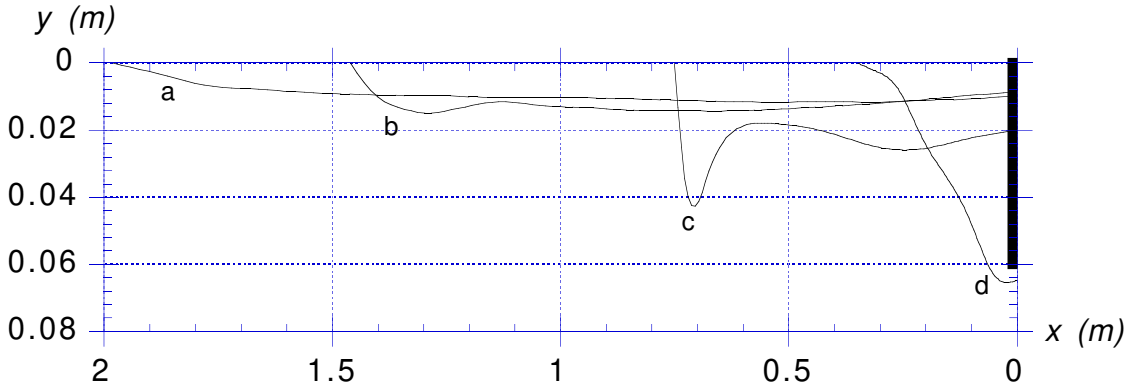

Figure 1.3: Experimental shapes of oil slicks measured in Delvigne's (1989) experiments with Arabian light emulsion ($\nu_o = 2,300$ cs) for relative oil-water velocity U = a : 0.065; b : 0.095; c : 0.128; and d : 0.145 m/s. The figure shows the increase in size of the headwave and the shortening of the slick as U increases from curve a to c and, finally, the failure by critical accumulation with the oil slick draining under the boom in curve d.

Many experimental and theoretical studies were pursued in the 1970's to understand the physics of oil containment by a boom and circumstances leading to containment failure. More recently, there has been a renewed interest in studying the problem and a few attempts were made to better understand the problem by the use of numerical modeling tools. In Section 1.2, we present a literature review of the oil containment problem including qualitative, experimental, and numerical studies. It will be shown, in particular, that interfacial waves occurring during the failure modes discussed above are both initiated and sustained by *shear instability* at the oil-water interface, usually referred to as a *Kelvin-Helmholtz (KH) instability*. Hence, modeling KH instability in the context of oil containment by a boom, will be one of the main objectives of the present study. This will be detailed in Section 1.3.

1.2 Literature review

Research in the area of boom–slick–current interaction has primarily been experimental, with few researchers adopting theoretical approaches to the problem. Recently, efforts have been made to study the phenomenon using numerical methods but with limited success.

In the following sections, in an attempt to better understand the physics of the problem and formulate an effective modeling strategy, the existing literature has been reviewed and significant studies summarized based on the approach adopted by the researchers, namely *qualitative, experimental, theoretical* or *numerical*.

1.2.1 Qualitative studies

Wilkinson

Wilkinson (1972) studied the effect of hydrodynamic forces on an oil slick contained in a two–dimensional channel and showed that, even for inviscid flows, the slick thickness would be finite in the presence of a current.

He conjectured that the oil slick can be divided into *two zones* : (i) one in which dynamic forces are dominant; and (ii) the other in which viscous effects dominate. The relative extents of each of these zones were determined by examining the orders of magnitude of the forces acting on the slick. The force balance in the frontal zone (headwave) was examined by equating pressure forces acting at sections upstream of and across the slick to the change in momentum of the flow between the two sections (viscous forces were assumed negligible). The following conclusions were drawn regarding contained oil slicks,

- The *frontal thickness* of a slick will never be greater than approximately one–third of the stream depth.
- Containment failure occurs when the *Froude number* of the flow upstream of the slick exceeds a critical value (0.498–0.527).

The frontal region of the slick is thus analogous to a hydraulic jump in which the head loss or rate of energy dissipation can be defined in terms of an upstream Froude number.

When the slick is of considerable length and overlies deep water, its final thickness may greatly exceed the frontal thickness. The form of the frontal zone is determined largely by interfacial stresses and interfacial slopes, which typically vary between 0.0005 and 0.004 (Cross and Hoult, 1970) and imply a more or less uniform interfacial stress.

The slick length and therefore the quantity of oil that can be contained by a barrier are also limited and depend upon the Froude number of the flow upstream of the slick and the interfacial and boundary stresses acting beneath the slick. A strong dependence of the interfacial friction coefficient C_f on the Reynolds number **Re** of the underlying flow is observed.

Leibovich

Leibovich (1976) studied *entrainment failure* of oil slicks and suggested that it was caused by the breaking of Kelvin–Helmholtz (KH) interfacial waves. Using linear stability theory, Leibovich demonstrated that thin slicks are more stable than thick slicks (unlike earlier conclusions by Jones, 1972). The surface tension at the oil–air interface, σ_{oa} was found to have a stabilizing influence on the development of interfacial waves in thin slicks.

Drazin's (1970) theory of *finite amplitude* KH waves was used to explain the departure of experimental values of U_{cr} from those predicted by the linear stability analysis. Stabilizing factors leading to the formation of equilibrium finite amplitude KH waves are buoyancy, $\Delta\rho_{ow}$, and surface-tension at the oil–water interface, σ_{ow}.

The formation of the *headwave* and its role in entrainment failure was also considered in this study. Three possible causes were proposed to explain the initiation of entrainment failure at the headwave,

- Benjamin (1968) studied gravity currents in cavity flows and observed *headwave instability* downstream of the point of maximum thickness (an inviscid theory, however, was used [3]).
- Adverse pressure gradient on the lee of the headwave, contributing to separation and eddy formation.
- The locally high values of the relative oil-water velocity at the interface, $\boldsymbol{u}_{ow}$, at the point of maximum thickness of the slick may cause the early *separation of oil droplets*, even though $\boldsymbol{u}_{ow}$ may be smaller than the critical value elsewhere along the slick.

Milgram and Van Houten

Milgram and Van Houten (1978) studied the respective magnitudes of *frictional and pressure forces* along the oil–water interface using a combined theoretical–experimental approach.

In this study, potential flow theory is assumed for the water and the shape of the oil–water interface is measured in experiments. Dynamic pressure due to the underlying flow is calculated on the interface using a Green's function approach. An equation relating interfacial shape, dynamic pressure, and shear stress is derived to calculate the shear stress distribution and conclusions are then drawn about the relative effects of shear and pressure forces along the oil–water interface.

A more detailed discussion of numerical methods employed and results obtained in this study are given later in this review.

Di Pietro and Cox

Di Pietro and Cox (1980) showed the existence of a region at the very tip of the slick where *surface tension* is more important than gravity and viscous forces. This region is shown to be (physically) necessary to connect the monolayer (defined as the thin layer of oil preceding the slick) and the bulk of the slick. This is also an area where the interface slope is large.

The form of a slick upstream of a barrier is computed assuming : (i) small velocity variations across the oil layer; (ii) monolayer and bulk layer lengths much larger than capillary scale; (iii) small interface slopes; (iv) inertia effects are neglected in the oil slick; (v) negligible pressure variations in the underlying flow; (vi) laminar flow in boundary layers.

This theory is important from the current perspective as it forms a plausible starting point for numerical simulations. Initial conditions based on the analytical form can be

[3]Note that Milgram and Van Houten (1978) showed the importance of viscous shear along the slick interface and hence the selection of a purely dynamic approach may not be appropriate.

used as input to the proposed model and evolution tracked for increasing U. The excellent description of the oil–water–air junction will be important to prevent numerical instabilities from creeping in due to incorrectly posed initial conditions (see also Section 3.2).

Delvigne

Delvigne (1980) identified a third failure mechanism for oil slick containment by a barrier and called it *critical accumulation* (hereafter referred to as CA). CA appears to occur for oil viscosities, $\nu_o \geq 3,000$ cs and flow velocities $U \geq 0.15$ m/s. Prior studies considered oils where viscosities were too low and water depths too limited to reveal this mechanism. In his experiments, Delvigne used oil viscosities as high as 33,000 cs and flow velocities up to 1 m/s.

Oil viscosity considerably influences both the length and shape of a contained oil slick and the occurrence of interfacial instabilities. In fact, oil viscosity is a key parameter for the occurrence of any of the three modes of failure, in the range of flow velocities at which failure commences. In real oil spills, however, oil viscosity often rapidly increases as a result of weathering and emulsification. Whereas most crude oils and products originally have $\nu_o \leq 1,000$ cs, emulsification takes place within a few hours of the spill and results in a viscosity on the order of 1,000 cs. Continual weathering of slicks eventually increases this viscosity to the order of 10,000 cs and, in the long term, almost solid tar balls can be formed.

Oil slick behavior behind a barrier can be described as a function of viscosity ν_o and flow velocity U. Three different scenarios are possible,

- *Low viscosity oils* with $\nu_o \leq 400$ cs exhibit failure normally by the droplet entrainment mechanism. Increasing values of U result in shorter slick lengths and fast moving interfacial waves (due to KH instability) which become unstable at a certain velocity, leading to oil droplets being torn from the slick and passing under the barrier or reattaching to the slick further downstream.

- *Moderately viscous oils* with ν_o in the $400 - 3,000$ cs range normally have a smooth interface, with a headwave at the upstream edge of the slick. Slow interfacial waves develop at higher current velocities, and slick shortening and thickening take place (see Fig. 1.3). If the barrier draft is adequate to prevent drainage failure, droplet entrainment begins as a result of headwave instability.

- *Highly viscous oils* with $\nu_o \geq 3,000$ cs show smooth interfaces and the formation of a headwave. In long slicks, regularly spaced interfacial waves are observed downstream of the headwave, which appear to be almost stationary. Slick length gradually decreases with increasing U. At some critical velocity U_{cr} the slick collapses to a vanishingly small length and passes under the barrier, regardless of barrier draft.

1.2.2 Some related phenomena

Owing to the complicated nature of the modeling problem of an oil containment by a boom, researchers have attempted to compare the slick–water–boom interaction problem to other physical phenomena and gather insight from studies in those fields. Two phenomena, analogous to the present problem, are gravity currents and hydraulic jumps.

Gravity currents

A gravity current (or density current) is the name given to the phenomena characterized by the relative flow of fluids of differing densities past each other. A typical gravity current consists of a heavier fluid flowing over the bottom, displacing a fluid of smaller density. The front of the fluid progresses with nearly constant speed and is characterized by the existence of a large headwave, typically twice the height of the interface average depth, and an undulating turbulent downstream side indicative of some kind of wave instability and/or breaking. Further downstream, the interface becomes nearly horizontal. Typical instances of gravity currents in nature include the case of salt water intrusion into fresh water, turbidity currents, and meteorological cold-fronts.

Wicks (1969) first observed the similarity of our problem to an upside down gravity current and posed that results for gravity currents would be similarly applicable to the problem of a contained slick floating on water.

Benjamin (1968) studied gravity currents using inviscid fluid theory with simple extensions to account for dissipation. Two approaches were investigated, without and with dissipation. The salient features of his paper and relevant conclusions of his study are,

- The interface between two fluids is shown to be unstable to all possible stable disturbances.
- The existence of a headwave is shown to be impossible if the flow is energy conserving and its existence is thus linked to the dissipative process.
- An analytical solution for the interface, is derived using complex mapping and assuming only dynamic effects. An included angle of 60° at the front of the gravity current is deduced [4].

Hydraulic jumps

Wilkinson (1972) pointed out the similarity of the slick water interface to a hydraulic bore. Wei *et al.* (1995) studied undular bores at the ocean surface. These results, when turned upside down, are remarkably similar to interfacial profiles measured by Delvigne (1989) (see Figs. 1.3 and 1.4). Since the results for the undular bore were computed using a fully nonlinear potential flow model (i.e., a theory that does not include friction), it is reasonable

[4]Note that Milgram and Van Houten (1978) demonstrated the need to also consider viscous effects when computing interfacial profiles.

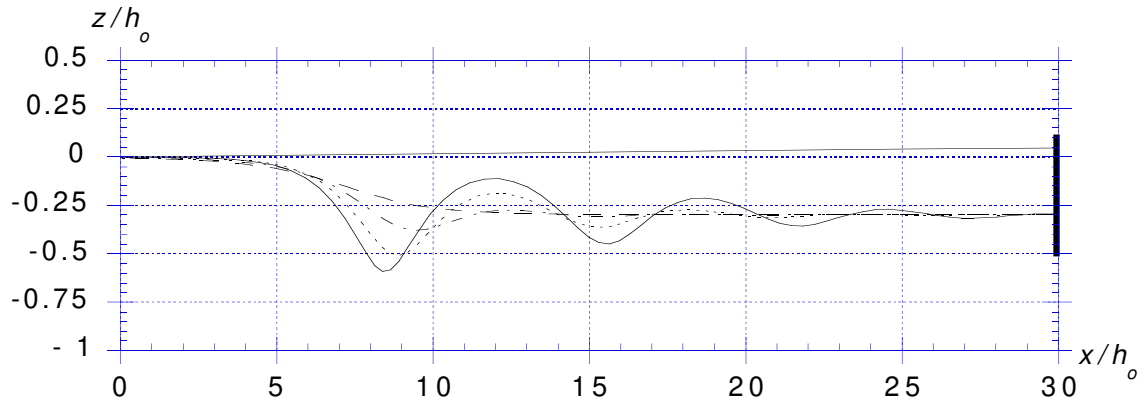

Figure 1.4: Qualitative similarity between headwave instabilities and the time development of an upside down undular bore calculated by Wei *et al.* 1995.

to infer that dynamic forces (i.e., boundary conditions on the oil water interface) dictate to a large extent the formation of the interfacial waves.

1.2.3 Experimental results

Following is a summary of significant experimental studies to date and their results that can provide a ready reference for the researcher in the field of current–slick interaction.

Milgram and Van Houten

In Milgram and Van Houten's (1978) study the *shape* of the oil–water interface in an oil slick was experimentally measured, for different oil characteristics and current speeds, and related by quasi-hydrostatic equilibrium equations to the friction coefficient and the dynamic pressure distribution along the interface (see Sections 1.2.4 and 3.2).

The experiments were carried out at MIT's precision flume (6.25 m by 0.61 m by 0.46 m), with an operating water depth of 0.53 m and a barrier draft of 0.175 m. Wall effects, shown to cause premature containment failure in the flume due to the generation of side vortices, were reduced by using a layer of rubberized horsehair on the upstream side of the barrier. Uniform current speeds were first established in the water before layering oil onto the test section and waiting for equilibrium. Equilibrium was reached in the slick after damping of waves moving back and forth in the oil was achieved. Since the speed of such waves is limited to $\sqrt{gq\,(1-s)}$, where q is the oil layer thickness, equilibrium in thin slicks was only reached after quite a long time, particularly since s varied between 0.804 and 0.88 in the experiments. Measurements of interfacial shape were directly made on the flume glass sidewalls, using photographic techniques. Smoothing of photographs of the interface was performed afterwards. Oil viscosity in the experiments varied between 3.61 and 125.36 cs and current speeds of 0.16 m/s to the upper limit of entrainment failure were tested.

The main experimental results obtained were as follows,

- The oil was found to move very slowly, with the formation of vertical circulation cells within the slick. This justifies assuming *quasi-hydrostatic pressure* in the oil for the theoretical analyses, particularly for high viscosity oils (see Section 3.2).

- Smooth interface shapes were only observed for $U \leq 0.20$ m/s. At higher velocities, interfacial waves developed. These were shown to be *KH instability* waves, owing to their constant phase speed and the formation of a headwave at the location of higher Reynolds numbers in the underlying flow.

- Leibovich's (1976) observation of increased stability for thinner oil layers was verified.

- The upstream end of the slick was marked by a visible ridge on the water surface, referred to as *Thoreau-Reynolds ridge*.

- A surface film formed upstream of the oil slick, referred to as the *monolayer* (Di Pietro and Cox, 1980). A boundary layer of water formed underneath the film, with the stress in the boundary layer being balanced by the surface tension gradient in the oil film.

- *Interfacial friction* was found to increase with increasing interfacial slope and current speed, and to have a strong dependence on pressure gradient.

- *Droplet entrainment* occurred due to the formation of large scale unstable KH waves on the interface. The rate of droplet entrainment increased with the water velocity $\boldsymbol{u}_{ow}$ directly below the interfacial boundary layer and with the thickness of the boundary layer. Thin boundary layers and high water speeds maximized droplet entrainment.

- Decreasing interfacial *surface tension* only had marginal effect on the interface geometry. Surface tension, however, was found important for the evolution of finite amplitude KH waves (Drazin, 1970). Increasing oil viscosity also helped damping the shorter waves occurring on the interface.

Delvigne

Delvigne (1989) primarily addressed the problem of containment of highly viscous oils ($\nu_o \geq 3,000$ cs) in nonlimiting water depths, for large values of U (up to 1 m/s) not addressed in prior experiments. He succeeded in demonstrating the occurrence of a new (dominant) failure mechanism, *critical accumulation*, and described the experimental results and the factors deemed to be important for this kind of failure mode.

Experiments were performed in two flumes with widths of 0.5 and 2.0 m, water depths ranging from 0.3 to 0.7 m and barrier draft from 0.07 to 0.13 m. Different oil types were used to obtain a continuous range of viscosity. Oil was poured on the water, current velocities were established, and slick length and form were measured. Different scaling rules were applied for different failure modes : (i) drainage failure was scaled using a Froude number

scaling, on account of its sensitivity to barrier draft and slick length; (ii) droplet entrainment and critical accumulation on the other hand were simulated using full scale, because of their dependence on viscosity and current speed.

The main experimental results obtained were as follows,

- The proportionality of maximum slick length for *drainage failure* to the square of the barrier draft (first proposed by Cross and Hoult, 1970; see Eq. (1.1)) was self evident in the results.

  For low current speed, maximum slick length was proportional to U^{-2} but for larger current speed, the interfacial friction coefficient C_f increases due to interfacial KH waves and maximum slick length was proportional to $Q^{2/3}$ (where Q is the oil volume per unit width of slick).

- Agrawal and Hale's (1974) postulated dependence of *critical velocity* U_{cr} for droplet entrainment failure on the Weber number was not supported by experimental results. Values of U_{cr} were also found to be lower than those observed by Agrawal and Hale. The trend of decreasing U_{cr} with increasing ν_o was substantiated.

- *Critical accumulation* always occurred in experiments for $\nu_o \geq 3,000$ cs and for current speeds greater than 0.15 m/s. Both entrainment and critical accumulation failures simultaneously occurred for 2,000 $\leq \nu_o \leq$ 3,000 cs.

- U_{cr} for critical accumulation was found to be *independent* of ν_o, $\Delta\rho_{ow}$, Q and water depth h.

Johnston et al.

Johnston *et al.*'s (1993) study was aimed at providing a better hydrodynamic understanding of containment of highly viscous oil slicks. A theoretical model describing the phenomenon was introduced where the importance of oil circulation on the *critical accumulation* failure mechanism was stressed.

Experiments were performed in a flume 24 m by 0.4 m by 0.4 m. Water depths ranged from 0.18 m to 0.3 m and model boom drafts ranged from 0.05 m to 0.08 m. Uniform current characteristics were obtained using a pump and a specially designed inlet manifold. Water level control was achieved using a weir type mechanism and flow rates were adjusted using valves in the inlet line. Oil viscosities of $\nu_o =$ 500 to 10,000 cs with relative densities $s =$ 0.900 to 0.985 were tested. The high sensitivity of oil viscosity to temperature changes was used to alter viscosity in the experiments, with negligible change in oil density. Parameters measured included, slick length, thickness, visual observation of behavior, interface shape (measured using capacitance gages). The air-oil interface was assumed to be constant in time and the rise of the interface as a result of the density differences was assumed to have little effect on the dynamics of the oil–water interface.

The main experimental results obtained were as follows,

- Water-in-oil *emulsions* exhibit non-Newtonian behaviors and some of them belong to a specific type of non–Newtonian fluid, known as *Bingham plastics*. The experimental program was geared towards the study of slicks having Bingham plastic characteristics.

- At relatively low values of U (0.10 to 0.26 m/s, depending on oil viscosity and density), the slick interface became dynamic. A *surge* developed at the frontal region (headwave) and pulsed towards the boom. As the oil slick thickness increased, its length reduced. The phenomenon reversed itself as interfacial waves were reflected from the boom.

- The *intensity of the surge* was dependent on flow velocity, oil viscosity, and oil density. For intermediate viscosities (2,000 to 8,000 cs) interfacial waves (surge) periods were small and the pressure build up at the boom seemed to be relieved by the upstream movement of the leading edge of the slick. For higher viscosities ($\geq$ 8,000 cs) the wave period considerably increaseed and circulation in the oil was often inadequate to account for the pressure buildup, leading to a major leakage followed by the slick reforming and a new circulation setting in.

In the light of these experimental findings, the surging phenomenon is posed as a possible precursor to the failure mode by critical accumulation. This is consistent with Delvigne's (1989) findings. A scoop boom was used to facilitate circulation and found to be of limited use since dynamic effects propagated from the front of the slick. A proposed explanation to the *critical accumulation failure* is : as the circulation in the oil becomes insufficient to relieve the shear stresses along the oil–water interface, a shear instability is caused in the slick interface, leading to containment failure.

Song et al.

Song *et al.* (1993) investigated the experimental behavior of contained oil slicks made with diesel fuel and soy bean oil. An analysis based on the approach by Milgram and Van Houten (1978) was performed to predict the interfacial friction coefficient.

Results are basically consistent with prior observations, linking slick length to slick volume and density, and to U. Only drainage and droplet entrainment failure mechanisms were explored since oil viscosities investigated were quite low (4.02 and 99.7 cs). The influence of the densimetric Froude number on the flow field was found to be significant.

1.2.4 Numerical Models

To our knowledge, only four previous studies qualify as numerical models of oil slick containment. In fact, among those, the older works by Zalosh (1974,1976) and by Milgram and Van Houten (1978), represent detailed and thorough investigations, using approaches that accurately address the physics specific to the oil containment problem. On the other

hand, recent modeling works, originated in the early 1990's, which rely on supposedly more accurate but more general Computational Fluid Dynamics techniques, have only met with limited success, owing to the simplifying assumptions made by the researchers for the representation of the interface or due to the modeling techniques chosen.

We will see, in particular, that recent numerical models proposed by Bai and Kim (1992) and Clavelle and Rowe (1993) concentrated primarily on calculating fluid behavior in the bulk of the oil and water domains while ignoring surface tension and KH interfacial waves along the slick-water interface. Because domain-discretization-type methods were used in these models (i.e., Finite Difference Method and Finite Volume Method), they also lacked resolution in the discretization of the geometry of interfaces which are the regions of the flow where accuracy is most needed in order to understand and predict oil-containment instability.

A review of the numerical techniques used thus far is however of great interest as it helps to guide the formulation of our modeling strategy.

Zalosh

In our opinion, despite being the older, only the work by Zalosh (1974,1976) (which for unknown reason seems to have long been forgotten in most of the existing oil containment literature) put emphasis on the important parameters identified in both the qualitative and experimental studies discussed above, that affect interfacial instabilities occurring during containment of an oil slick by a boom, i.e., fluid density difference, surface tension, unsteadiness of KH instability waves, detailed shape of interfaces.

Zalosh studied the headwave instability of an oil slick due to an underlying current velocity U (i.e., for the case of a pure headwave instability without a boom), by developing a numerical model assuming inviscid fluid. In the model, the oil-water, oil-air and air-water interfaces were represented by vortex sheets (VS) discretized using point vortices and semi-infinite VS's used to represent interfaces far away from the slick leading edge. An evolution equation including gravity and surface tension effects was developed and used to compute the geometry of the oil-water interface as a function of time. An implicit numerical scheme was used to solve the time-evolution equation. Using this approach, model results showed some sawtooth instabilities which required geometric smoothing algorithms during time marching computations.

Using this model, Zalosh predicted the occurrence of KH instability waves in the headwave region, for flow velocity beyond a critical value, and initial stages of roll-up of VS's. Some unacceptable simplifications and a few mistakes in the equations, however, prevented quantitatively realistic results for a sufficiently long time. Since our model uses an approach similar to Zalosh's, detailed discussions of this model's equations and numerical procedures can be found in Chapters 2 and 3.

An oil droplet formation algorithm was then formulated and applied to the numerically modeled headwave region. The computed velocity for the onset of significant droplet entrainment was found in good agreement with laboratory experiments. A theoretical analysis

was thus conducted for the droplet entrainment rates which were found to approximately agree with experiments but did not vary with current velocity.

Milgram and Van Houten

Milgram and Van Houten (1978) studied the mechanics of a restrained layer of floating oil above a water current U by performing a quasi-hydrostatic mathematical analysis in the oil layer, combined with an ideal fluid approximation in the water. Since this analysis is the basis of our computations of initial steady-state shape of oil slicks, basic equations for these computations are detailed in Section 3.2 and only a brief summary of this study is given here.

Milgram and Van Houten treated the oil slick instability problem as a combination of potential flow in the underlying water layer (infinite depth) and hydrostatic force equilibrium in the oil slick. This is supported by experimental evidence discussed above showing that circulation in the oil slick is quite slow and essentially stationary.

Assuming potential flow theory in the water, a Green's function Boundary Integral Equation can be expressed for the potential ϕ and the tangential velocity U_{ws} at points (x_l, y_l) along the slick interface boundary Γ_s can be found by taking the tangential derivative of the potential, as,

$$\frac{\partial \phi}{\partial s}(x_l, y_l) = U_{ws}(x_l, y_l) = \frac{U}{2} cos\theta + \int_{\Gamma_s} U_{ws}(x, y) \frac{\partial G}{\partial n} \, d\Gamma(x, y) \tag{1.2}$$

where $G(\boldsymbol{x}, \boldsymbol{x}_l)$ is the Green's function (see Eq. (3.32)). The dynamic free surface boundary condition (Bernoulli eq.) yields the dynamic pressure p_D along the interface as a function of U_{ws} (see Eq. (3.25)).

Neglecting oil momentum fluxes and dynamic pressures, the pressure in the oil layer can be assumed hydrostatic. The forces on an element of oil slick interface are shown in Fig. 3.2 and the force equilibrium equations relating the mean shear stress τ_s, the dynamic pressure and the hydrostatic forces to interface shape and slick depth can be expressed (see Eqs. (3.26) to (3.28)).

Hence, given an initial slick shape measured in experiments $(\eta(x), q(x))$, U_{ws} is calculated by Eq. (1.2) and yields the dynamic pressure which then lets us determine the value of the friction coefficient C_f using the force equilibrium equations.

Milgram and Van Houten showed various experimental results and corresponding values of C_f and thus discussed the relative importance of interfacial shear stress and dynamic pressure in determining slick thickness distribution. The results show that the rear portion of the slick is governed purely by shear stress as is the forward portion for lower current speed. For higher current speed, both dynamic pressure and shear stress are important in determining the shape of the forward portion. Large friction coefficients are shown to be due to flow over a rough interface resulting from the generation of KH waves on the interface.

Bai and Kim

Bai and Kim (1993) formulated a numerical method to determine the thickness of a contained slick and simulate the long scale gravity, inertial, and viscous effects occurring on the oil–water interface while neglecting the unsteady short–scale motion governed by surface tension, viscous and buoyancy effects (i.e., KH instability waves).

As before, the oil layer is modeled following the quasi-hydrostatic approach proposed by Milgram and Van Houten (1978) and the outer water flow (i.e., flow outside the interfacial Boundary Layer) is modeled using a Green's function approach assuming ideal fluid. The modeling of the inner water layer (i.e., the interfacial Boundary Layer) is performed by solving Navier–Stokes (NS) equations, with kinematic viscosity terms only (i.e., a Stokes flow model; see e.g. Eqs. (1.5)).

The outer layer (far from the interface) is modeled using a streamfunction ψ (also see Section 3.2). Boundary conditions at the oil-water interface are linearized to yield the following simplified problem,

$$\begin{aligned}
\nabla^2\psi &= 0 && \text{for } y < 0 \\
\frac{\partial\psi}{\partial y} &= \frac{g}{U^2}\psi && \text{for } x < 0, y = 0 \text{ on } \Gamma_f \\
\frac{\partial\psi}{\partial y} &= \frac{gs}{U^2}\psi - \frac{g(1-s)}{U}(q-\eta) && \text{for } x \geq 0, y = 0 \text{ on } \Gamma_s
\end{aligned} \qquad (1.3)$$

where Γ_f denotes the air-water interface and Γ_s the oil-water interface.

Closure for the above system of equations is provided by determining $q(x)$ from the hydrostatic force equilibrium along the oil slick interface (see Eqs. (3.26) to (3.28)) and from the viscous model of the interface Boundary Layer. The viscous model within the Boundary Layer is based on a finite difference solution of the NS equations and on the continuity equation for incompressible fluids. The details of the model are not clear from the paper but, apparently, a system of Ordinary Differential Equations is derived, following Kantarovich's variational approach, and is then solved by Newton–Raphson iterations.

In the numerical results, Bai and Kim note that the use of the molecular water viscosity in the NS equations modeling yields computed oil slick thicknesses far smaller than observed in practice, e.g., by Milgram and Van Houten. This is attributed to the assumption made in the model of neglecting (turbulent) Reynolds stresses. A rather heuristic increase in the molecular viscosity coefficient applied in some computations shows that the computed interface shape can be "made" qualitatively similar to results obtained experimentally by Milgram and Van Houten.

Clavelle and Rowe

Following Johnson *et al.* (1993), Clavelle and Rowe (1993) posed that *critical accumulation* failures occur due to the inability of the internal circulation in the oil to account for the interfacial shear stress, at current speeds exceeding 0.15 m/s. To account for internal

circulation within the oil and for the non-uniform flow beneath the slick, an approximate solution to the Navier–Stokes (NS) equations for layered fluids is applied to the problem.

The solution approach involves the use of a finite difference–based numerical model referred to as *SOLA-VOF*. This model uses fractional Volume Of Fluids (VOF) to establish and keep track of the density interface location more accurately than in pure VOF methods. A function $F(x, y, t)$ is defined within each computational cell with values between 0 and 1 for water and oil, respectively, and a temporal dependence specified by the standard kinematic condition,

$$\frac{\partial F}{\partial t} + u\frac{\partial F}{\partial x} + v\frac{\partial F}{\partial y} = 0 \tag{1.4}$$

The flow in both fluids is described by the full two-dimensional NS momentum equations and by the continuity equation,

$$\begin{aligned} \frac{\partial u}{\partial t} + u\frac{\partial u}{\partial x} + v\frac{\partial u}{\partial y} &= g_x - \frac{1}{\rho}\frac{\partial p}{\partial x} + \nu\left(\frac{\partial^2 u}{\partial x^2} + \frac{\partial^2 u}{\partial y^2}\right) \\ \frac{\partial v}{\partial t} + u\frac{\partial v}{\partial x} + v\frac{\partial v}{\partial y} &= g_y - \frac{1}{\rho}\frac{\partial p}{\partial y} + \nu\left(\frac{\partial^2 v}{\partial x^2} + \frac{\partial^2 v}{\partial y^2}\right) \\ \frac{\partial u}{\partial x} + \frac{\partial v}{\partial y} &= 0 \end{aligned} \tag{1.5}$$

where ρ and ν denote the density and the kinematic viscosity of the considered fluid (oil or water), and (g_x, g_y) denotes the gravitational acceleration vector.

Steps in the numerical implementation are essentially : (i) finite difference approximations to the momentum equations (1.5) are used to determine the velocities at the next time step; (ii) pressure is iteratively adjusted in the VOF's cells and the resulting corrections to the velocities are added to those computed in step (i); (iii) the time derivative of function F is used to time step the system to later time; (iv) numerical dissipation is used in the computational model to approximately simulate turbulence.

Due to the computationally expensive nature of such simulations, only coarse grid sizes were used by Clavelle and Rowe. Hence, poor resolution is obtained for the oil-water interface. In the applications presented in the paper, free surface boundary conditions were not implemented. Results show that only qualitative agreement is obtained with interface shapes measured by Delvigne (1989) for the critical accumulation failure mode.

1.3 Statement of the problem

The literature review identified key parameters and physical phenomena responsible for the three failure modes of oil containment by a boom. More specifically, in the light of Delvigne (1989) and Johnston *et al.* (1993) experiments, *critical accumulation* seems to be the dominant failure mode for high viscosity oils that are found in actual slicks.

Critical accumulation results from the interplay of the following physical processes and parameters (see Fig. 1.2),

- the relative *oil-water velocity* U, which controls the magnitude of interfacial friction forces and triggers and sustains KH instability;
- the fluid *density difference*, $\Delta\rho_{ow} = \rho_w - \rho_o$ (or, $1 - s$, with $s = \rho_o/\rho_w$), which affects both slick thickness and spreading forces;
- $\Delta\rho_{ow}$ and the *surface tension* at the oil water interface, σ_{ow}, which both affect the growth of interfacial KH waves;
- the interfacial *friction coefficient*, C_f, which controls the magnitude of interfacial friction forces and thus affects oil slick thickness, and is a function of interfacial shape (including irregularities due to KH waves);
- *oil viscosity*, ν_o, which damps out short interfacial waves and limits the strength of internal circulation cells within the oil slick (hence justifying a quasi-hydrostatic assumption for highly viscous oil slicks).

Other parameters of lesser importance are : σ_{aw} and σ_{oa}, the air-water and oil-air surface tension, respectively.

As far as the KH instability at the interface, increasing U or C_f reinforces the instability whereas increasing σ_{ow} or $\Delta\rho_{ow}$ (i.e., buoyancy) reduces the instability.

Overall, a steady-sate slick shape can be achieved for $U < U_{cr}$, when stabilizing forces (i.e., spreading forces and circulation in the slick) can balance interfacial friction forces. For $U > U_{cr}$, however, increased friction forces at the interface can no longer be compensated by counteracting forces, particularly for high viscosity oils for which circulation in the slick is very limited. Hence, slick length must decrease to balance friction forces and, as a result, interfacial waves grow even larger (see Fig. 1.3), which increases friction forces even more. This leads to the unstable reduction in slick length and total loss of oil by drainage under the boom that characterize *critical accumulation*. Delvigne points out that, at the onset of critical accumulation, strong deformations of interfacial waves, headwave, or both are observed. [This is confirmed by Johnston *et al.*.] He also notes that, for lower viscosity oils, a similar unstable growth of interfacial waves would probably lead to oil being torn off the wave crests and, therefore, to droplet entrainment.

Hence, it appears that modeling KH instability and resulting interfacial waves in the context of oil containment by a boom is the key to both understanding and predicting *critical accumulation*. In proposing this project and anticipating the high degree of complexity of physical mechanisms involved, we initially suggested an "incremental" modeling approach where the initial model would only be a first step towards a more comprehensive model of oil containment that could eventually provide practically useful results. In view of the better overall understanding of critical accumulation that resulted from the extensive literature review conducted as part of this project, we can now more clearly identify a hierarchy of modeling strategies aimed at "incrementally" addressing the problem. This hierarchy will correspond to phases in model development with successive improvements of the level of

	OIL	O - W INTERFACE	WATER
	Modeling techniques used in literature		
	Quasi-hydrostatic Viscous (NS)	**Vortex Sheet (no S.T) Viscous (NS)**	**Inviscid Fluid Viscous (NS)**
	Proposed modeling strategies for the project		
Phase I	**Quasi-hydrostatic**	**Inviscid Vortex Sheet with surface tension**	**Inviscid Fluid**
Phase II	**Quasi-hydrostatic**	**Viscous Vortex Sheet with surface tension**	**Inviscid Fluid**
Phase III	**Viscous (NS)**	**Viscous Vortex Sheet with surface tension**	**Inviscid Fluid**

Figure 1.5: Table of existing and proposed modeling strategies. Phase I model was developed under the FY94 project reported on here and Phase II model is currently being developed as part of the FY95 project. NS : Navier-Stokes equations; S.T : surface tension.

physics modeled and, hence, also of increased modeling accuracy. This will be detailed in the following.

Modeling the problem sketched in Fig. 1.2 involves solving for the unsteady motion of a two fluid system in the presence of fixed obstacles (bottom, boom). This system has both free surfaces (air-oil, air-water) and an interface (oil-water) for which viscous and turbulent effects may be important. Apart from the region very close to the oil-water interface, water behaves as an almost perfect *inviscid fluid*, due to the large Reynolds number of the underlying flow (e.g., Batchelor, 1967). From the literature review, it is apparent that *dynamic effects* dominate along the oil–water interface as far as development of KH instabilities and interfacial waves (e.g., Wilkinson, 1972). Besides dynamic effects, both slick thickness $q(x)$ and shape also depend, but to a lesser extent, on *viscous/turbulent effects* at both the oil-water interface and within the oil slick (slow viscous circulation occurs within the oil slick; Milgram and Van Houten, 1978). *Surface tension* at the interface also plays an important role in the development of KH waves (Di Pietro and Cox, 1980; Rangel and Sirignano, 1988).

Figure 1.5 gives a summary of modeling techniques, discussed in Section 1.2.4, that were proposed in the literature for representing the motion of the oil slick, the oil–water interface, and the underlying water, in the oil containment problem. Among the few existing models, it seems that only the older work by Zalosh (1974) included the important parameters identified above as affecting interfacial instability phenomena responsible for

the *critical accumulation* failure of oil slicks. In particular, this was the only model where unsteadiness of KH shear instability and detailed shapes of interfaces were accounted for. This work was based on using inviscid Vortex Sheets (VS) to represent interfacial geometry and vorticity as a function of time. Several unrealistic simplifications and mistakes in the model equations, however, prevented this model from providing quantitatively realistic results for a sufficiently long time (see further discussion of this in Chapters 2 and 3). Two other models (Bai and Kim, 1992; Clavelle and Rowe, 1993) concentrated on representing fluid behavior in the bulk of the oil and water domains and ignored surface tension and KH waves on the oil–water interface. Because domain-discretization-type methods were used in the latter models (i.e., Finite Difference Method, Finite Volume Method), they also lacked sufficient resolution for the discretization of the interface geometry. These, however, are the regions of the flow where accuracy is most needed in order to correctly model and predict oil containment failure by critical accumulation.

It will be shown in Chapter 2 that, for an inviscid fluid in which (shear-induced) vorticity is concentrated along interfaces and solid boundaries, vorticity is well represented by vortex sheets (VS) . The analysis of the VS dynamics shows that induced velocities can be expressed by Biot-Savart's law (e.g., Lamb, 1932; Batchelor, 1967), which employs a boundary integral formulation. This allows for the development of Boundary Integral Equation (BIE) models which, when combined with higher-order Boundary Element Methods (BEM) for the spatial discretization, have proved to be very efficient and accurate for solving unstable free surface flow and gravity wave problems (e.g., Grilli and Subramanya, 1995, 1996). More specifically, in BIE/BEM models, discretization of the solution is limited to boundaries (i.e., to interfaces in the present case) whereas the representation of the solution inside the fluid domain is exact. Hence, model grids are very much reduced in size compared to domain-discretization-type methods and high resolution can thus be achieved along the boundaries. Furthermore, for moving boundary problems like the present one, time updating of both the discretization and the boundary conditions along boundaries is a much more efficiently and accurately implemented in BEM models than in domain-discretization-type models where the whole spatial grid has to be recreated at each time step.

It was thus decided, in the present study, to adopt the *inviscid VS* approach to represent the shear layer (interface) between oil and water in a first model of oil containment instabilities. This model is hereafter referred to as the *Phase I model* and the present report concentrates on describing the development and the implementation of this model. The Phase I model assumes that viscous circulation is neglected in the oil slick, i.e., a *quasi-hydrostatic* hypothesis. This is acceptable in view of the experimental results discussed in the literature review, particularly for high viscosity oils, which are those found in many slicks. The VS approach exactly accounts for the vorticity generated by the velocity jump at the oil-water interface but not for the viscous or turbulent diffusion of vorticity that may occur at the interface [5]. The Phase I model also assumes that the underlying water behaves

[5]Note that the vorticity along the VS's will induce a slow non-viscous rotational motion in the oil slick, but with likely minimal vertical accelerations; this is consistent with the assumption that pressure in the oil is close to hydrostatic. Accounting for a slow circulation in the slick would only provide small additional

as an incompressible *inviscid fluid* (i.e., ideal fluid). The main features for the Phase I model are summarized in Fig. 1.5.

The Phase I model was developed and validated as part of Task (ii) of this project. As stated in our original objectives, it is anticipated that this model will "provide a firm foundation with which to perform more sophisticated analyses that are more closely representative of at sea- and full-scale laboratory conditions". Such analyses will imply extending the Phase I model to include a more accurate physical representation of interfacial instability and will be the object of continuations of this project (see Chapter 5). In particular, *interfacial friction* was identified as one of the important factors for critical accumulation. In the Phase I model, however, no explicit friction term was included in the dynamics of inviscid VS's. Hence, it is proposed, in an extension to the present study, to model viscous and turbulent effects within a small boundary layer close to the oil-water interface and thus to include friction forces in the analysis. This approach, globally referred to as *viscous VS*, will be implemented as part of the Phase II model, as a continuation of this project. Finally, modeling of the slow *viscous circulation* in the oil slick will be proposed as the last extension to the present model, referred to as the Phase III model. This modeling will be done through solving Stokes flow equations within the oil slick. The main characteristics for the Phase II and III models are summarized in Fig. 1.5.

In the Phase I model, VS's will be discretized by *piecewise-constant elements* of vorticity. This represents an improvement over most existing VS models which use less accurate point vortices to discretize vortex sheets (e.g., Zalosh, 1974, 1976; Zalosh and Jensen, 1975; Rangel and Sirignano, 1988). [In the Phase II model, however, we are planning on using higher-order elements to represent VS's and thus providing better accuracy for the representation of interfacial waves.] *Time evolution* of the vortex sheets at the oil-water interface will be computed using an equation that accounts for both the oil-water density difference and interfacial tension effects (Zaroodny and Greenberg, 1973; Fink and Soh, 1974; Zalosh, 1974, 1976; Zalosh and Jensen, 1975; Rangel and Sirignano, 1988). Details of the Phase I model equations, and numerical algorithms and implementation are given in Chapter 2 and 3, respectively.

stabilizing forces reducing interfacial waves. Hence, the present model is likely to slightly overpredict the growth of interfacial instabilities.

Chapter 2

General equations for the dynamics of vortex sheets

2.1 Velocity-vorticity equations for a vortex sheet

For inviscid, incompressible, uniform fluids in two-dimensional motion in the plane (x, y) (e.g., Fig. 1.2), with vorticity, $\boldsymbol{\omega}(x, y) = \omega(x, y)\boldsymbol{\nabla} z$, the velocity, $\boldsymbol{u} = (u, v)$, can be calculated for points (x, y) according to the Biot-Savart law (Batchelor, 1967, p84) as,

$$\begin{aligned} u(x,y) &= -\frac{1}{2\pi}\int\int \frac{y-y'}{r^2}\,\omega(x',y')\,dx'\,dy' \\ v(x,y) &= \frac{1}{2\pi}\int\int \frac{x-x'}{r^2}\,\omega(x',y')\,dx'\,dy' \end{aligned} \tag{2.1}$$

with

$$r(x,y,x',y') = \{(x-x')^2 + (y-y')^2\}^{1/2} \tag{2.2}$$

When vorticity is concentrated within *vortex sheets* or within *point vortices* aligned as a sheet, equations (2.1) transform into (Batchelor, 1967, p527),

$$\begin{aligned} u(x,y) &= \frac{1}{2\pi}\int \frac{y-y'}{r^2}\,\gamma(s)\,ds \\ v(x,y) &= -\frac{1}{2\pi}\int \frac{x-x'}{r^2}\,\gamma(s)\,ds \end{aligned} \tag{2.3}$$

where, $\gamma(s) = -\omega(x', y')$, is the *clockwise* vortex sheet strength and $s(x', y')$ is the curvilinear abscissa along the sheet.

When points, $\boldsymbol{x} = (x, y)$, do not belong to the sheet, integrals in (2.3) are non-singular. For points (x, y) within the sheet, integrals in (2.3) are singular for vanishing r and must thus be calculated in a Cauchy Principal Value (CPV) sense. In this case, (2.3) also takes the form of a Boundary Integral Equation (BIE) for $\boldsymbol{u}(x, y)$ on the sheet.

In the numerical model that will be developed to track the motion of vortex sheets representing interfaces between fluids (see Chapter 3), various discretized expressions of

(2.3) will be used to calculate the sheet position as a function of time, according to the Lagrangian definition of velocities,

$$\frac{d\boldsymbol{x}}{dt}(t) \;=\; \boldsymbol{u}(x,y) \tag{2.4}$$

where the time derivative follows the motion of the sheet (see below for detail).

2.2 Piecewise constant vorticity and point vortices

A standard simplifying assumption in modeling studies using Biot-Savart law is to assume that the vorticity in vortex sheets is either *piecewise constant* or is concentrated at *point vortices*. Despite their similarity—and sometimes their confusion in the literature—, these two representations differ in the sense that point vortices do not have a self-induced velocity contribution to Eqs. (2.3) whereas piecewise constant distributions of vortices do have self-induced velocity at the center of each interval, due to CPV integral contributions in (2.3) (Fink and Soh, 1974; Van de Vooren, 1980; Rangel and Sirignano, 1988). Finally, point vortices essentially specify an isotropic flow around their center whereas, for vortex sheets (even with piecewise-constant vorticity distribution), the flow is essentially inhomogeneous for the directions tangent and perpendicular to the sheet.

Differences and similarities between these approaches have been somewhat controversial in the literature and will be detailed in the following.

2.2.1 Point vortices

For point vortices, the vortex sheet is replaced by a series of N equal length segments containing a point vortex of strength (i.e., circulation) Γ_i at the mid-point of each segment.

Since there is no self-induced velocity for point vortices (e.g., Batchelor, 1967, p530), equations (2.3) reduce to,

$$\begin{aligned} u(x_i,y_i) \equiv u_i &= \frac{1}{2\pi}\sum_{j\neq i}\frac{y_i-y_j}{r_{ij}^2}\,\Gamma_j \\ v(x_i,y_i) \equiv v_i &= -\frac{1}{2\pi}\sum_{j\neq i}\frac{x_i-x_j}{r_{ij}^2}\,\Gamma_j \end{aligned} \tag{2.5}$$

for $(i,j=1,...,N)$, and,

$$r_{ij} = \{(x_i-x_j)^2+(y_i-y_j)^2\}^{1/2} \tag{2.6}$$

These are essentially the equations used in Zalosh (1974,1976).

2.2.2 Piecewise constant vortices

As pointed out by several authors (Fink and Soh, 1974; Van de Vooren, 1980; Rangel and Sirignano, 1988), point vortices are a poor representation for a continuous vortex sheet—for instance representing the interface between two fluids—and usually quickly lead to inaccurate or even to unstable results, when used to calculate the dynamics of vortex sheets as a function of time. This seems unless point vortices are continuously regridded to equal arc-length distance on the sheet (Fink and Soh, 1974). The reason for this will be clear from the following.

Vortex sheets in fact represent a continuous (line) vorticity variation which can be well represented by a piecewise polynomial distribution of vorticity, similar to Boundary Elements used in continuum mechanics (e.g. Brebbia, 1978). The simplest possible representation is made of N piecewise-constant elements of vorticity density, $\gamma(s_i) = \gamma_i$.

Doing so, (2.3) transforms into,

$$\begin{aligned} u_i &= \frac{1}{2\pi}\sum_{j=1}^{N}\gamma_j \int_{s_j-\Delta s_j/2}^{s_j+\Delta s_j/2} \frac{y_i - y}{r_i^2}\,ds \\ v_i &= -\frac{1}{2\pi}\sum_{j=1}^{N}\gamma_j \int_{s_j-\Delta s_j/2}^{s_j+\Delta s_j/2} \frac{x_i - x}{r_i^2}\,ds \end{aligned} \tag{2.7}$$

for $(i = 1, ..., N)$, and,

$$r_i = \{(x - x_i)^2 + (y - y_i)^2\}^{1/2} \tag{2.8}$$

When assuming that the geometry within each vortex element is smoothly varying and can thus be approximated by values at mid-point s_i of each element, and denoting by, $\Gamma_i = \gamma_i \Delta s_i$, the circulation attributed to each element i (see geometric explanation of this in Section 2.3), (2.7) reduces to (2.5) for $j \neq i$.

For cases with, $j = i$, however, integrals in (2.7) are singular and CPV's must be calculated. This is easily done using either polar coordinates or complex notations and one finds (e.g., Fink and Soh, 1974),

$$\begin{aligned} u_i &= \frac{1}{2\pi}\sum_{j\neq i}\frac{y_i - y_j}{r_{ij}^2}\,\Gamma_j \;-\; \frac{1}{2\pi}\frac{\Gamma_i}{\Delta s_i}\,\sin\theta_i\,\log\frac{r_{i+1/2}}{r_{i-1/2}} \\ v_i &= -\frac{1}{2\pi}\sum_{j\neq i}\frac{x_i - x_j}{r_{ij}^2}\,\Gamma_j \;+\; \frac{1}{2\pi}\frac{\Gamma_i}{\Delta s_i}\,\cos\theta_i\,\log\frac{r_{i+1/2}}{r_{i-1/2}} \end{aligned} \tag{2.9}$$

for $(i = 1, ..., N)$; where θ_i is the angle between the x-axis and segment i, and $[r_{i-1/2}, r_{i+1/2}]$ denote distances from both extremities to the mid-point of segment i. Terms with logarithmic variations in (2.9) represent CPV's contributions to velocity (u_i, v_i). It is easy to see in Eq. (2.9) that these contributions disappear when vortex elements are regridded to equal arclength distance[1] so that, $r_{i-1/2} = r_{i+1/2}$.

[1] This was the method used by Rangel and Sirignano (1988) to avoid calculating CPV integrals.

Thus, when regridding is used or when vortex elements do not change length too much as a function of time (actually over one time step in numerical calculations; see Chapter 3), Eqs. (2.5) and (2.7) are essentially identical and the discrete vortex method provides the same results as the piecewise constant vortex elements. When, either regridding is not used or when the length of vortex elements significantly changes with time, CPV's terms provide significant contributions in (2.9) and the assumption of discrete vortices is unacceptable [2]. This is the likely reason why Zalosh (1974,1976), who used discrete vortices and no regridding was unable to pursue computations for a long time without experiencing numerical instability whereas Rangel and Sirignano (1988), who also used discrete vortices but performed regridding at each time step, were able to calculate the development of Kelvin-Helmholtz instability and rolling-up of vortex sheets at an interface, for a fairly long time (see Fink and Soh, 1974; and Van de Vooren, 1980, for discussions of this and other related problems).

As we will see in Chapter 3, with a piecewise-constant representation of vortex sheets, it is not possible to satisfy all dynamic equilibrium equations of vortex sheets when performing regridding of the discretization to equal arc-length distance. Therefore, in the present model, it will be necessary to accurately calculate CPV integrals representing self-induced velocity contributions.

2.3 Vorticity dynamics equations for a vortex sheet

2.3.1 Circulation on a vortex sheet

Along a material contour $[0, s]$, circulation is defined as (Batchelor, 1967),

$$\Gamma(s) \equiv \int_o^s d\Gamma = \int_o^s \boldsymbol{u} \cdot d\boldsymbol{s}' \tag{2.10}$$

where s denotes the curvilinear abscissa and $d\boldsymbol{s}'$ is the tangential vector element along the contour.

For a vortex sheet representing the interface between two fluids, following Zalosh (1974, 1976), Van de Vooren (1980), and Rangel and Sirignano (1988), the elementary circulation $d\Gamma$ can be calculated by isolating an element of interface of small but finite thickness and considering a contour crossing the interface, as,

$$d\Gamma \equiv \gamma(s)\, ds = \Delta\boldsymbol{u} \cdot d\boldsymbol{s} = \Delta u_s\, ds \tag{2.11}$$

in which $\Delta\boldsymbol{u}$ and Δu_s denote jumps of fluid velocity and tangential fluid velocity across the interface, respectively.

[2] One would see, for instance, that if elements (i.e., boundary segments) are very much stretched or become very small, CPV terms in (2.9) provide almost singular (i.e., very large) contributions, whereas discrete vortices approaching each other would not exhibit this behavior in (2.5).

Equation (2.11) implies that, for a vortex sheet at the *interface between two fluids* moving with velocity $\boldsymbol{u}_o$ and $\boldsymbol{u}_1$, respectively, the vortex sheet strength is given by,

$$\gamma(s) = \Delta u_s = u_{os} - u_{1s} \tag{2.12}$$

in which,

$$u_{os} = \boldsymbol{u}_o \cdot \boldsymbol{s} \quad ; \quad u_{1s} = \boldsymbol{u}_1 \cdot \boldsymbol{s} \quad ; \quad \boldsymbol{s} = [\cos\beta, \sin\beta] \tag{2.13}$$

where $\boldsymbol{s}$ is the tangential vector along the sheet and $\beta(s)$ is the angle between the tangent to the sheet and the x-axis [3].

If we now calculate the circulation associated with a small vortex element i of length Δs_i, over which we can assume constant velocity and smoothly varying geometry, (2.10)-(2.12) transform into,

$$\Gamma(s_i) \equiv \Gamma_i = \int_{s_i - \Delta s_i/2}^{s_i + \Delta s_i/2} (\, u_{os} - u_{1s}\,)\, ds \simeq (\, u_{os} - u_{1s}\,)_i\, \Delta s_i = \gamma_i \Delta s_i \tag{2.14}$$

2.3.2 Rate of change of circulation for a vortex sheet

For a uniform, incompressible, inviscid fluid with conservative forces, Kelvin's theorem states that the rate of change of circulation around a closed material contour moving with the fluid is zero (e.g., Batchelor, 1967),

$$\frac{D\,\Gamma}{D\,t} = 0 \qquad \text{with} \qquad \frac{D}{D\,t} \equiv \frac{\partial}{\partial t} + \boldsymbol{u} \cdot \boldsymbol{\nabla} \tag{2.15}$$

where D/Dt denotes the material derivative.

For a vortex sheet at the interface between two regions of different velocity within the same fluid (e.g., jet, shear current), however, Van de Vooren (1980) clearly showed that a contour crossing the interface and moving with the fluid does not remain closed. Hence, Kelvin's theorem as stated in (2.15) is not applicable. Kelvin's theorem may only be applied for a contour moving with the reference velocity, $\boldsymbol{u} = \frac{1}{2}(\boldsymbol{u}_o + \boldsymbol{u}_1)$, equal to the mean between velocities on both sides of the sheet. This reference velocity will be referred to as the *sheet velocity* and will be used whenever calculating material time derivatives with respect to the sheet motion, referred to as d/dt.

For the interface between two different fluids with density ρ_o and ρ_1, and non-zero interfacial tension σ_{o1}, the fluid is non-uniform and forces are non-conservatives. Hence the rate of change of circulation around a material contour crossing the interface is non-zero and an evolution equation must be developed for it. Zaroodny and Greenberg (1973) first derived an equation for the rate of change of circulation for a continuous vortex sheet without surface tension. Zalosh (1974,1976) developed a similar equation, including surface tension effects, for a sheet discretized with discrete vortices but made an error when he failed to

[3] Note that β and θ, introduced earlier, have different definitions but that, for calculations of self-induced velocity of piecewise constant vortex sheet elements, these angles have the same value.

consider the difference mentioned above between time derivatives, D/Dt, following fluid particles on either side of the sheet and those, d/dt, following the sheet motion. This was pointed out in a discussion by Rottman and Olfe (1977). Rangel and Sirignano (1988) derived the correct evolution equation but without including gravity effects.

The following is a derivation of the rate of change of circulation, including both gravity and surface tension effects at the interface between two fluids, for a vortex sheet with piecewise constant vorticity elements. Taking the material time derivative of the circulation equation (2.10), we get,

$$\frac{D\,\Gamma}{D\,t}(s) = \int_o^s \frac{D\,\boldsymbol{u}}{D\,t}\cdot d\boldsymbol{s}' + \int_o^s \boldsymbol{u}(s')\cdot d(\frac{D\,\boldsymbol{s}'}{D\,t}) \tag{2.16}$$

Because the material derivative follows the fluid particles, we have, by the Lagrangian definition of velocity, $D\boldsymbol{s}'/Dt = \boldsymbol{u}(s')$, and the dot product in the second integral is zero. Hence, using (2.11),(2.12),(2.13),

$$\frac{D\,\Gamma}{D\,t}(s) = \int_o^s (\,\frac{D\,u_{os}}{D\,t} - \frac{D\,u_{1s}}{D\,t}\,)\,ds \tag{2.17}$$

As done in equation (2.14) for the circulation, we can now use (2.17) to calculate the rate of change of circulation associated with a small vortex element i of length Δs_i, over which we can assume constant velocity and smoothly varying geometry,

$$\frac{D\,\Gamma}{D\,t}(s_i) \equiv \frac{D\,\Gamma_i}{D\,t} = \int_{s_i-\Delta s_i/2}^{s_i+\Delta s_i/2} (\,\frac{D\,u_{os}}{D\,t} - \frac{D\,u_{1s}}{D\,t}\,)\,ds \simeq (\,\frac{D\,u_{os}}{D\,t} - \frac{D\,u_{1s}}{D\,t}\,)_i\,\Delta s_i \tag{2.18}$$

Tangential accelerations in (2.18) can be expressed for both fluids using Euler's equations,

$$\frac{D\,\boldsymbol{u}_{o,1}}{D\,t} = -\frac{1}{\rho_{o,1}}\boldsymbol{\nabla} p_{o,1} \;-\; g\boldsymbol{\nabla} y \tag{2.19}$$

in which subscripts denote fluid 0 or 1, p is the fluid pressure (discontinuous across the interface due to surface tension) and g is the acceleration of gravity (vertical pointing in the downward y direction). Taking the dot product of (2.19) with the tangential vector $\boldsymbol{s}$, we get,

$$\frac{D\,u_{os,1s}}{D\,t} = -\frac{1}{\rho_{o,1}}\frac{\partial p_{o,1}}{\partial s} \;-\; g\sin\beta \tag{2.20}$$

Replacing tangential accelerations from (2.20) in (2.18), we get,

$$\frac{D\,\Gamma_i}{D\,t} = (\,\frac{1}{\rho_1}\frac{\partial p_1}{\partial s} - \frac{1}{\rho_o}\frac{\partial p_o}{\partial s}\,)_i\,\Delta s_i \tag{2.21}$$

From the definition of the *sheet velocity*, $\boldsymbol{u}$, the tangential acceleration following the vortex sheet is obtained as,

$$\frac{du_{si}}{dt} = \frac{1}{2}\,(\frac{du_{os}}{dt} + \frac{du_{1s}}{dt})_i \tag{2.22}$$

with, according to the definitions of different material derivatives,

$$\frac{d}{dt} = \frac{D}{D\,t} \pm \frac{1}{2}(\boldsymbol{u}_o - \boldsymbol{u}_1)\cdot\boldsymbol{\nabla} \tag{2.23}$$

with the plus sign being taken in fluid 1 and the minus sign in fluid 0. Using (2.23) in (2.22), we get,

$$\frac{du_{si}}{dt} = \frac{1}{2}(\frac{D\,u_{os}}{D\,t} + \frac{D\,u_{1s}}{D\,t})_i - \frac{1}{4}(u_{os} - u_{1s})_i\,(\frac{\partial u_{os}}{\partial s} - \frac{\partial u_{1s}}{\partial s})_i \tag{2.24}$$

Finally, using Euler equations (2.20) for the tangential velocities and equation (2.12) for the vortex sheet strength, we get,

$$\frac{du_{si}}{dt} = -\frac{1}{2}(\frac{1}{\rho_o}\frac{\partial p_o}{\partial s} + \frac{1}{\rho_1}\frac{\partial p_1}{\partial s} + 2g\,\sin\beta)_i - \frac{1}{4}\gamma_i\frac{\partial \gamma_i}{\partial s} \tag{2.25}$$

Due to a confusion between different material derivatives, the last term in equation (2.25) was missing in Zalosh's (1974,1976) equations.

From the expression of surface tension effects at the interface between two fluids (Batchelor, 1967), the pressure jump across the vortex sheet is given by,

$$p_o \;-\; p_1 \;=\; \sigma_{o1}\,\frac{1}{\mathcal{R}} \tag{2.26}$$

in which $1/\mathcal{R}(s)$ is the sheet curvature. In curvilinear coordinates, it can easily be shown that the curvature is identical to, $\partial\beta/\partial s$. Hence, taking the tangential derivative of (2.26), we get,

$$\frac{\partial p_o}{\partial s} \;-\; \frac{\partial p_1}{\partial s} \;=\; \sigma_{o1}\,\frac{\partial^2\beta}{\partial s^2} \tag{2.27}$$

Eliminating the pressure between equations (2.21),(2.25), and (2.27), we finally get the rate of change of circulation at point s_i of the sheet as,

$$\frac{D\,\Gamma_i}{D\,t} = 2\kappa\,\Delta s_i\left(\frac{du_{si}}{dt} \;+\; g\,\sin\beta_i \;+\; \frac{1}{4}\gamma_i\frac{\partial\gamma_i}{\partial s}\right) - \frac{2\sigma_{o1}}{\rho_o+\rho_1}\,\Delta s_i\,\frac{\partial^2\beta_i}{\partial s^2} \tag{2.28}$$

where $\kappa = (\rho_1 - \rho_o)/(\rho_1 + \rho_o)$, by (2.14), $\gamma_i = \Gamma_i/\Delta s_i$, and by (2.13),

$$\frac{du_{si}}{dt} \;=\; \frac{du_i}{dt}\cos\beta_i + \frac{dv_i}{dt}\sin\beta_i \tag{2.29}$$

2.3.3 Acceleration-rate of change of circulation equations for a vortex sheet

Equation (2.28) contains tangential acceleration terms along the vortex sheet, du_{si}/dt proportional to fluid acceleration on the sheet (2.29). In most earlier numerical models of unsteady motion of vortex sheets, accelerations were calculated by backward finite differentiation (Zalosh, 1974, 1976; Zalosh and Jensen, 1975; Rangel and Sirignano, 1988). As

suggested (without detail) by Rangel and Sirignano (1991), however, accelerations can also be calculated by direct time differentiation of Biot-Savart equations (2.3). When carried out under the integral signs following Leibnitz rule, such a differentiation creates terms proportional to both Γ_i and $D\Gamma_i/Dt$. Hence, rates of change of circulation $D\Gamma_i/Dt$ can be iteratively calculated using (2.28) and this expression of accelerations (see Section 3.1.3). Note that limits of integrations, say $s_a(t)$ and $s_b(t)$, have to be set in (2.3) for the variable $s(t)$ before carrying out time differentiation.

In their time differentiation of (2.3), however, it is not clear whether Rangel and Sirignano (1991) accounted for various CPV integrals. In fact, since they altogether avoided calculating such terms for the velocities in (2.9) by using a regridding method (see discussion in previous Section), we believe that they simply calculated accelerations by time differentiating the equivalent [4] of (2.5),(2.6).

In the following, accelerations are calculated by time differentiation of (2.3), assuming a vortex sheet with a piecewise-constant distribution of N vortex elements along curve, $[s_a(t), s_b(t)] = \sum_{j=1}^{N} \Delta s_j(t)$, and taking into account CPV integrals resulting from self-induced velocities. In the numerical model, accelerations will be explicitly replaced in (2.28), as a function of Γ_i and $D\Gamma_i/Dt$, and rates of change of circulation $D\Gamma_i/Dt$ will be explicitly calculated.

Thus, by (absolute) time differentiation (2.3) following the motion of point, $\boldsymbol{x} = (x, y)$ on the vortex sheet as well as changes along the sheet at points $\boldsymbol{x}' = (x', y')$, and with (2.11), we obtain for, $i = 1, ..., N$,

$$\begin{aligned} \frac{du_i}{dt} &= \frac{1}{2\pi} \sum_{j=1}^{N} \frac{d}{dt} \Big\{ \int_{\Delta s_j} \frac{y_i - y'}{r_i^2} \gamma \, ds' \Big\} \\ \frac{dv_i}{dt} &= -\frac{1}{2\pi} \sum_{j=1}^{N} \frac{d}{dt} \Big\{ \int_{\Delta s_j} \frac{x_i - x'}{r_i^2} \gamma \, ds' \Big\} \end{aligned} \tag{2.30}$$

which, by applying Leibnitz rule and isolating CPV integrals (last terms), reads,

$$\begin{aligned} \frac{du_i}{dt} &= \frac{1}{2\pi} \Big\{ \sum_{j \neq i} \frac{d}{dt} [\frac{y_i - y_j}{r_{ij}^2}] \, \Gamma_j \; + \sum_{j \neq i} \frac{y_i - y_j}{r_{ij}^2} \frac{d\Gamma_j}{dt} \; + \sum_{j \neq i} \gamma_j \\ &\quad [\frac{y_i - y_{j+1/2}}{r_{i,j+1/2}^2} \frac{ds_{j+1/2}}{dt} - \frac{y_i - y_{j-1/2}}{r_{i,j-1/2}^2} \frac{ds_{j-1/2}}{dt}] + \frac{d}{dt} \Big(\int_{\Delta s_i} \frac{y_i - y'}{r_i^2} \gamma \, ds' \Big) \Big\} \\ \frac{dv_i}{dt} &= -\frac{1}{2\pi} \Big\{ \sum_{j \neq i} \frac{d}{dt} \frac{x_i - x_j}{r_{ij}^2} \, \Gamma_j \; + \sum_{j \neq i} \frac{x_i - x_j}{r_{ij}^2} \frac{d\Gamma_j}{dt} \; + \sum_{j \neq i} \gamma_j \\ &\quad [\frac{x_i - x_{j+1/2}}{r_{i,j+1/2}^2} \frac{ds_{j+1/2}}{dt} - \frac{x_i - x_{j-1/2}}{r_{i,j-1/2}^2} \frac{ds_{j-1/2}}{dt}] + \frac{d}{dt} \Big(\int_{\Delta s_i} \frac{x_i - x'}{r_i^2} \gamma \, ds' \Big) \Big\} \end{aligned} \tag{2.31}$$

[4] Note that in Zalosh (1976), Van de Vooren (1980), and Rangel and Sirignano (1988,1991), periodic problems were solved for which (2.5) was replaced by a different expression assuming a spatial periodicity λ, for the interface shape.

where r is given by (2.2), r_i by (2.8), r_{ij} by (2.6), and $(d\gamma_j/dt)\,\Delta s_j = d\Gamma_j/dt$.

Last terms in Eq. (2.31), for both components of the acceleration, represent CPV integrals that can be calculated following the procedure used for the CPV integrals for the velocity components (see Eq. (2.9)). We get,

$$\begin{aligned}
\frac{d\tilde{u}_i}{dt} &= \frac{1}{2\pi}\frac{d}{dt}\Big\{\int_{\Delta s_i}\frac{y_i-y'}{r_i^2}\,\gamma\,ds'\Big\} = \frac{1}{2\pi}\frac{d}{dt}\Big\{\frac{\Gamma_i}{\Delta s_i}\,\sin\theta_i\,\log\frac{r_{i+1/2}}{r_{i-1/2}}\Big\} \\
\frac{d\tilde{v}_i}{dt} &= -\frac{1}{2\pi}\frac{d}{dt}\Big\{\int_{\Delta s_i}\frac{x_i-x'}{r_i^2}\,\gamma\,ds'\Big\} = -\frac{1}{2\pi}\frac{d}{dt}\Big\{\frac{\Gamma_i}{\Delta s_i}\,\cos\theta_i\,\log\frac{r_{i+1/2}}{r_{i-1/2}}\Big\}
\end{aligned} \tag{2.32}$$

where $[r_{i-1/2}, r_{i+1/2}]$ denote distances from both extremities to the mid-point of segment i.

In the first terms of Eq. (2.31) we have, for both components of the acceleration,

$$\begin{aligned}
\frac{dr_{ij}}{dt} &= \frac{(u_i-u_j)\,(x_i-x_j)+(v_i-v_j)\,(y_i-y_j)}{r_{ij}} \\
&= -(u_i-u_j)\,\cos\theta_{ij} \;-\; (v_i-v_j)\,\sin\theta_{ij}
\end{aligned} \tag{2.33}$$

where Eq. (2.4) has been used and θ_{ij} denotes the angle between the vector from point i to j and the x-axis. Hence, using (2.33), we get,

$$\begin{aligned}
\frac{d}{dt}\Big[\frac{x_i-x_j}{r_{ij}^2}\Big] &= -\frac{(u_i-u_j)\,[(x_i-x_j)^2-(y_i-y_j)^2] \;+\; 2(v_i-v_j)\,(x_i-x_j)(y_i-y_j)}{r_{ij}^4} \\
&= -\frac{1}{r_{ij}^2}\,\{\,(u_i-u_j)\,\cos 2\theta_{ij} \;+\; (v_i-v_j)\,\sin 2\theta_{ij}\,\} \\
\frac{d}{dt}\Big[\frac{y_i-y_j}{r_{ij}^2}\Big] &= \frac{(v_i-v_j)\,[(x_i-x_j)^2-(y_i-y_j)^2] \;-\; 2(u_i-u_j)\,(x_i-x_j)(y_i-y_j)}{r_{ij}^4} \\
&= \frac{1}{r_{ij}^2}\,\{\,(v_i-v_j)\,\cos 2\theta_{ij} \;-\; (u_i-u_j)\,\sin 2\theta_{ij}\,\}
\end{aligned} \tag{2.34}$$

Terms involving time derivatives of $(s_{j+1/2},\, s_{j-1/2})$ in Eq. (2.31) represent contributions to the acceleration obtained by applying Leibnitz's rule in Eq. (2.30). For piecewise constant vortex elements, as usual, we can assume that the geometry is approximated by values at the center point of the elements. Hence, third summations in (2.31) can be simplified as,

$$\begin{aligned}
\sum_{j\neq i}\gamma_j\,\Big[\,\frac{y_i-y_{j+1/2}}{r_{i,j+1/2}^2}\,\frac{ds_{j+1/2}}{dt} - \frac{y_i-y_{j-1/2}}{r_{i,j-1/2}^2}\,\frac{ds_{j-1/2}}{dt}\,\Big] &\simeq \sum_{j\neq i}\gamma_j\,\frac{y_i-y_j}{r_{ij}^2}\,\frac{d\Delta s_j}{dt} \\
\sum_{j\neq i}\gamma_j\,\Big[\,\frac{x_i-x_{j+1/2}}{r_{i,j+1/2}^2}\,\frac{ds_{j+1/2}}{dt} - \frac{x_i-x_{j-1/2}}{r_{i,j-1/2}^2}\,\frac{ds_{j-1/2}}{dt}\,\Big] &\simeq \sum_{j\neq i}\gamma_j\,\frac{x_i-x_j}{r_{ij}^2}\,\frac{d\Delta s_j}{dt}
\end{aligned} \tag{2.35}$$

where $\Delta s_j = s_{j+1/2} - s_{j-1/2}$ is the length of segment j. Furthermore, by definition of $s(x,y)$ and using (2.4) for the velocity, we have,

$$\begin{aligned}
\frac{d\Delta s_j}{dt} &= \frac{ds_{j+1/2}}{dt} - \frac{ds_{j-1/2}}{dt} \\
&= \{u_{j+1/2}\frac{\partial x_{j+1/2}}{\partial s} + v_{j+1/2}\frac{\partial y_{j+1/2}}{\partial s}\} - \{u_{j-1/2}\frac{\partial x_{j-1/2}}{\partial s} + v_{j-1/2}\frac{\partial y_{j-1/2}}{\partial s}\} \\
&= (u_{j+1/2} - u_{j-1/2})\cos\theta_j + (v_{j+1/2} - v_{j-1/2})\sin\theta_j \qquad (2.36)
\end{aligned}$$

where the piecewise-constant segment approximation has been used, with θ_j the angle between the x-axis and segment j. Hence Eq. (2.36) represents effects of differential velocity between extremities of segment j.

Combining Eqs. (2.31)-(2.32), we get,

$$\begin{aligned}
\frac{du_i}{dt} &= \frac{1}{2\pi}\Big\{ \sum_{j\neq i} \frac{\Gamma_j}{r_{ij}^2}\{(v_i - v_j)\cos 2\theta_{ij} - (u_i - u_j)\sin 2\theta_{ij}\} \\
&+ \sum_{j\neq i} \frac{y_i - y_j}{r_{ij}^2}\frac{d\Gamma_j}{dt} + \sum_{j\neq i}\frac{y_i - y_j}{r_{ij}^2}\frac{\Gamma_j}{\Delta s_j}\frac{d\Delta s_j}{dt}\Big\} + \frac{d\tilde{u}_i}{dt} \\
\frac{dv_i}{dt} &= \frac{1}{2\pi}\Big\{ \sum_{j\neq i} \frac{\Gamma_j}{r_{ij}^2}\{(u_i - u_j)\cos 2\theta_{ij} + (v_i - v_j)\sin 2\theta_{ij}\} \\
&- \sum_{j\neq i} \frac{x_i - x_j}{r_{ij}^2}\frac{d\Gamma_j}{dt} - \sum_{j\neq i}\frac{x_i - x_j}{r_{ij}^2}\frac{\Gamma_j}{\Delta s_j}\frac{d\Delta s_j}{dt}\Big\} + \frac{d\tilde{v}_i}{dt} \qquad (2.37)
\end{aligned}$$

in which $d\Delta s_j/dt$ is given by Eq. (2.36).

The CPV integrals in Eq. (2.37) can be calculated using Eq. (2.32) and applying Leibnitz's theorem. After some algebra, we get,

$$\begin{aligned}
\frac{d\tilde{u}_i}{dt} &= \frac{1}{2\pi}\frac{d\Gamma_i}{dt}\frac{\sin\theta_i}{\Delta s_i}\log\frac{r_{i+1/2}}{r_{i-1/2}} + \frac{1}{2\pi}\frac{\Gamma_i}{\Delta s_i}\Big\{\frac{1}{\Delta s_i}\log\frac{r_{i+1/2}}{r_{i-1/2}} \\
&\{(v_{i+1/2} - v_{i-1/2})\cos 2\theta_i - (u_{i+1/2} - u_{i-1/2})\sin 2\theta_i\} + \\
&\sin\theta_i\{\cos\theta_i(\frac{u_{i+1/2} - u_i}{r_{i+1/2}} - \frac{u_i - u_{i-1/2}}{r_{i-1/2}}) + \sin\theta_i(\frac{v_{i+1/2} - v_i}{r_{i+1/2}} - \frac{v_i - v_{i-1/2}}{r_{i-1/2}})\}\Big\} \\
\frac{d\tilde{v}_i}{dt} &= -\frac{1}{2\pi}\frac{d\Gamma_i}{dt}\frac{\cos\theta_i}{\Delta s_i}\log\frac{r_{i+1/2}}{r_{i-1/2}} + \frac{1}{2\pi}\frac{\Gamma_i}{\Delta s_i}\Big\{\frac{1}{\Delta s_i}\log\frac{r_{i+1/2}}{r_{i-1/2}} \\
&\{(v_{i+1/2} - v_{i-1/2})\sin 2\theta_i + (u_{i+1/2} - u_{i-1/2})\cos 2\theta_i\} - \\
&\cos\theta_i\{\cos\theta_i(\frac{u_{i+1/2} - u_i}{r_{i+1/2}} - \frac{u_i - u_{i-1/2}}{r_{i-1/2}}) + \sin\theta_i(\frac{v_{i+1/2} - v_i}{r_{i+1/2}} - \frac{v_i - v_{i-1/2}}{r_{i-1/2}})\}\Big\} \qquad (2.38)
\end{aligned}$$

2.3.4 Semi-infinite vortex sheets

As in Zalosh (1974), horizontal semi-infinite vortex sheets will be used in the numerical model in Chapter 3 to represent regions of the water domain with constant uniform horizontal

velocity U. In Fig. 2, this corresponds to free surface and bottom regions both in front of the slick (from $x = -\infty$ to $x = x_\ell$) and behind the boom (from $x = x_r$ to $x = +\infty$).

Assuming no air velocity and no flow in the bottom, these semi-infinite sheets have a tangential velocity jump, $\Delta u_s = \pm U$ (with the negative sign being taken on the free surface and the positive sign on the bottom).

When part of the fluid domain is discretized with point vortices or piecewise-constant vortex elements, such semi-infinite vortex sheets provide contributions to the discretized forms, (2.5) or (2.9), of Biot-Savart integrals (2.3) for the sheet velocity and also to equation (2.37), for the sheet acceleration. These contributions are calculated in the following.

Let us first calculate the contribution to the velocity field, $\boldsymbol{u}_l$, of a horizontal sheet at depth $y = y_\ell$, with velocity jump, $\Delta u_{s\ell}$, from $x = -\infty$ to $x = x_\ell$,

$$\begin{aligned} u_\ell(x,y) &= +\frac{1}{2\pi}\,\Delta u_{s\ell}\int_{-\infty}^{x_\ell}\frac{y-y_\ell}{(x-x')^2+(y-y_\ell)^2}\,dx' \\ v_\ell(x,y) &= -\frac{1}{2\pi}\,\Delta u_{s\ell}\int_{-\infty}^{x_\ell}\frac{x-x'}{(x-x')^2+(y-y_\ell)^2}\,dx' \end{aligned} \tag{2.39}$$

Straightforward integration of these equations yields,

$$\begin{aligned} u_\ell(x,y) &= -\frac{1}{2\pi}\,\Delta u_{s\ell}\,\{\,\arctan\,(\frac{x-x_\ell}{y-y_\ell})\;-\;\frac{\pi}{2}\,\mathrm{sign}(y-y_\ell)\,\} \\ v_\ell(x,y) &= +\frac{1}{4\pi}\,\Delta u_{s\ell}\,\{\log\,[(x-x_\ell)^2+(y-y_\ell)^2] \\ &\quad -\lim_{x'\to-\infty}\log\,[(x-x')^2+(y-y_\ell)^2]\,\} \end{aligned} \tag{2.40}$$

in which the indefinite limit will disappear when combined with other sheets (see below).

Similarly, we compute the contribution to the velocity field, $\boldsymbol{u}_r$, of a horizontal sheet at depth $y = y_r$, with velocity jump, Δu_{sr}, from $x = x_r$ to $x = +\infty$, as,

$$\begin{aligned} u_r(x,y) &= +\frac{1}{2\pi}\,\Delta u_{sr}\,\{\,\arctan\,(\frac{x-x_r}{y-y_r})\;+\;\frac{\pi}{2}\,\mathrm{sign}(y-y_r)\,\} \\ v_r(x,y) &= -\frac{1}{4\pi}\,\Delta u_{sr}\,\{\log\,[(x-x_r)^2+(y-y_r)^2] \\ &\quad -\lim_{x'\to+\infty}\log\,[(x-x')^2+(y-y_r)^2]\,\} \end{aligned} \tag{2.41}$$

Following the same procedure as for the velocity, we can now calculate contributions of semi-infinite vortex sheets to the acceleration field by time derivation of Eq. (2.39) and of a similar equation for the rightward sheets leading to Eq. (2.41). For stationary vortex sheets with constant strength, $\pm U$, simplifications occur and after integrating from $-\infty$ to x_ℓ, for $d\boldsymbol{u}_\ell/dt$, and from x_r to $+\infty$, for $d\boldsymbol{u}_r/dt$, we get,

$$\begin{aligned} \frac{du_\ell}{dt} &= \frac{1}{2\pi}\,\frac{\Delta u_{s\ell}}{r_\ell^2}\,\{\,v\,(x-x_\ell)\;-\;u\,(y-y_\ell)\,\} \\ \frac{dv_\ell}{dt} &= \frac{1}{2\pi}\,\frac{\Delta u_{s\ell}}{r_\ell^2}\,\{\,u\,(x-x_\ell)\;+\;v\,(y-y_\ell)\,\} \end{aligned} \tag{2.42}$$

and,

$$\begin{aligned}
\frac{du_r}{dt} &= -\frac{1}{2\pi}\frac{\Delta u_{sr}}{r_r^2}\left\{\, v\,(x-x_r) \,-\, u\,(y-y_r)\,\right\} \\
\frac{dv_r}{dt} &= -\frac{1}{2\pi}\frac{\Delta u_{sr}}{r_r^2}\left\{\, u\,(x-x_r) \,+\, v\,(y-y_r)\,\right\}
\end{aligned} \tag{2.43}$$

with,

$$\begin{aligned}
r_\ell &= \left\{(x-x_\ell)^2+(y-y_\ell)^2\right\}^{1/2} \\
r_r &= \left\{(x-x_r)^2+(y-y_r)^2\right\}^{1/2}
\end{aligned} \tag{2.44}$$

As mentioned above, in the numerical model in Chapter 3, semi-infinite vortex sheets will be used to model parts of the free surface and parts of the bottom. Assuming that the unperturbed free surface is at, $y = 0$ and the horizontal bottom is at, $y = -h$, we can calculate the total contribution to both the velocity and the acceleration field, of four vortex sheets located at $(x_\ell, 0)$ and $(x_r, 0)$, with strength $-U$, and at $(x_\ell, -h)$ and $(x_r, -h)$, with strength $+U$.

First, for the velocity, using (2.40) and (2.41), we get,

$$\begin{aligned}
u_{\ell r} &= \frac{U}{2\pi}\{2\pi + \arctan\,(\frac{x-x_\ell}{y}) - \arctan\,(\frac{x-x_\ell}{y+h}) - \arctan\,(\frac{x-x_r}{y}) + \arctan\,(\frac{x-x_r}{y+h})\} \\
v_{\ell r} &= \frac{U}{4\pi}\,\log\frac{\left[(x-x_r)^2+y^2\right]\left[(x-x_\ell)^2+(y+h)^2\right]}{\left[(x-x_\ell)^2+y^2\right]\left[(x-x_r)^2+(y+h)^2\right]}
\end{aligned} \tag{2.45}$$

where, as expected, indefinite limits have cancelled each other. Note that, as a verification, if we take, $x_\ell = x_r$, thus assuming a uniform flow represented by two infinite vortex sheets, we can see that (2.45) indeed reduces to, $u_{\ell r} = U$ and $v_{\ell r} = 0$.

Finally, for the acceleration, it can be seen that all contributions from the four sheets cancel each other and we get, $du_{\ell r}/dt = dv_{\ell r}/dt = 0$.

Chapter 3

Equations for numerical model

3.1 General model equations

3.1.1 Principle of computations

Figure 3.1 gives a sketch of a typical computational domain used in the model, with definition of various parameters.

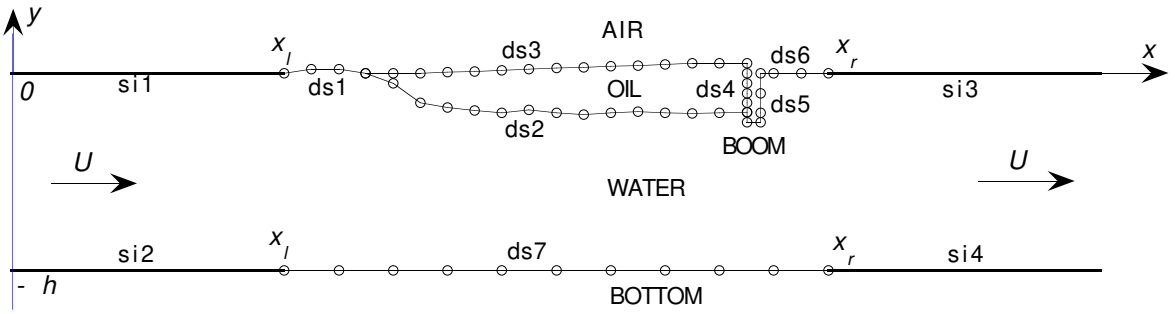

Figure 3.1: Sketch of computational domain with definition of main parameters : U = flow velocity; si1-si4 = semi-infinite vortex sheets; ds1-ds7 = piecewise-constant discretized vortex sheets; ∘ = centers of discretized vortex elements.

In the model, the geometry of boundaries and interfaces is represented using both discretized vortex sheets (ds) with piecewise-constant vorticity distribution and continuous semi-infinite horizontal vortex sheets (si), representing regions of the water domain with constant uniform horizontal velocity U. Vortex sheet dynamics equations for both of these cases have been detailed in Chapter 2.

Contributions of semi-infinite sheets to various integrals presented in Chapter 2 are exactly accounted for in the model, whereas contributions of sheets with piecewise-constant vorticity are discretized using values of both geometry $[(x_i, y_i), \Delta s_i, \theta_i, \beta_i, \partial^2\beta_i/\partial s^2]$ and field variables $[\Gamma_i, d\Gamma_i/dt, (u_i, v_i), (du_i/dt, dv_i/dt)]$ at mid-points $(i = 1, ..., N)$ of each constant vortex sheet element (boundary element).

Assuming that both discretized geometry and field variables are known at time t, the numerical model is used to compute these quantities at time $(t + \Delta t)$ (with Δt being a small time step). This can be done by simultaneously integrating vortex sheet dynamics equations in discretized form, (2.9), (2.14), (2.28), (2.29), and (2.37), together with contributions of semi-infinite vortex sheets of the form (2.40)-(2.45). Computation of an initial steady state solution is discussed in Section 3.2.

In earlier models proposed in the literature for solving vortex sheet dynamics equations, implicit iterative methods were used for the integration of equations of the form (2.4), (2.5) (or equivalent for periodic problems; see Chapter 4) and (2.28) (or equivalent), together with iterative or backward finite difference approximations of accelerations (Zalosh, 1974, 1976; Rangel and Sirignano, 1988, 1991). These models, however, often exhibited sawtooth instability of the solution which required smoothing of the geometry after each time step (e.g., Zalosh, 1974). Such instabilities, we believe, are partly due to the non-representation of self-induced velocities of vortex elements and to the implicit iterative scheme used in the models. In the present study, CPV integrals are exactly accounted for and, hence, self-induced velocity contributions are included in the equations and an explicit time stepping method is developed to hopefully improve both the stability and the accuracy of computations.

The explicit time stepping method is based on truncated Taylor series expansions expressed in Lagrangian form for the position and the vorticity value of individual vortex elements (Grilli and Subramanya, 1995). In the present case, second-order Taylor series are used for time updating of both the sheet geometry and circulation as,

$$\begin{aligned}
x_i(t+\Delta t) &= x_i(t)\ \Delta t\,\frac{dx_i}{dt}(t) + \frac{(\Delta t)^2}{2}\,\frac{d^2x_i}{dt^2}(t) + \mathcal{O}[(\Delta t)^3] \\
y_i(t+\Delta t) &= y_i(t)\ \Delta t\,\frac{dy_i}{dt}(t) + \frac{(\Delta t)^2}{2}\,\frac{d^2y_i}{dt^2}(t) + \mathcal{O}[(\Delta t)^3] \\
\Gamma_i(t+\Delta t) &= \Gamma_i(t)\ \Delta t\,\frac{d\Gamma_i}{dt}(t) + \frac{(\Delta t)^2}{2}\,\frac{d^2\Gamma_i}{dt^2}(t) + \mathcal{O}[(\Delta t)^3]
\end{aligned} \tag{3.1}$$

with, using the Lagrangian definition of velocities (2.4),

$$\begin{aligned}
\frac{dx_i}{dt} &= u_i \quad ; \quad \frac{dy_i}{dt} = v_i \\
\frac{d^2x_i}{dt^2} &= \frac{du_i}{dt} \quad ; \quad \frac{d^2y_i}{dt^2} = \frac{dv_i}{dt}
\end{aligned} \tag{3.2}$$

where velocities (u_i, v_i) are given by (2.9), accelerations $(du_i/dt, dv_i/dt)$ are given by (2.37) (with (2.36) and (2.38)), and rates of change of circulation, $d\Gamma_i/dt$, are given by (2.28),(2.29), with contributions of semi-infinite vortex sheets being added to the equations for the velocity and the acceleration as detailed in Chapter 2.

As pointed out before, equations for $(du_i/dt, dv_i/dt)$ and $d\Gamma_i/dt$ are coupled and therefore first must be solved, simultaneously at time t, before accelerations and rates of change of circulation can be used for time stepping of the vortex sheet geometry and circulation to

time $(t + \Delta t)$ using Eqs. (3.1),(3.2). This is discussed in Section 3.1.3 for the explicit time stepping scheme. Also note that second derivatives of circulation needed in Eq. (3.1) are calculated based on backward finite differences as,

$$\frac{d^2\Gamma_i}{dt^2} \simeq \frac{1}{\Delta t}\{\frac{d\Gamma_i}{dt}(t) - \frac{d\Gamma_i}{dt}(t-\Delta t)\} \tag{3.3}$$

For sake of comparison with earlier models in the literature, an implicit time stepping scheme has also been implemented in the present model, in which equations for the velocities and the rate of change of vorticity are integrated in time using a standard 4th-order Runge-Kutta scheme. This scheme is based on equations listed in Section 3.1.2 in non-dimensional form, Eqs. (3.9) and (3.13),(3.15). Both explicit and implicit schemes have been used in the applications presented in Chapter 4.

Following a similar approach as in Grilli and Subramanya (1995, 1996), the time step Δt used in the model is adaptively calculated at each time step based on a constant mesh Courant number $\mathcal{C}_o$ such that,

$$\Delta t = \mathcal{C}_o \frac{\text{Min}(\Delta s_i)}{\text{Max}(\mid \boldsymbol{u}_i \mid)} \tag{3.4}$$

where the numerator represents the minimum length and the denominator represents the maximum velocity of vortex elements at the current time t. A value $\mathcal{C}_o \simeq 0.5$ was found to ensure good accuracy and stability of computations in most cases.

In the following subsections, model equations are first put in a non-dimensional form better suited to accurate numerical calculations. The computation of acceleration terms is then presented. This is followed by a discussion of the representation of the geometry using "sliding-elements" for calculating vortex sheet geometry and $\partial/\partial s$ derivatives. A description of the node regridding method used in some applications of the model is given. Finally, the computation of initial slick shape is discussed.

3.1.2 Non-dimensional model equations

In computations, a characteristic length scale is defined as λ and a characteristic time scale as $\lambda/\Delta U$, in which ΔU denotes a characteristic velocity jump at the interface. The non-dimensional time is thus, $\tau = t\Delta U/\lambda$.

Based on these, the following non-dimensional variables are introduced for coordinates of vortex element centers and their arc-length,

$$\xi_i = \frac{x_i}{\lambda} \quad ; \quad \eta_i = \frac{y_i}{\lambda} \quad ; \quad \Delta \mathrm{s}_i = \frac{\Delta s_i}{\lambda} \tag{3.5}$$

for the curvature at vortex element centers,

$$\mathrm{c}_i = \lambda \frac{\partial \beta}{\partial s} \tag{3.6}$$

for velocities at vortex elements centers,

$$\mathrm{u}_i = \frac{u_i}{\Delta U} \qquad ; \quad \mathrm{v}_i = \frac{v_i}{\Delta U} \tag{3.7}$$

for the vorticity of vortex elements,

$$\mathrm{g}_i = \frac{\Gamma_i}{\lambda \Delta U} \tag{3.8}$$

Using variables (3.5)-(3.8), the rate of change of vorticity of vortex elements, Eq. (2.28), is transformed into $(i = 1, ..., N)$,

$$\frac{d\,\mathrm{g}_i}{d\,\tau} = 2\kappa\,\Delta \mathrm{s}_i \left(\frac{d\,\mathrm{u}_{is}}{d\,\tau} + \frac{\mathrm{g}_i}{4(\Delta \mathrm{s}_i)^2} \frac{\partial \mathrm{g}_i}{\partial \mathrm{s}} \right) + 2\Delta \mathrm{s}_i \mathbf{Fr}^{-2} \sin\beta_i - 2\Delta \mathrm{s}_i \mathbf{We}^{-1} \frac{\partial \mathrm{c}_i}{\partial \mathrm{s}} \tag{3.9}$$

where **Fr** denotes the Froude number,

$$\mathbf{Fr} = \frac{\Delta U}{\sqrt{g\kappa\lambda}} \tag{3.10}$$

and **We** denotes the Weber number,

$$\mathbf{We} = \frac{\rho_w \lambda\,(1+s)\,(\Delta U)^2}{\sigma_{o1}} \tag{3.11}$$

The non-dimensional tangential acceleration at the interface in (3.9) is found using (2.13) and variables (3.5)-(3.8) as $(i = 1, ..., N)$,

$$\frac{d\,\mathrm{u}_{is}}{d\,\tau} = \frac{d\,\mathrm{u}_i}{d\,\tau}\cos\beta_i + \frac{d\,\mathrm{v}_i}{d\,\tau}\sin\beta_i \tag{3.12}$$

Velocity components are calculated by Biot-Savart law, using Eqs. (2.9) which, with non-dimensional variables, read $(i = 1, ..., N)$,

$$\begin{aligned}
\mathrm{u}_i &= \frac{d\,\xi_i}{d\,\tau} = \frac{1}{2\pi}\sum_{j\neq i} \frac{\eta_i - \eta_j}{\mathrm{r}_{ij}^2}\,\mathrm{g}_j - \frac{1}{2\pi}\frac{\mathrm{g}_i}{\Delta \mathrm{s}_i}\sin\theta_i \log\frac{\mathrm{r}_{i+1/2}}{\mathrm{r}_{i-1/2}} + \mathrm{u}_{\ell r} \\
\mathrm{v}_i &= \frac{d\,\eta_i}{d\,\tau} = -\frac{1}{2\pi}\sum_{j\neq i} \frac{\xi_i - \xi_j}{\mathrm{r}_{ij}^2}\,\mathrm{g}_j + \frac{1}{2\pi}\frac{\mathrm{g}_i}{\Delta \mathrm{s}_i}\cos\theta_i \log\frac{\mathrm{r}_{i+1/2}}{\mathrm{r}_{i-1/2}} + \mathrm{v}_{\ell r}
\end{aligned} \tag{3.13}$$

with by (2.6),

$$\mathrm{r}_{ij} = \{(\xi_i - \xi_j)^2 + (\eta_i - \eta_j)^2\}^{1/2} \tag{3.14}$$

Contributions $(\mathrm{u}_{\ell r}, \mathrm{v}_{\ell r})$ of semi-infinite vortex sheets have been added to velocities in Eq. (3.13). If 4 semi-infinite sheets are used in the model as shown in Fig. 3.1, we obtain, using Eq. (2.45) in non-dimensional form,

$$\begin{aligned}
\mathrm{u}_{\ell r} &= 1 + \frac{1}{2\pi}\{\arctan(\frac{\xi - \xi_\ell}{\eta}) - \arctan(\frac{\xi - \xi_\ell}{\eta + \mathrm{h}}) - \arctan(\frac{\xi - \xi_r}{\eta}) + \arctan(\frac{\xi - \xi_r}{\eta + \mathrm{h}})\} \\
\mathrm{v}_{\ell r} &= \frac{1}{4\pi}\log\frac{[(\xi - \xi_r)^2 + \eta^2]\,[(\xi - \xi_\ell)^2 + (\eta + \mathrm{h})^2]}{[(\xi - \xi_\ell)^2 + \eta^2]\,[(\xi - \xi_r)^2 + (\eta + \mathrm{h})^2]}
\end{aligned} \tag{3.15}$$

where $\mathrm{h} = h/\lambda$.

Accelerations $(d\,\mathrm{u}_i/d\,\tau,\, d\,\mathrm{v}_i/d\,\tau)$ are calculated for the implicit time stepping scheme using simple backward finite differences. For the explicit scheme, accelerations are calculated using Eq. (2.37) put in non-dimensional form,

$$
\begin{aligned}
\frac{d\,\mathrm{u}_i}{d\,\tau} &= \frac{1}{2\pi}\Big\{ \sum_{j\neq i} \frac{\mathrm{g}_j}{\mathrm{r}_{ij}^2} \{\, (\mathrm{v}_i - \mathrm{v}_j)\, \cos 2\theta_{ij} \;-\; (\mathrm{u}_i - \mathrm{u}_j)\, \sin 2\theta_{ij} \,\} \;+\; \sum_{j\neq i} \frac{\eta_i - \eta_j}{\mathrm{r}_{ij}^2}\, \frac{d\,\mathrm{g}_j}{d\,\tau} \\
&+ \sum_{j\neq i} \frac{\eta_i - \eta_j}{\mathrm{r}_{ij}^2}\, \frac{\mathrm{g}_j}{\Delta \mathrm{s}_j} \{\, (\mathrm{u}_{j+1/2} - \mathrm{u}_{j-1/2})\, \cos\theta_j \;+\; (\mathrm{v}_{j+1/2} - \mathrm{v}_{j-1/2})\, \sin\theta_j \,\} \\
&+ \frac{d\,\mathrm{g}_i}{d\,\tau}\, \frac{\sin\theta_i}{\Delta \mathrm{s}_i}\, \log \frac{\mathrm{r}_{i+1/2}}{\mathrm{r}_{i-1/2}} \;+\; \frac{\mathrm{g}_i}{\Delta \mathrm{s}_i} \Big\{ \frac{1}{\Delta \mathrm{s}_i}\, \log \frac{\mathrm{r}_{i+1/2}}{\mathrm{r}_{i-1/2}} \\
&\quad \{\, (\mathrm{v}_{i+1/2} - \mathrm{v}_{i-1/2}) \cos 2\theta_i \;-\; (\mathrm{u}_{i+1/2} - \mathrm{u}_{i-1/2}) \sin 2\theta_i \,\} \;+\; \sin\theta_i \\
&\quad \{ \cos\theta_i \,(\frac{\mathrm{u}_{i+1/2} - \mathrm{u}_i}{\mathrm{r}_{i+1/2}} - \frac{\mathrm{u}_i - \mathrm{u}_{i-1/2}}{\mathrm{r}_{i-1/2}}) + \sin\theta_i \,(\frac{\mathrm{v}_{i+1/2} - \mathrm{v}_i}{\mathrm{r}_{i+1/2}} - \frac{\mathrm{v}_i - \mathrm{v}_{i-1/2}}{\mathrm{r}_{i-1/2}}) \,\} \Big\} \Big\} \\
\frac{d\,\mathrm{v}_i}{d\,\tau} &= \frac{1}{2\pi}\Big\{ \sum_{j\neq i} \frac{\mathrm{g}_j}{\mathrm{r}_{ij}^2} \{\, (\mathrm{u}_i - \mathrm{u}_j)\, \cos 2\theta_{ij} \;+\; (\mathrm{v}_i - \mathrm{v}_j)\, \sin 2\theta_{ij} \} \;-\; \sum_{j\neq i} \frac{\xi_i - \xi_j}{\mathrm{r}_{ij}^2}\, \frac{d\,\mathrm{g}_j}{d\,\tau} \\
&- \sum_{j\neq i} \frac{\xi_i - \xi_j}{\mathrm{r}_{ij}^2}\, \frac{\mathrm{g}_j}{\Delta \mathrm{s}_j} \{\, (\mathrm{u}_{j+1/2} - \mathrm{u}_{j-1/2})\, \cos\theta_j \;+\; (\mathrm{v}_{j+1/2} - \mathrm{v}_{j-1/2})\, \sin\theta_j \,\} \\
&- \frac{d\,\mathrm{g}_i}{d\,\tau}\, \frac{\cos\theta_i}{\Delta \mathrm{s}_i}\, \log \frac{\mathrm{r}_{i+1/2}}{\mathrm{r}_{i-1/2}} \;+\; \frac{\mathrm{g}_i}{\Delta \mathrm{s}_i} \Big\{ \frac{1}{\Delta \mathrm{s}_i}\, \log \frac{\mathrm{r}_{i+1/2}}{\mathrm{r}_{i-1/2}} \\
&\quad \{\, (\mathrm{v}_{i+1/2} - \mathrm{v}_{i-1/2}) \sin 2\theta_i \;+\; (\mathrm{u}_{i+1/2} - \mathrm{u}_{i-1/2}) \cos 2\theta_i \,\} \;-\; \cos\theta_i \\
&\quad \{ \cos\theta_i \,(\frac{\mathrm{u}_{i+1/2} - \mathrm{u}_i}{\mathrm{r}_{i+1/2}} - \frac{\mathrm{u}_i - \mathrm{u}_{i-1/2}}{\mathrm{r}_{i-1/2}}) + \sin\theta_i \,(\frac{\mathrm{v}_{i+1/2} - \mathrm{v}_i}{\mathrm{r}_{i+1/2}} - \frac{\mathrm{v}_i - \mathrm{v}_{i-1/2}}{\mathrm{r}_{i-1/2}}) \,\} \Big\} \Big\}
\end{aligned}
\tag{3.16}
$$

3.1.3 Computation of acceleration terms in explicit scheme

At a given time τ, both the geometry of vortex sheets $(\xi_i, \eta_i, \Delta \mathrm{s}_i, \theta_i)$ and the vorticity g_i are fixed and Eq. (3.13) can thus be used to calculate velocities along the sheets, $(\mathrm{u}_i, \mathrm{v}_i)$.

Hence, Eqs. (3.9) and (3.16) reduce to,

$$
\begin{aligned}
\frac{d\,\mathrm{g}_i}{d\,\tau} &= \mathcal{F}(\frac{d\,\mathrm{u}_i}{d\,\tau}, \frac{d\,\mathrm{v}_i}{d\,\tau}) \\
\frac{d\,\mathrm{u}_i}{d\,\tau} &= \mathcal{G}_1(\frac{d\,\mathrm{g}_i}{d\,\tau}) \\
\frac{d\,\mathrm{v}_i}{d\,\tau} &= \mathcal{G}_2(\frac{d\,\mathrm{g}_i}{d\,\tau})
\end{aligned}
\tag{3.17}
$$

which represents a coupled system of linear algebraic equations for, $d\,\mathrm{g}_i/d\,\tau$, and for $(d\,\mathrm{u}_i/d\,\tau,\, d\,\mathrm{v}_i/d\,\tau)$, at $i = 1, ..., N$, vortex sheet element centers. In the model, this system is solved by iterations at each time step, before the explicit time stepping (3.1)-(3.3) is

used to update the sheets geometry and vorticity to (dimensionless) time, $\tau + \Delta\tau$ (i.e., time $t + \Delta t$).

3.1.4 Computation of geometry and tangential derivatives

In earlier studies (e.g., Zalosh, 1974), simple lower-order finite difference approximations were used to calculate tangential derivatives along interfaces [1]. For the problems solved in the present study, however, due to the intense roll-up of vortex sheets that occurs when instabilities develop along the oil-water interface, even if a low-order (piecewise-constant) representation is satisfactory for the vorticity, it is necessary to use a higher-order representation of the geometry along interfaces. Roll-up indeed leads to a large curvature of the interface and to enhanced surface tension effects (proportional to second-order tangential derivatives of the slope angle; see Eq. (2.28)) which must be accurately accounted for. Hence, the interfacial slope and the curvature must be continuous between vortex elements which requires using a piecewise representation of the geometry of third-order or better.

A higher-order representation of the geometry can be achieved along a segment of an interface either by defining a sliding polynomial interpolation of the geometry on center nodes of vortex elements $(\xi_i, \eta_i; i = 1, ..., N)$ or by using a cubic spline fit on these nodes. In the model, sliding polynomials are 5-node quartic isoparametric boundary elements in which geometric characteristics are calculated for the middle node of the polynomial. Slope angles β_i and tangential derivatives ∂/∂s are calculated along the vortex sheets by direct differentiation within the polynomials. To calculate characteristics for the next node along the interface, the sliding polynomial element is moved forward by one node. The polynomial is kept identical for the first 3 nodes and for the last 3 nodes on a sheet. With cubic splines, 2-nodes cubic polynomials are defined in such a way as to maintain continuity of the slope from one polynomial to the other. This method, however, requires knowledge of end slopes on the interface to be used as boundary conditions in the spline analysis. Moreover, due to the multiple-valued interface geometry that occurs during roll-up, it is necessary to simultaneously use two parametric spline approximations of the geometry.

Details about both methods can be found in Grilli and Subramanya (1996). In the applications, the sliding and the spline methods are used either individually or in combination. In the latter case, a *hybrid method* is defined which combines the advantages of both methods to achieve optimal accuracy : (i) the *sliding* method is first used to calculate the slope at both extremities of the computational domain representing an interface; and (ii) the *spline* method is then applied to the whole interface, using the slopes computed in (i) as boundary conditions at both extremities.

More specifically, using either one of the interpolation methods, the angle β along the interface can be expressed as a piecewise analytical expression. Following a classical Boundary Element methodology (e.g., Brebbia, 1978), we define the intrinsic coordinate $\mu \in [-1, +1]$ in a piecewise sliding or in a cubic polynomial interpolation. Under this

[1] This is likely another reason why Zalosh could not follow the time development of interfacial instabilities for very long.

representation, $x(\mu), y(\mu)$ and $s(\mu)$ are expressed in closed form within each piecewise polynomial approximation of the geometry of an interface and we get, for the geometric parameters in the model,

$$\cos\beta = \frac{x_\mu}{s_\mu} \quad , \quad \sin\beta = \frac{y_\mu}{s_\mu} \quad , \quad s_\mu = \{x_\mu^2 + y_\mu^2\}^{1/2} \tag{3.18}$$

and, for the curvature and its gradient along s,

$$\begin{aligned} \frac{\partial\beta}{\partial s} &= \frac{x_\mu y_{\mu\mu} - x_{\mu\mu} y_\mu}{s_\mu^3} \\ \frac{\partial^2\beta}{\partial s^2} &= \frac{1}{s_\mu^5}\left\{ s_\mu \left(y_{\mu\mu\mu} x_\mu - x_{\mu\mu\mu} y_\mu\right) - \frac{3}{s_\mu}\left[\, x_{\mu\mu} y_{\mu\mu}\left(x_\mu^2 - y_\mu^2\right) - x_\mu y_\mu \left(x_{\mu\mu}^2 - y_{\mu\mu}^2\right)\,\right]\right\} \end{aligned} \tag{3.19}$$

respectively, in which indices denote total derivatives with respect to the intrinsic coordinate. Note that, in the second equation (3.19), third derivatives of the geometry are needed to calculate curvature gradients along interfaces. This justifies using at least cubic polynomials for the representation of the geometry [2].

3.1.5 Node regridding

Regridding of point vortices was used in earlier works (e.g., by Rangel and Sirignano, 1988, in their study of Kelvin-Helmholtz (KH) instability), to prevent vortices from excessively concentrating in roll-up regions of the interface. Due to the increased length of the interface with time, nodes were added prior to regridding to the initial number of nodes used on the interface and were then regridded to equal arc-length distance. A consequence of regridding was also that the need for evaluating CPV integrals was eliminated (see discussion in Chapter 2).

Grilli and Subramanya (1996) developed a node regridding technique to study breaking surface waves based on a combination of sliding and cubic polynomial interpolations similar to those discussed in the previous Section. This technique was modified to apply to a piecewise constant distribution of vortices. More specifically, a node arc length vector, s_l (with $l = 1, ..., N$) is first calculated for the old locations of nodes/centers-of-vortex-elements on the interface, $\boldsymbol{x}_l$, by computing, $\int_0^{s(\mathbf{x}_l)} ds$, over the entire interface as a summation over vortex elements whose geometry is given by the cubic sliding/spline interpolation method. A boundary section is then defined over which regridding is to be performed and the (arbitrary) number of nodes to be added to or removed from this section is used for computing the new arc length increment within the section. Based on this increment, a new arc length vector, s_l^r, is calculated for regridded nodes and mapped node

[2] In fact, in the applications, to improve the accuracy of computed curvature gradients when cubic splines are used, the third derivatives in (3.19) are calculated within a (second) spline approximation directly built on the first-derivatives.

by node onto s_l, to isolate vortex elements k (old nodes $(k, k+1)$) within which new nodes are located. For each such element, an iterative procedure is used to calculate the intrinsic coordinate μ corresponding to a given component of s_l^r and, based on this, nodal coordinates $\boldsymbol{x}_l = \boldsymbol{x}^k(\mu)$ are re-calculated for the new node locations and, similarly, for the vorticity.

This regridding technique was tested in the present model for the KH instability problem. It was thought that the addition of point vortices to selected regions of the interface with high curvature (i.e., roll-up regions) would make results more accurate. Moreover, regridding had proved efficient in the computations by Rangel and Sirignano (1988) who used point vortices. Initial computational results, however, despite a very accurate evaluation of vorticity at regridded nodes, always showed the occurrence of small irregularities in point vortex motions right after regridding, which quickly grew with time. Such a phenomenon was found to occur no matter how many nodes were added and no matter whether regridding was used on the whole interface or only on part of it.

After a more detailed analysis of the vortex sheet dynamics parameters before and after regridding, it was found that regridding violated kinematic conditions of the discretized vortex sheet system. It can be shown, indeed, that the dynamic equilibrium of a vortex sheet system $[s_o, s_N]$ is governed by values of the following three parameters (Batchelor, 1967),

$$\begin{aligned} \bar{x}_N &= \frac{1}{\Gamma_{TN}} \int_{s_o}^{s_N} x\, \gamma(s) ds \\ \bar{y}_N &= \frac{1}{\Gamma_{TN}} \int_{s_o}^{s_N} y\, \gamma(s) ds \\ \bar{r}_N &= \frac{1}{\Gamma_{TN}} \int_{s_o}^{s_N} \sqrt{x^2 + y^2}\, \gamma(s) ds \end{aligned} \tag{3.20}$$

where,

$$\Gamma_{TN} = \int_{s_o}^{s_N} \gamma(s) ds \tag{3.21}$$

is the total vorticity on the vortex sheet.

For point vortex systems, these parameters take the forms,

$$\begin{aligned} \bar{x}_N &= \frac{1}{\Gamma_{TN}} \sum_{i=1}^{N} x_i\, \Gamma_i \\ \bar{y}_N &= \frac{1}{\Gamma_{TN}} \sum_{i=1}^{N} y_i\, \Gamma_i \\ \bar{r}_N &= \frac{1}{\Gamma_{TN}} \sum_{i=1}^{N} \sqrt{x_i^2 + y_i^2}\, \Gamma_i \end{aligned} \tag{3.22}$$

where,

$$\Gamma_{TN} = \sum_{i=1}^{N} \Gamma_i \tag{3.23}$$

For a system made of piecewise-constant vortex elements, however, they take the form,

$$\begin{aligned}
\bar{x}_N &= \frac{1}{\Gamma_{TN}} \sum_{j=1}^{N} x_i \, \gamma_i \Delta s_i \\
\bar{y}_N &= \frac{1}{\Gamma_{TN}} \sum_{j=1}^{N} y_i \, \gamma_i \Delta s_i \\
\bar{r}_N &= \frac{1}{\Gamma_{TN}} \sum_{j=1}^{N} \sqrt{x_i^2 + z_i^2} \, \gamma_i \, \Delta s_i
\end{aligned} \tag{3.24}$$

where Γ_{TN} is again given by (3.23) and $\Delta s_i = \Delta s_{i-1/2} + \Delta s_{i+1/2}$.

Assuming that partial regridding is performed for an arbitrary section of an interface made of N piecewise-constant vortex elements, based on the sole condition of conservation of total circulation on the interface (i.e., Γ_{TN} constant), it can be seen that changes in both Δs_i's and γ_i's of vortex elements will cause variations in $\bar{x}_N$, $\bar{y}_N$, and $\bar{r}_N$, according to Eqs. (3.23),(3.24). On the other hand, when only point vortices are used, the element length does not affect the value of the vortex sheet system dynamic parameters in Eqs. (3.22),(3.23) which can thus be maintained constant. This explains why regridding worked for Rangel and Sirignano's results.

To date, we have not been able to reconcile values of dynamic parameters with regridding for piecewise-constant vortex elements. In Phase II of this study, however, we will introduce higher-order (e.g., cubic) vortex elements with which, we believe, we might be able to use regridding techniques while preserving values of the dynamic parameters of the system.

3.2 Computation of initial steady state slick shape

3.2.1 Principle of initialization

In earlier studies of headwave instability, the initial shape of the oil slick was selected rather arbitrarily. Zalosh (1974) for instance used part of a sine function to define the initial slick shape in his computations (see Section 4.3 for details about this initialization). Based on our analysis of the oil containment problem, we believe that such an arbitrary choice of initial slick shape (and dynamics) in the numerical model may actually induce non-physical (numerical) instabilities of the slick.

An arbitrary geometry selected to represent the interface between oil and water indeed is not likely to satisfy both the kinematic and dynamic boundary conditions along the interface. A violation of these equilibrium conditions is similar to creating an initial perturbation on the interface which, when introduced in a time dependent dynamic model, readily tries to adjust its shape to satisfy the equilibrium conditions. It is likely that such adjustments do not match actual instabilities occurring along an initially stable interface, for which the underlying current velocity is increased beyond the instability threshold.

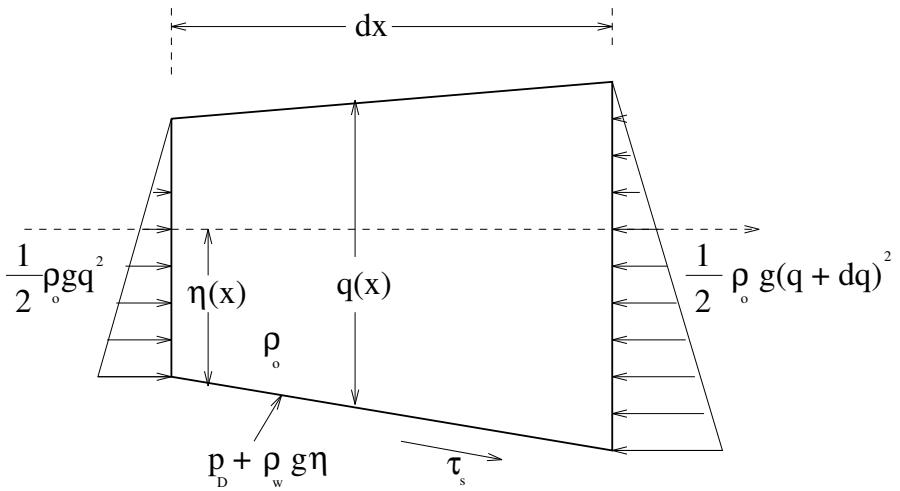

Figure 3.2: Sketch of forces acting on a differential element of length dx of the oil slick as in Milgram and Van Houten's (1978) quasi-hydrostatic model.

In the present Phase I study, only simple cases will be solved in Chapter 4 in order to validate the model equations and numerical procedures (i.e., Kelvin-Helmholtz and headwave instabilities). Hence, the initial shape of interfaces used in the applications will be selected as done in earlier studies.

In the more sophisticated applications of the model to oil containment by a boom that will take place under the ongoing Phase II of this study, however, it will be necessary to calculate an initially stable shape of the oil slick interface, corresponding to an underlying current velocity U below the instability threshold, before interfacial instability is studied. After this initialization stage, current velocity will be increased beyond the instability threshold and development of interfacial waves will be calculated as a function of time using the numerical model developed in this study.

Initialization thus consists in finding the shape of the slick interface $\eta(x)$ (measured from still water level; Fig. 3.2) that satisfies both the dynamic and kinematic conditions on the interface. Following Milgram and Van Houten (1978) quasi-hydrostatic approach within the slick, we express the Bernoulli equation between the front of the slick and any point on the slick interface and get,

$$p_D \;=\; \frac{1}{2}\rho_w \left(U^2 - U_{ws}^2\right) \tag{3.25}$$

Expressing the horizontal equilibrium along the interface (Fig. 3.2), we get to the first-order,

$$\left(p_D + \rho_w g\, \eta\right) \frac{\partial \eta}{\partial x} \;+\; \tau_s \;=\; \rho_o g\, q\, \frac{\partial q}{\partial x} \tag{3.26}$$

Expressing the vertical equilibrium along the interface (Fig. 3.2), we get to the first-order,

$$p_D \;+\; \rho_w g\, \eta \;=\; \rho_o g\, q \tag{3.27}$$

where p_D is the dynamic pressure in the water below the slick, U_{ws} is the tangential flow velocity along the slick, τ_s is the shear stress along the slick, q is the the total slick thickness (i.e., η plus the part above still water level; see Fig. 3.2). The shear stress along the slick can be classically expressed using a simple drag formula (e.g., Batchelor, 1967),

$$\tau_s \;=\; \frac{1}{2}\rho_w \, C_f \, U_{ws}^2 \tag{3.28}$$

where C_f is a non-dimensional friction coefficient function of flow characteristics and roughness along the interface.

In Milgram and Van Houten's study, the interface shape $\eta(x)$ and slick thickness $q(x)$ were experimentally measured and the tangential velocity of the underlying flow was calculated using ideal flow theory, assuming a uniform velocity U for the incident flow ahead of the slick. The friction coefficient (the only "unknown" left in the equations) was then calculated along the interface using Eqs. (3.25)-(3.28). When carrying out Phase II calculations with the present model, we will use the same approach but in reverse mode : the friction coefficient C_f will be calculated along the interface using boundary layer theory and the quasi-steady slick shape will be predicted. Since C_f is a function of *a priori* unknown flow characteristics (e.g., Reynolds number), an iterative method will be used : (i) a slick shape will be assumed; (ii) the tangential velocity along the interface will be calculated for the external water flow, based on ideal flow theory; (iii) the friction coefficient will be calculated for the external flow calculated in (ii); and (iv) a corrected slick shape will be calculated.

More details are provided in the following Sections for stages (ii) to (iv) of the iterative method. Results from this iterative method will be presented as part of Phase II of this study.

3.2.2 External flow calculation

Using a streamfunction representation in the water (e.g., Batchelor, 1967), continuity equation reads,

$$\nabla^2 \psi = 0 \tag{3.29}$$

where ψ is the streamfunction defined such that,

$$u_w = -\frac{\partial \psi}{\partial y} \qquad ; \; v_w = \frac{\partial \psi}{\partial x} \qquad ; \; U_{ws} = -\frac{\partial \psi}{\partial n} \tag{3.30}$$

where (u_w, v_w) are velocity components in the water and $\boldsymbol{n}$ denotes the normal direction along the slick interface pointing outwards from the water. Eq. (3.29) is solved using a Boundary Integral Equation representation (BIE),

$$\alpha(\boldsymbol{x}_l)\psi(\boldsymbol{x}_l) = \int_{\Gamma(\boldsymbol{x})} [\frac{\partial \psi}{\partial n} G(\boldsymbol{x}, \boldsymbol{x}_l) - \psi \frac{\partial G(\boldsymbol{x}, \boldsymbol{x}_l)}{\partial n}] \, d\Gamma(\boldsymbol{x}) \tag{3.31}$$

with,

$$G(\boldsymbol{x}, \boldsymbol{x}_l) = -(1/2\pi)\log \mid \boldsymbol{x} - \boldsymbol{x}_l \mid \tag{3.32}$$

the free space Green's function, $\boldsymbol{x} = (x, y)$ and $\boldsymbol{x}_l = (x_l, y_l)$ representing position vectors for points on boundary Γ, and $\alpha(\boldsymbol{x}_l)$ a geometric coefficient.

The BIE (3.31) is solved using a higher-order Boundary Element Method (BEM) (Grilli and Subramanya 1995, 1996), together with boundary conditions expressing no-flow on the bottom boundary Γ_b and on the boom, and uniform incoming and outgoing flows on lateral boundaries Γ_l (see, e.g., Fig. 3.1). Along the slick interface Γ_s, we also assume a no-flow conditions for the quasi-steady case. In a streamfunction representation, no-flow conditions correspond to specifying streamlines with ψ =cst (e.g., 0 on Γ_s and $h\,U$ on Γ_b) and uniform flow conditions correspond to specifying a linearly varying streamfunction in the vertical direction, i.e., $\psi = \mid y \mid U$.

The solution of (3.31) directly provides, $\partial\psi/\partial n = -U_{ws}$, along the slick interface, to be used in Eq. (3.25). Hence, the ideal flow solution allows one to calculate the dynamic pressure along the slick for any assumed slick shape.

3.2.3 Iterative calculation of slick shape

Non-dimensional variables are introduced in Eqs. (3.25)-(3.28), based on a length scale U^2/g, a velocity scale U, and a stress scale $\rho_w U^2$ (note that for the oil-water interface, $U = \Delta U$). We thus get,

$$x' = \frac{gx}{U^2} \quad ; \quad q' = \frac{gq}{U^2} \quad ; \quad \eta' = \frac{g\eta}{U^2} \tag{3.33}$$

$$p'_D = \frac{p_D}{\rho_w U^2} \quad ; \quad \tau'_s = \frac{\tau_s}{\frac{1}{2}\rho_w U^2} \quad ; \quad C'_f = C_f \frac{U_{ws}^2}{U^2} \tag{3.34}$$

where primes denote non-dimensional variables.

Using definitions (3.33),(3.34), Eqs. (3.25)-(3.28) transform into,

$$p'_D \;=\; \frac{1}{2}\,(1 - U'^2_{ws}) \tag{3.35}$$

where $U'_{ws} = U_{ws}/U$.

$$(p'_D + \eta')\,\eta_{x'} \;+\; \frac{1}{2}\tau'_s \;=\; s\,q'\,q'_{x'} \tag{3.36}$$

where x' indices denote derivatives with respect to x', and $s = \rho_o/\rho_w$.

$$p'_D \;+\; \eta' \;=\; s\,q' \tag{3.37}$$

$$\tau'_s \;=\; C'_f \tag{3.38}$$

Combining Eqs. (3.36) and (3.38), we further get,

$$(p'_D \;+\; \eta')\left((1-s)\,\eta'_{x'} \;-\; p'_{Dx'}\right) = \frac{s}{2}\,C'_f \tag{3.39}$$

After some algebraic transformations, Eq. (3.39) reads,

$$\begin{aligned} \eta'^2 + \frac{2}{1-s}\, p'_D \eta' + \frac{1}{1-s}\, p'_D &= \frac{s}{1-s} \int_0^{x'} \{\, C'_f(\xi) + 2\, p'_D(\xi) \tan\beta(\xi) \,\}\, d\xi \\ &= \frac{s}{1-s}\, F(x') \end{aligned} \tag{3.40}$$

where, $\eta'_{x'} = \tan\beta$, has been used along the interface. The integrand in the right hand side of Eq. (3.40) represents both shear friction effects and, for small β, the horizontal force due to the dynamic pressure along the slick [3].

Eq. (3.40) is a quadratic equation for η' which can be solved as,

$$\begin{aligned} \eta'(x') &= \frac{1}{1-s}\, p'_D(x') \left\{ \sqrt{s}\, \{1 + (1-s)\, \frac{F(x')}{p'^2_D(x')}\, \}^{1/2} - 1 \right\} \\ &= \mathcal{F}(s, F(x'), p'_D(x')) \end{aligned} \tag{3.42}$$

with, from the external flow calculations, using Eq. (3.30) and (3.35),

$$p'_D(x') = \frac{1}{2}\, (1 - \psi'^2_{n'}(x')) \tag{3.43}$$

where $\psi'_{n'}$ is directly provided along the slick interface by the BEM solution for the underlying flow.

The iterative method for calculating the initial slick shape is obtained based on Eqs. (3.42),(3.43), as,

$$\begin{aligned} \eta'_{k+1}(x') &= \mathcal{F}(s, F_k(x'), \psi'_k(x')) \qquad \text{for } k = 1, ... \\ F_k(x') &= \int_0^{x'} \{\, C'_{fk}(\xi) + (1 - \psi'^2_{kn'}(\xi)) \tan\beta_k(\xi) \,\}\, d\xi \end{aligned} \tag{3.44}$$

where k denotes the iteration number. A rough initial shape, say $\eta'_o(x')$, can be assumed for the slick, e.g. as in Zalosh (1974), and a first BEM solution can be calculated for the underlying flow, providing ψ'_o. F_o is then calculated, with $\tan\beta_o = \eta'_{ox'}$ and an improved slick shape η_1 is obtained using (3.44). This process is repeated until convergence is reached.

In applications, the slick is represented by N_{ow} vortex elements along the oil-water interface. Slick geometry is thus defined at the center points of these elements. BEM computations are also carried out in a discretized geometry in which nodes are defined along the boundary. For the slick interface boundary Γ_s, the BEM nodes will be selected at locations identical to the nodes defining vortex elements. For each iteration, Eq. (3.44) is

[3] Note that for small current velocity, the dynamic pressure in (3.40) can be neglected and we get,

$$\eta'(x') = \left\{ \frac{s}{1-s} \int_0^{x'} C'_f(\xi)\, d\xi \right\}^{1/2} \tag{3.41}$$

which directly provides the shape of the slick due to purely frictional effects.

thus applied to the N_{ow} nodes defining the slick interface. To accelerate convergence and limit sawtooth oscillations of the slick shape, after each iteration, the geometry calculated at the nodes using (3.44) will be fitted using a Least Square Method to a smoother "simplified" slick shape, function of only a few parameters, including the slick angle at the leading edge and the slick depth far away from the leading edge.

3.2.4 Friction coefficient calculation

According to the classical laminar Boundary Layer theory (e.g., Batchelor, 1967) applicable to smooth slender bodies, the friction coefficient is a simple function of a Reynolds number **Re** based on the tangential velocity and the (arclength) distance s from the leading edge of the flow,

$$\mathbf{Re} = \frac{U_{ws}\, s}{\nu_w} \tag{3.45}$$

where ν_w denotes the water kinematic viscosity.

We have,

$$C_f = \frac{0.73}{\sqrt{\mathbf{Re}}} = \varepsilon \left(U_{ws}(s)\, s\right)^{-1/2} \qquad \text{with } \varepsilon = 0.73\sqrt{\nu_w} \simeq 0.00073 \tag{3.46}$$

If one neglects dynamic effects (i.e., $p'_D = 0$ and by (3.35) $U'_{ws} = 1$), the slick shape purely due to friction can be found using Eq. (3.41). With (3.46), assuming $s' \simeq x'$, we get,

$$\eta'(x') = \frac{s}{1-s}\sqrt{2\varepsilon}\, x'^{1/4} \quad \text{and} \quad \eta'_{x'}(x') = \frac{s}{1-s}\sqrt{\frac{\varepsilon}{8}}\, x'^{-3/4} \tag{3.47}$$

Eq. (3.47) predicts a slick shape which is both unbounded for large x' and has a vertical tangent at the leading edge ($x' = 0$). These results are not quite realistic if one compares them to experiments. Furthermore, comparing the general variation of C_f given by Eq. (3.46) when $U'_{ws} = 1$ (i.e. $C_f \propto s^{-1/2}$) to results calculated by Milgram and Van Houten (1978) for actual slicks, one sees that the true variation of C_f is much more complex along the slick, particularly in the headwave region, than predicted by this simplified (purely frictional) equation.

Thus, as concluded by Milgram and Van Houten, dynamic pressure plays an important role in the headwave region in determining slick shape. This also means that U_{ws} in this region exhibits significant variations and so do **Re** and C_f. This justifies using the complete iterative procedure (3.44) to calculate the initial slick shape in the model, together with a representation of C_f similar to Eq. (3.46). Now, for a more accurate prediction of C_f, it will be necessary to introduce a representation of the BL along the slick which includes both laminar and turbulent regimes. This will be done as part of Phase II of this project.

Chapter 4

Model test and validation

4.1 Principle of model validation

Due to the complexity of the oil containment problem, it is difficult at this stage to independently test various numerical aspects of the model, for both accuracy and convergence, on fully realistic test cases. Moreover, there is not, to our knowledge, any detailed experimental data available for oil slick evolution that could be directly compared with model predictions.

To proceed with model validation and testing, it was decided instead to separately assess the accuracy of specific aspects of the numerical model, using simpler test cases having physical features similar to the oil containment problem by a boom, for which both analytical and experimental data are available.

The first test case deals with the periodic shear instability of a two-fluid system, also known as a Kelvin-Helmholtz (KH) instability. Through a detailed analysis of the relevant literature for this problem (e.g., Drazin *et al.*, 1966; Drazin, 1970; Van de Vooren, 1980; Rangel and Sirignano, 1988), it was found that the periodic KH problem produced instability patterns similar to those occurring in the headwave of an oil slick contained by a boom (see Chapter 1). In order to simulate the KH problem, however, the model had to be slightly modified to account for periodic lateral boundary conditions and periodic CPV singularity, while keeping most of its numerical procedures unchanged (e.g., for time updating of geometry and vorticity in the interface). In doing so, a practical tool was constructed to test and validate modeling assumptions and analyze propagation of errors with time. In a following section, we explain how the model was modified to address the periodic KH problem and give results of computations for two selected sets of parameter values corresponding to examples treated by Rangel and Sirignano (1988).

A second test case was selected for the pure headwave instability in deep water of a semi-infinite oil slick over a uniform water flow (i.e., a slick without a boom modeled using 3 si sheets and 2 sd sheets; Fig. 3.1). This case is similar to the one that Zalosh (1974) studied with an equivalent but less accurate model. It was found that the mechanism of roll-up of the vortex sheet in the headwave was very similar to the one occurring for a slick contained by a boom. In a following section, we explain how the model is used to solve the

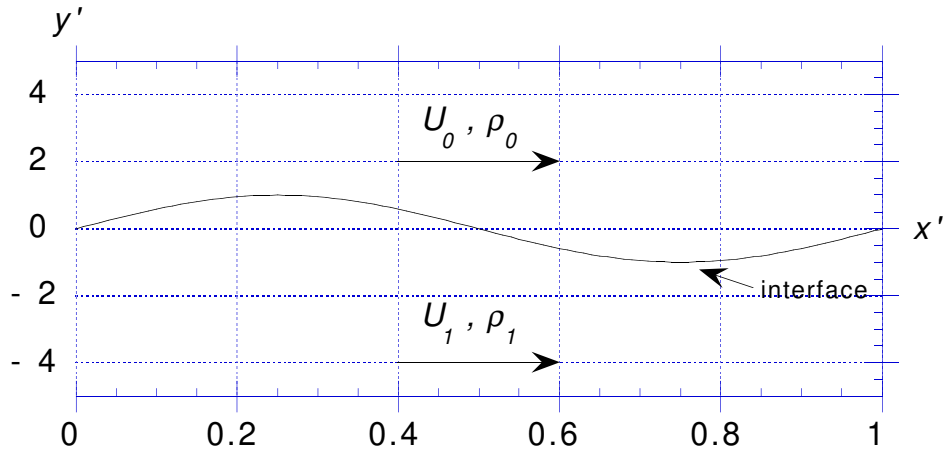

Figure 4.1: Sketch of computational set-up for periodic Kelvin-Helmholtz instability. U_o, U_1 are uniform velocities and ρ_o, ρ_1 are densities of fluid 0 and 1, respectively.

headwave instability problem (particularly the selection of the initial slick shape) and give results for cases corresponding to those modeled by Zalosh (1974).

4.2 Periodic KH instability

New formulations for the Cauchy Principal Values (CPV) integrals for *periodic sinusoidal disturbances* were derived and both the explicit and implicit time updating methods were tested in these applications.

4.2.1 Overview

We consider a two-layer stratified system of infinite extension in the x direction made of homogeneous inviscid fluids with density ρ_o (e.g., the oil) and ρ_1 (e.g., the water) and uniform horizontal velocity U_o and U_1, respectively (Fig. 4.1). An initial sinusoidal disturbance of wavelength λ, $\eta(x) = \varepsilon \sin 2\pi x/\lambda$, is specified on the interface between both fluids, with initial vorticity distribution corresponding to the velocity discontinuity (see Section 4.2.4).

This problem was solved by Lamb (1932) in a linear framework (see p. 373 and p. 461; see also Leibovich, 1976). He found that a periodic disturbance would always be unstable and grow exponentially with time if,

$$\Delta U = \mid U_o - U_1 \mid > \frac{1+s}{\sqrt{s}}\, c_o \tag{4.1}$$

where,

$$c_o = \left(\frac{1}{1+s} \{(1-s)\frac{g}{k} + \sigma_{o1}\frac{k}{\rho_1}\} \right)^{1/2} \tag{4.2}$$

the speed of propagation of interfacial waves, where, $k = 2\pi/\lambda$, is the wavenumber of the interfacial perturbation waves, $s = \rho_o/\rho_1$ and σ_{o1} is the interfacial tension coefficient.

Another way of expressing condition (4.1) is, $W < 1$ with,

$$W = \{(1-s)\frac{g}{k} + \sigma_{o1}\frac{k}{\rho_1}\}\frac{1+s}{s(\Delta U)^2} = \frac{(1+s)^2}{s}\frac{c_o^2}{(\Delta U)^2} \tag{4.3}$$

According to Eq. (4.1), the growth of the instability will be maximum for a minimum value of c_o. Calculating $dc_o/dk = 0$ in Eq. (4.2), we see that the minimum value of c_o is achieved for a wavelength,

$$\lambda_m = 2\pi\left(\frac{\sigma_{o1}}{\rho_1 g(1-s)}\right)^{1/2} \tag{4.4}$$

and takes the value,

$$c_{om} = \left(\frac{2}{1+s}\sqrt{\frac{\sigma_{o1}}{\rho_1}g(1-s)}\right)^{1/2} \tag{4.5}$$

the critical interfacial wave velocity.

If we select $\lambda = \lambda_m$ from (4.4) as the wavelength of the interfacial instability and $W = W_m = 1$ (given by Eq. (4.3) with $c_o = c_{om}$, from Eq. (4.5), and $k = 2\pi/\lambda_m$), we can calculate the critical velocity discontinuity causing instability, ΔU_{cr}, and see whether there is (linear) instability or not for a specified discontinuity ΔU. We get,

$$\Delta U_{cr} = \left(2\frac{1+s}{s}\sqrt{\frac{\sigma_{o1}}{\rho_1}g(1-s)}\right)^{1/2} \tag{4.6}$$

Lamb's solution detailed above assumes that the height of interfacial waves is infinitesimal. This is only an approximation particularly if the instability is free to develop for a long enough time. As a first approximation, however, this solution can be used to predict the threshold velocity ΔU likely to cause initial instability of interfacial waves. Moreover, despite their limitations, Lamb's equations contain the correct physical parameters influencing interfacial instability (i.e., fluid density ratio, interfacial tension and gravity) that will be used in the more exact solution presented hereafter.

4.2.2 Governing equations

Using the present model, no approximation is made on the size of interfacial waves and computations can be pursued up and into the roll-up of vortex sheets representing the interface (e.g., Figs. 4.2., 4.3).

Since a velocity discontinuity exists at the interface (i.e., a shear layer), a vorticity distribution is created along the interface. Hence, for both (ideal) fluids in the system, the velocity potential obeys a Poisson equation (i.e., not the simple Laplace's equation of classical ideal fluid cases). It can be shown that the flow velocity induced in both fluids due to the interfacial vorticity can be calculated using Biot-Savart's law (2.3) (e.g., Batchelor,

1967, pps. 84 and 527). In doing so, it is assumed that the interface is well represented by a vortex sheet.

For a periodic disturbance of wavelength λ on the interface with infinite extension in the s direction, Eq. (2.3) reads, in complex form,

$$u(z) - i\,v(z) = \frac{i}{2\pi} \int_{-\infty}^{+\infty} \gamma(s)\, \frac{1}{z - z'}\, ds \tag{4.7}$$

where, $i = \sqrt{-1}$, $z = x + iy$, $z' = x' + iy'$, and $s = s(z')$. Due to periodicity, Eq. (4.7) can be transformed into,

$$u - i\,v = \frac{i}{2\pi} \int_0^{\lambda} \gamma(s) \sum_{n=-\infty}^{\infty} \frac{1}{z - z' + n\lambda}\, ds \tag{4.8}$$

or, following Van de Vooren (1980), into,

$$u - i\,v = \frac{i}{2\lambda} \int_0^{\lambda} \gamma(s) \cot\left[\frac{\pi}{\lambda}(z - z')\right] ds \tag{4.9}$$

After some algebraic transformations (Van de Vooren, 1980) and introduction of dimensionless variables, $\xi = x/\lambda$, $\eta = y/\lambda$, and $\tau = t\,\Delta U/\lambda$, Eq. (4.9) becomes,

$$\begin{aligned} u &= \Delta U \frac{d\xi}{d\tau} = \frac{1}{2\lambda} \int_0^{\lambda} \frac{\sinh 2\pi(\eta - \eta')}{\cosh 2\pi(\eta - \eta') - \cos 2\pi(\xi - \xi')}\, \gamma(s)\, ds \\ v &= \Delta U \frac{d\eta}{d\tau} = -\frac{1}{2\lambda} \int_0^{\lambda} \frac{\sin 2\pi(\xi - \xi')}{\cosh 2\pi(\eta - \eta') - \cos 2\pi(\xi - \xi')}\, \gamma(s)\, ds \end{aligned} \tag{4.10}$$

Eq. (4.10) can be used in this form to time march the geometry of the interface, defined by points (ξ, η), provided integrals on the right hand side of the equation are calculated as a function of time. As described in Chapter 2, this can be done by assuming that the interface (vortex sheet) is made of N segments with piecewise constant vorticity density γ_j. This is similar to the discretization used in Eq. (2.7). The velocity induced at the mid-point of a segment i is thus given by $(i, j = 1, ..., N)$,

$$\begin{aligned} u_i &= \frac{1}{2\lambda} \sum_{j \neq i} \Gamma_j \frac{\sinh 2\pi(\eta_i - \eta_j)}{\cosh 2\pi(\eta_i - \eta_j) - \cos 2\pi(\xi_i - \xi_j)} + \tilde{u}_i \\ v_i &= -\frac{1}{2\lambda} \sum_{j \neq i} \Gamma_j \frac{\sin 2\pi(\xi_i - \xi_j)}{\cosh 2\pi(\eta_i - \eta_j) - \cos 2\pi(\xi_i - \xi_j)} + \tilde{v}_i \end{aligned} \tag{4.11}$$

where $\tilde{u}_i$ and $\tilde{v}_i$ denote CPV integrals resulting from singularities occurring when the source point (x_i, y_i) coincides with the integration point (x_j, y_j) (i.e., self-induced velocity contributions; see Section 2.2.2). These CPV integrals are calculated in the next section.

4.2.3 Calculation of self-induced velocity contributions for piecewise constant element

As pointed out by Van de Vooren (1980), there is a need for accurately evaluating self-induced velocity contributions resulting from singularities in (4.10) when the source point coincides with the integration point. It seems, however, that a number of studies have avoided this problem either by using (less accurate) point vortices (e.g., Zalosh, 1974, 1976), which do not have self-induced velocity (see Section 2.2.1) and/or by regridding discretization points at equal distance in such a way as to (knowingly or unknowingly) cancel self-induced velocity contributions (Rangel and Sirignano, 1988, 1991; see also the discussion in Fink and Soh, 1974, and in Section 2.2.2).

Starting from the complex form (4.9) of the periodic Biot-Savart law, the CPV integrations over segment i of length Δs_i give,

$$\tilde{u}_i - i\,\tilde{v}_i = \frac{i}{2\lambda}\int_{s_{i-1/2}}^{s_{i+1/2}} \gamma_i \cot\left[\frac{\pi}{\lambda}(z_i - z')\right] e^{-i\theta_i} dz' \tag{4.12}$$

where for a straight line segment we have used, $ds = dz' e^{-i\theta_i}$, with θ_i the angle between segment i and the x-axis.

Eq. (4.12) can be readily integrated to yield,

$$\tilde{u}_i - i\,\tilde{v}_i = -\frac{\Gamma_i}{2\pi\Delta s_i}\left(\sin\theta_i - \cos\theta_i\right) \ln\left|\frac{\sin\left[\pi(z_i - z_{i+1/2})/\lambda\right]}{\sin\left[\pi(z_i - z_{i-1/2})/\lambda\right]}\right| \tag{4.13}$$

where, $\Gamma_i = \gamma_i \Delta s_i$, is the total vorticity of segment i.

Separating real and imaginary parts of (4.13), we obtain,

$$\begin{aligned}
\tilde{u}_i &= \frac{\Gamma_i}{2\pi\Delta s_i}\left\{\cos\theta_i \arctan P - \frac{\sin\theta_i}{2}\ln|\,Q\,|\right\} \\
\tilde{v}_i &= -\frac{\Gamma_i}{2\pi\Delta s_i}\left\{\sin\theta_i \arctan P + \frac{\cos\theta_i}{2}\ln|\,Q\,|\right\}
\end{aligned} \tag{4.14}$$

with,

$$\begin{aligned}
P = &\Big(\left\{\cot\left(\pi\Delta s_{i+1/2}\cos\theta_i\right)\tan\left(\pi\Delta s_{i+1/2}\sin\theta_i\right)\right\} - \\
&\left\{\cot\left(\pi\Delta s_{i-1/2}\cos\theta_i\right)\tan\left(\pi\Delta s_{i-1/2}\sin\theta_i\right)\right\}\Big) \Big/ \\
&\Big(1 + \left\{\cot\left(\pi\Delta s_{i+1/2}\cos\theta_i\right)\tan\left(\pi\Delta s_{i+1/2}\sin\theta_i\right)\right\} \\
&\left\{\cot\left(\pi\Delta s_{i-1/2}\cos\theta_i\right)\tan\left(\pi\Delta s_{i-1/2}\sin\theta_i\right)\right\}\Big)
\end{aligned} \tag{4.15}$$

and,

$$Q = \frac{\sin^2\left(\pi\Delta s_{i+1/2}\cos\theta_i\right)\cosh\left(\pi\Delta s_{i+1/2}\cos\theta_i\right)}{\sin^2\left(\pi\Delta s_{i-1/2}\cos\theta_i\right)\cosh\left(\pi\Delta s_{i-1/2}\cos\theta_i\right)} \tag{4.16}$$

It can be shown that Eqs. (4.14)-(4.16) for the self-induced velocities generalize the equations derived by Van de Vooren (1980), using a Taylor series expansion method truncated to first-order. Hence, the present method is both more general and more accurate than Van de Vooren's method.

Using Eqs. (4.11) and (4.14)-(4.16), the total velocity induced by a vorticity distribution on the interface can be calculated along the interface and, if needed, in the bulk of both fluids. Selection of the initial vorticity distribution on the interface is discussed in the next section.

4.2.4 Initial vorticity distribution

Using linear theory (Lamb, 1932), the initial distribution of vorticity density is determined on the interface for the KH problem as ($i = 1, ..., N$),

$$\gamma_i = \frac{1}{N\Delta s_i}\left(1 + 2\pi\varepsilon\left\{\kappa\sin(2\pi\xi_i) - 2\frac{\sqrt{s(1-W)}}{(1+s)}\cos(2\pi\xi_i)\right\}\right) \tag{4.17}$$

where κ is the Atwood number defined in Section 2.3.2, ε is the initial amplitude of the interfacial wave, and W (< 1) is given by Eq. (4.3) for the selected values of physical parameters.

Eqs. (4.17) and (4.3) were used by Rangel and Sirignano (1988), with $g = 0$, to specify initial vorticity in their solution of KH instability problems without gravity effects [1].

If the two-fluid system is made of identical fluids with different velocities, we have $s = 1$, $\kappa = 0$, and $W = 0$ and, hence, the initial vorticity distribution is given by,

$$\gamma_i = \frac{1}{N\Delta s_i}\left\{1 - 2\pi\,\varepsilon\,\cos(2\pi\xi_i)\right\} \tag{4.18}$$

Zalosh (1976) used this simpler equation to specify the initial vorticity distribution in his solution of the KH-problem. Since he used two different fluids, however, this led to an incorrect specification of the initial disturbance, which might partly explain why he could not achieve sufficient accuracy and stability in his computations.

4.2.5 Summary of computational techniques

A computational test case for the KH instability problem is defined by selecting values of physical parameters : ρ_o, ρ_1, ΔU, and σ_{o1}. Due to the spatial periodicity of the KH problem, a domain representing only one wave length λ is modeled in the computations and numerical parameters are selected as : (i) the initial number N of piecewise-constant vortex elements

[1] Note that, in this study, computations were carried out using an incorrect coefficient in the equation for time updating of the vorticity (i.e., Eq. similar to (2.28)); this was later corrected by Rangel and Sirignano (1991).

on the interface, of initial length $\Delta s_o = \lambda/N$; and (ii) the initial time step, Δt_o. The latter is found according to Eq. (3.4), in which we assume that the initial sheet velocity is, by definition, the average of fluid 0 and 1 velocities (see Section 2.3.2), i.e., $\Delta U/2$ (for $U_o = 0$ in the present case), and the Courant number $C_o = 0.5$; we thus get, $\Delta t_o = \lambda/(N\Delta U)$.

The initial vorticity distribution on the interface is calculated using Eqs. (4.17) and (4.3) for a two-fluid system (second application below) and Eq. (4.18) for a problem with the same fluid for both layers (first application below). In the present computations, as in Rangel and Sirignano (1988), we use $\varepsilon = 0.025$ to define the initial perturbation on the interface, and the initial shape of the interface is selected as $\eta(x) = \varepsilon \sin 2\pi x/\lambda$.

Due to periodicity, corner points at both extremities of the modeled interface-sheet (i.e., points 1 and N) must always behave similarly in the computations, i.e., have the same y-coordinates, x-coordinates separated by λ, and have identical velocity, acceleration, and vorticity. Lateral boundary conditions are used to "enforce" these requirements in the model. For instance, horizontal coordinates are constrained as,

$$(x_N - x_1) + \Delta s_{1/2} \cos\beta_1 + \Delta s_{N+1/2} \cos\beta_N = \lambda \tag{4.19}$$

The interface evolution is tracked as a function of time by iteratively using the time updating procedure (3.1)-(3.3) (for the explicit time updating scheme). For each time step, the velocity on the interface is calculated using Eqs. (4.11), with (4.14)-(4.16), and the acceleration is calculated using time derivatives of these equations.

Tangential derivatives along the interface are calculated using the 4th-order sliding polynomial and the spline procedures described in Section 3.1.4. In the present computations, the hybrid method is used in combination with periodicity conditions expressed between nodes $(1+j)$ and $(N-j)$, $(j = 0, ..., 3)$ of the computational domain. This hybrid method was found to eliminate errors and instabilities of the solution that were first observed, particularly at both extremities of the interface, when only one of the above methods was used.

4.2.6 Computational results for interface evolution

Computations were performed using $U_o = 0$ (i.e., a still upper layer) and $U_1 = 0.25$ m/s (which is larger than the critical value for oil/water of about 0.15 m/s; see below), for two cases : (i) $s = \rho_o/\rho_1 = 1$ (water/water interface; same fluid) and no surface tension ($\sigma'_{o1} = 0$); and (ii) $s = 0.90$ (light oil/water interface; two-fluid system) and an average surface tension $\sigma'_{o1} = 0.0237$ N/m (oil/water value). In the present computations, $N = 55$ piecewise-constant vortex elements are first used to discretize the interface for both cases, and the mesh Courant number is set to $C_o = 0.5$, in both cases. Figure 4.2 (a) shows nodes between vortex elements in the discretization after 11 time steps.

In the first case (i), with a water-water system, Eqs. (2.28) or (3.9) would show that $d\Gamma_i/dt = d\,g_i/d\,\tau = 0$, i.e., the vorticity, is constant as a function of time. This case in fact represents a very unstable limiting case of KH instability computations (Rangel and Sirignano, 1988); one for which the instability grows with the same time rate for any

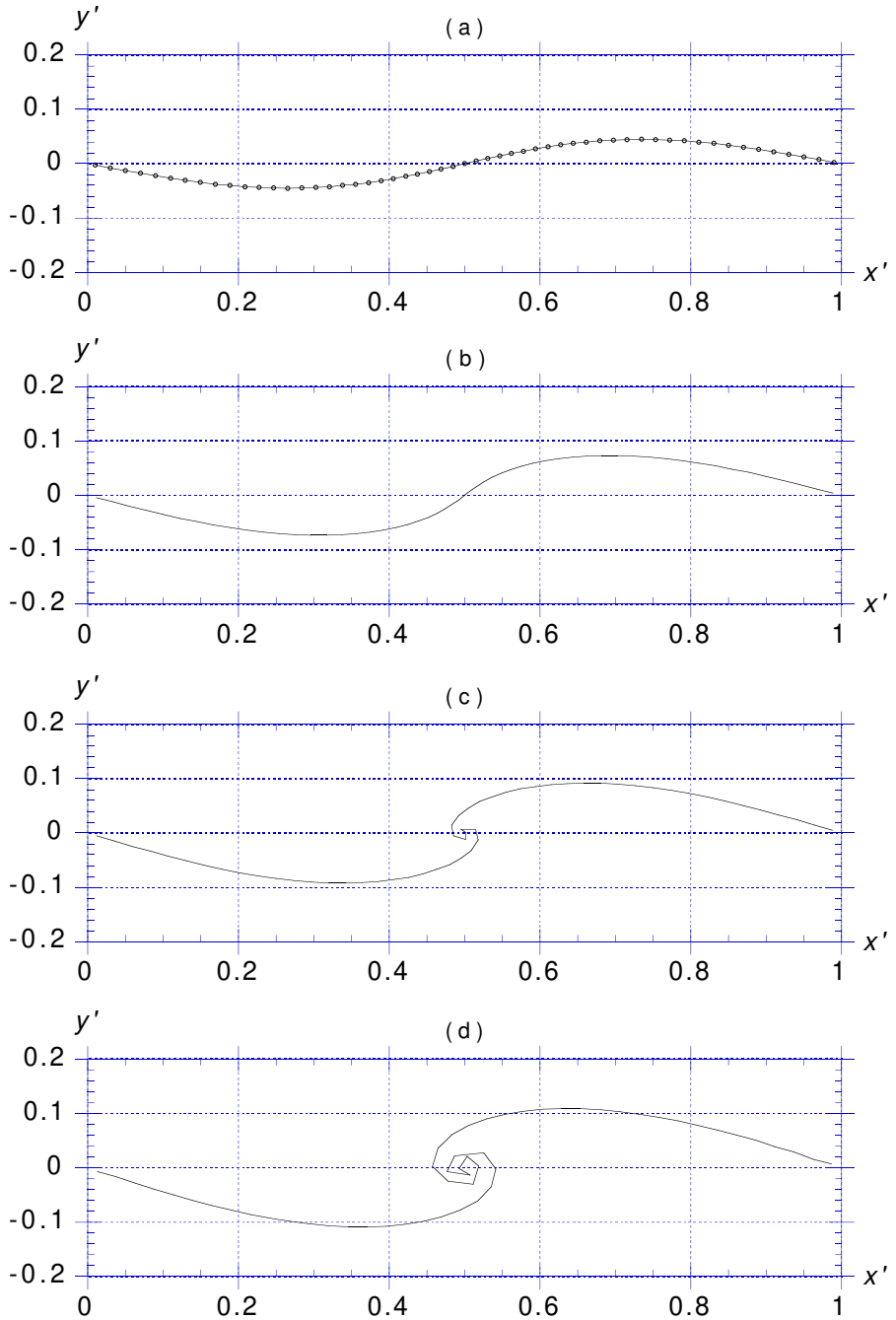

Figure 4.2: Interface shape $x' = x/\lambda$ and $y' = y/\lambda$ for KH instability computations in a set-up similar to Fig. 4.1 with $U_o = 0$ and $U_1 = 0.25$ m/s, $\rho_o/\rho_1 = 1$ (same fluid) and $\lambda = 1$ m and no surface tension. The initial time step is $\Delta t_o = 0.0727$ s and the initial perturbation is a sinusoidal wave with vorticity distribution according to Eq. (4.18), with $\varepsilon = 0.025$. Results are for $t =$ (a) 0.8; (b) 1.53; (c) 1.91; and (d) 2.24 s; corresponding to 11, 21, 31, and 43 varying time steps, respectively. The interface was discretized using $N = 55$ piecewise-constant vorticies and $\mathcal{C}_o = 0.5$. (○) in figure (a) denote nodes between vortex elements.

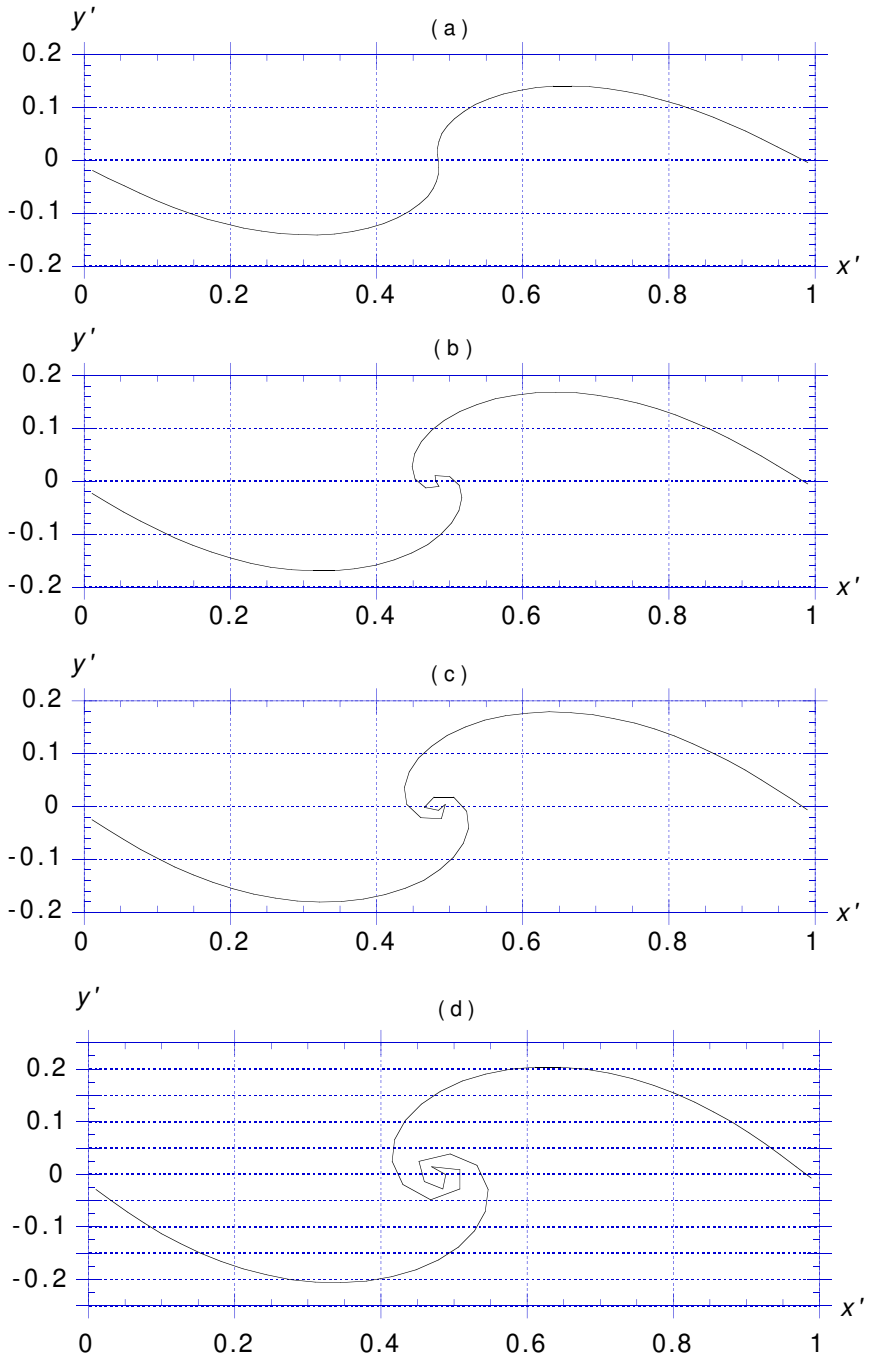

Figure 4.3: Same results as in Fig. 4.2 for $\rho_o/\rho_1 = 0.9$, a surface tension $\sigma_{o1} = 0.0237$ N/m, and $\lambda = 0.031$ m (water-oil; ripple scale). The initial time step is $\Delta t_o = 0.00225$ s and the initial perturbation is as in Fig. 4.2. with the initial vorticity distribution from Eq. (4.17). Results are for $t =$ (a) 1.74; (b) 1.85; (c) 1.89; and (d) 1.98 10^{-2} s; again corresponding to 6, 12, 16, and 22 varying time steps, respectively.

wavelength. For this case, due to the absence of surface tension and density difference at the interface, the analysis of the most unstable wavelength λ_m presented above is irrelevant. Hence, λ can be arbitrarily selected and results for any wavelength should be expected to be self-similar. To confirm this, computations were performed for $\lambda = 0.01$, 0.1, 1, and 5 m and non-dimensional interface profiles were found to be closely identical in all cases, as a function of non-dimensional time. In the following, we present results obtained for case (i) with $\lambda = 1$ m. For this value, the initial time step is $\Delta t_o = 0.0727$ s (or $\Delta\tau_o = 0.01818$; in fact the nondimensional time step does not depend on wavelength).

In the second case (ii), following the linear analysis by Lamb (1932), the wavelength is selected from Eq. (4.4), as $\lambda = \lambda_m$, which provides the maximum growth rate of the (linear) instability, with interfacial wave velocity c_{om} given by (4.5). This gives a value $\lambda = 0.0309$ m and, hence, $\Delta t_o = 0.00225$ s or $\Delta\tau_o = 0.0182$ (note that dimensionless time steps are identical to $1/N$ for both cases (i) and (ii)). This centimetric value of λ corresponds to an instability at the ripple scale (with $c_{om} = 0.0712$ m/s). As a verification of the (linear) instability of the problem for case (ii), we would also get from Eq. (4.3) $W = W_m = 0.325$ and from Eq. (4.6) $\Delta U_{cr} = 0.143$ m/s, i.e., we do have $W < 1$ and $\Delta U > \Delta U_{cr}$.

Results in Figs. 4.2 and 4.3 show the typical KH instability by overturning; intense roll-up of the vortex sheet on the interface, for water/water and oil/water cases, respectively. In the first case, the time step value stays closely equal to its initial value $\Delta\tau_o = 0.01818$ for 23 time steps, up to $t = 1.67$ s (i.e., just slightly beyond the time of Fig. 4.2 (b)). For later time, due to the overturning of the interfacial wave and the resulting shortening of vortex elements length, however, the time step value progressively reduces according to the adaptive time step procedure (3.4), down to $\Delta\tau = 0.00926$ for $t = 2.24$ s (Fig. 4.2 (d)). A similar variation in time step size was observed for the second case. Note that, in earlier works by Zalosh (1976) and Rangel and Sirignano (1988), a constant time step value was used. This prevented adjusting the level of accuracy in their models when interfacial instabilities occurred.

Overall, for both cases, numerical results are smooth and well-behaved, even when vortex sheet elements get very close to each other (see, e.g., Figs. 4.2 and 4.3 (d)). This confirms the correct treatment of CPV singularities in the model.

For both cases in Figs. 4.2 and 4.3, the number of vortex elements on the interface was first decreased to $N = 40$ and then increased to $N = 70$, and the initial time step was adjusted accordingly. Computations were performed for these discretizations. Figure 4.4 (a) shows a comparison of free surface shapes obtained at $t = 2.24$ s for the same case as in Fig. 4.2 and for the three selected discretizations. The agreement between the three results is quite good, except in the small central region where intense roll-up of VS's occurs. Figure 4.4 (b) shows the evolution of the interfacial amplitude as a function of time, for the three discretizations. For both the finer and the coarser discretizations, interfacial amplitudes stay within 2% of the results for $N = 55$. Hence, results are not significantly affected by a slight decrease or an increase in resolution which confirms both the convergence and stability of the numerical model, particularly compared to earlier works by Zalosh (1976) and Rangel and Sirignano (1988) where computed results showed irregular behavior when

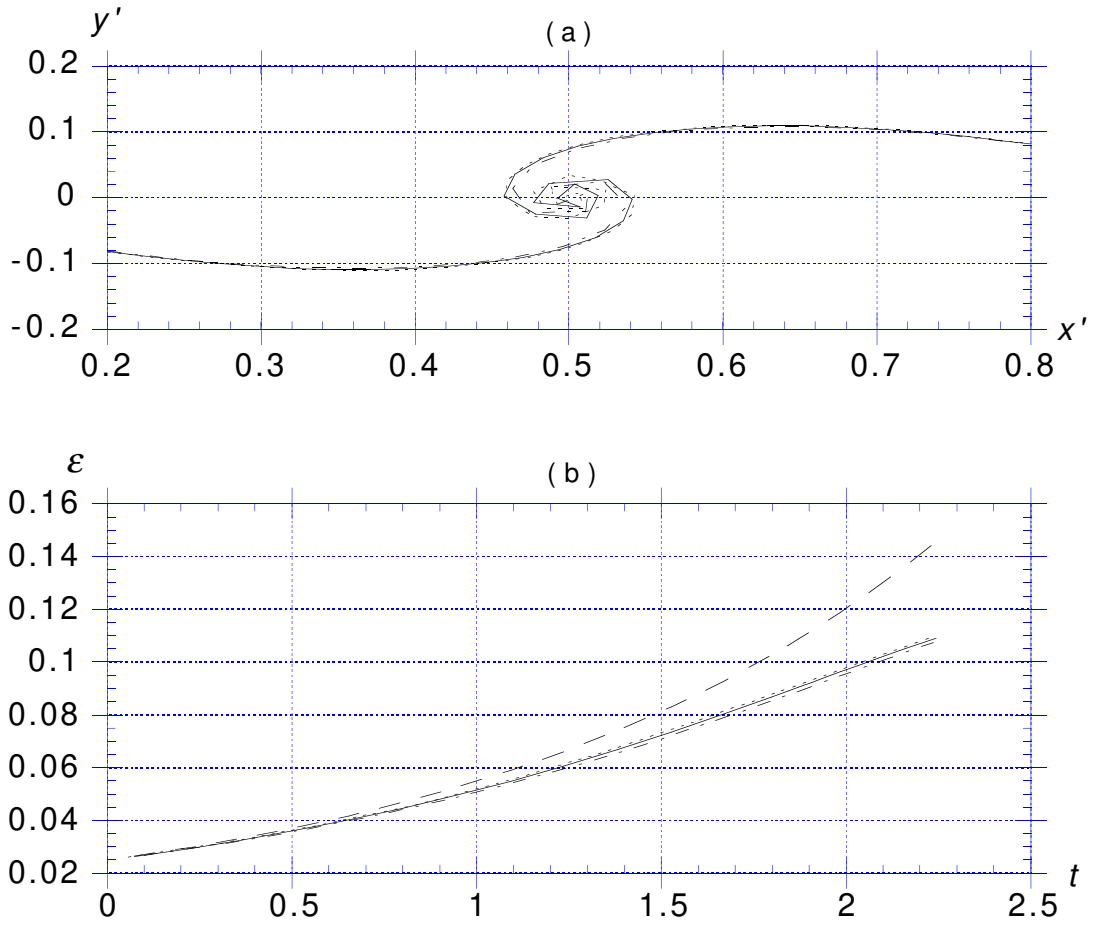

Figure 4.4: Same computations as in Fig. 4.2 for N = (— - —) 40; (——) 55; and (- - - - -) 70, vortex elements on the interface; with : (a) interface shape at $t = 2.24$ s; (b) growth of interfacial amplitude ε as a function of time t compared to (—- —-), the linear growth rate (Lamb, 1932).

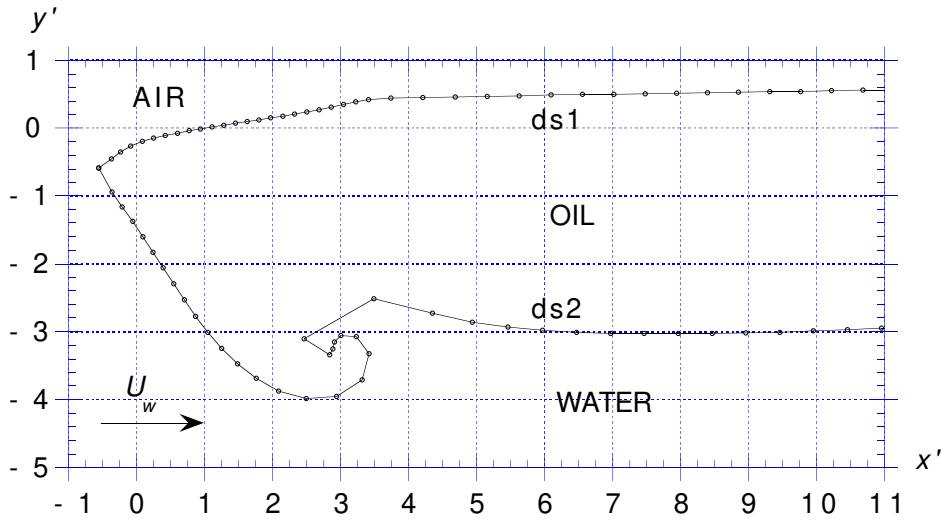

Figure 4.5: Sketch of computational domain for headwave instability of an oil slick, with definition of main parameters : U_w = water velocity with respect to slick ($U_o = 0$); air velocity can be set to U_a and interfacial tensions to σ_{oa} and σ_{ow}; densities are $\rho_a = 0$, ρ_o and ρ_w; si1, si2, si3 (not shown) = three semi-infinite vortex sheets; ds1, ds2 = piecewise-constant discretized vortex sheets; ∘ = centers of discretized vortex elements.

the size of vortex elements was too small. Finally, note the differences in Fig. 4.4 (b) between the amplitude growth rates obtained with the present nonlinear model and the rate predicted by linear theory (Lamb, 1932; in fact simply $\propto \exp(\pi \Delta U t/\lambda)$ in the present case). Clearly, for sufficiently larger time, nonlinearity increases and the instability grows slower in the nonlinear model than predicted by linear theory. This confirms earlier findings that nonlinearity provides stabilizing effects for the KH problem (e.g., Zalosh, 1976; Rangel and Sirignano, 1988).

Comparing both figures 4.2 and 4.3, one can see that the second case, with oil/water and surface tension, leads to a relatively larger scale of instability (in non-dimensional values, i.e., with respect to the selected wavelength) that also develops at a faster (non-dimensional) time rate than in the first case. The interface shape is up/down symmetrical in the first case (Fig. 4.2), where buoyancy does not play a role ($s = 1$), and slightly asymmetrical in the second case (see Fig. 4.3 (d)) due to buoyancy effect ($s = 0.9$). The present results are qualitatively similar to those obtained by Rangel and Sirignano (1988). The latter study, however, did not include gravity and used several incorrect coefficients in the vorticity updating equation. Hence, a direct comparison is not feasible.

4.3 Deep water headwave instability

This case corresponds to the problem solved by Zalosh (1974) and sketched in Fig. 4.5. A semi-infinite oil slick with zero initial velocity $U_o = 0$ is subjected to a water flow velocity U_w (and an air flow U_a). An instability soon develops in the front part of the slick, and propagates downstream as a headwave which quickly overturns and rolls-up on itself in a way similar to KH instability waves calculated in the previous section.

The computational model used for this case is the original model introduced in Chapters 2 and 3. Errors made by Zalosh in his model for Eq. (2.28) for the interface evolution were corrected and the present, more accurate discretization/updating, method was used. In particular, the sliding/spline method was used to calculate tangential derivatives along the interface and velocities were calculated along the interface using Eq. (2.9). Unlike Zalosh, an exact representation of self-induced velocities of vorticies was used.

Note that, to overcome problems caused by the lack of representation of the self-induced velocities, Zalosh introduced the concept of a viscosity-core, in which contributions of individual point vortices in the discretized Biot-Savart equations (2.5) were multiplied by a term, $[1 - \exp(-r_{ij}^2/R_c^2)]$ (in which R_c is the "core radius"), i.e., providing a very small contribution to the velocity field for point vortices j's very close to point i. Zalosh stated that his numerical model was unstable without the use of this "damping" method. After experimenting with this method, we found that it was not needed for our model to provide both stable and accurate results, except at the three intersections between semi-infinite sheets and the piecewise-constant vortex sheets. This was thought to be due to the local mismatch between the continuous vorticity on the semi-infinite sheets and the piecewise-constant vorticity on the discretized vortex sheets. This problem will likely be eliminated in the Phase II model which will use higher-order vortex elements for the discretization of vortex sheets. For these three points, a core length equal to the distance to the first vortex element center was used.

The *initial slick shape* was selected as in Zalosh (i.e., no BEM initialization was used here; see Fig. 4.6 (o)), based on the observation of various experimental results, as,

$$\begin{aligned} \eta(x) &= D\sin(2\pi\, x/L) \qquad \text{for } 0 \le x \le L/4 \\ \eta(x) &= D \qquad\qquad\qquad\quad \text{for } L/4 \le x \le L \end{aligned} \tag{4.20}$$

where D and L are the initial depth and length of the slick headwave, respectively. Using Bernoulli's equation between the front and the back of the slick, we get,

$$D = \frac{U_w^2}{2g\,(1-s)} \tag{4.21}$$

Following the work by Von Karman (1940) for density intrusions along solid boundaries, Zalosh assumed a 60° value for the angle of the headwave at the leading edge. With this angle, Eq. (4.20) leads to $L = 3.63D$. As pointed out by Zalosh, experimental results usually show smaller angles at the leading edge, which would lead to increased values of L.

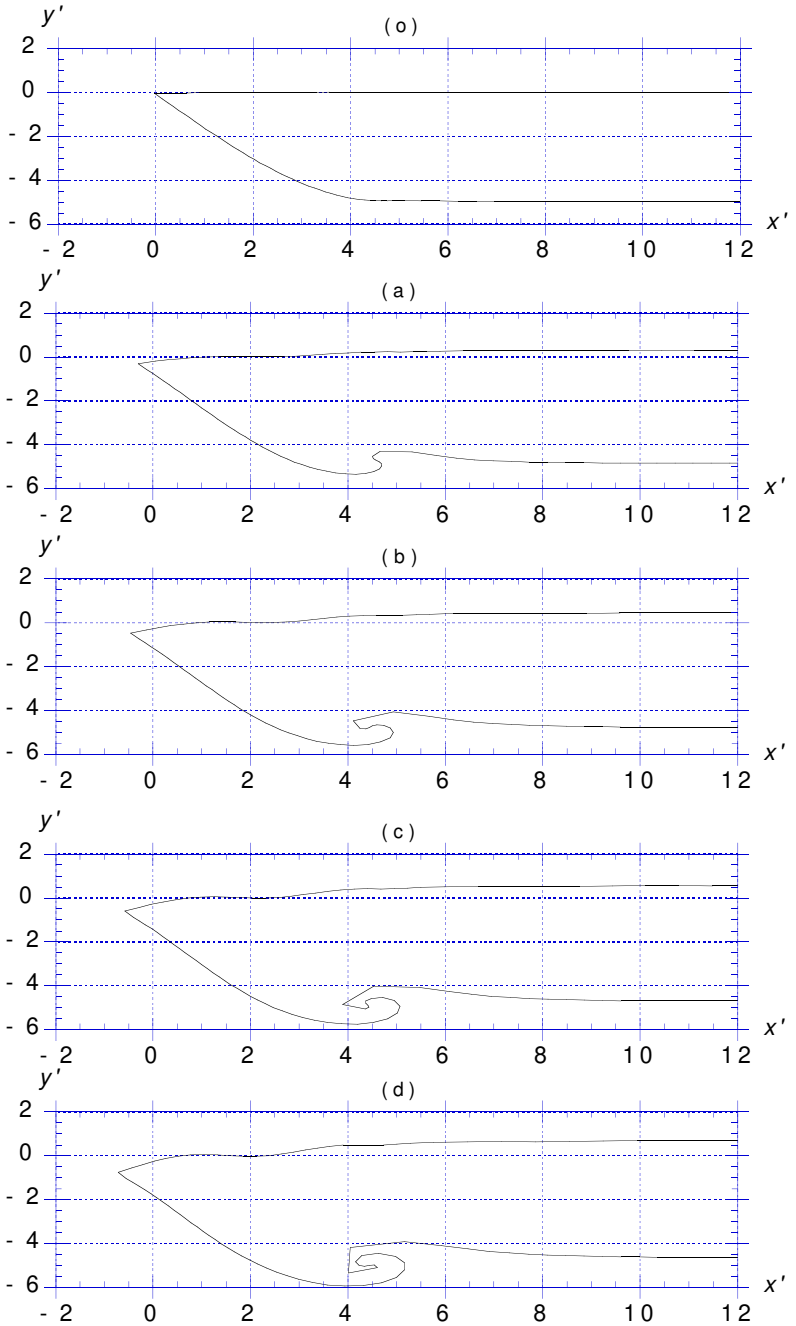

Figure 4.6: Typical results for headwave instability computations as in Zalosh (1974), in a set up similar to Fig. 4.5, with U_w = 0.25 m/s, $U_o = 0$, $U_a = 0$ m/s, $s = \rho_o/\rho_w = 0.9$, $\sigma_{ow} = 0.0237$ N/m (water-oil). Results $(D' = 5, L' = 18.15)$: (o) initial shape of the slick after one time step $t = 0.00273$ s; development of instability for $t =$ (a) 1.8; (b) 3.1; (c) 4.1; and (d) 5.2 10^{-2} s; corresponding to 5, 10, 16, and 22 varying time steps, respectively. Three semi-infinite sheets were used and interfaces were discretized with $N_a = 45$ piecewise-constant vorticies between air and oil and $N_w = 85$ between oil and water.

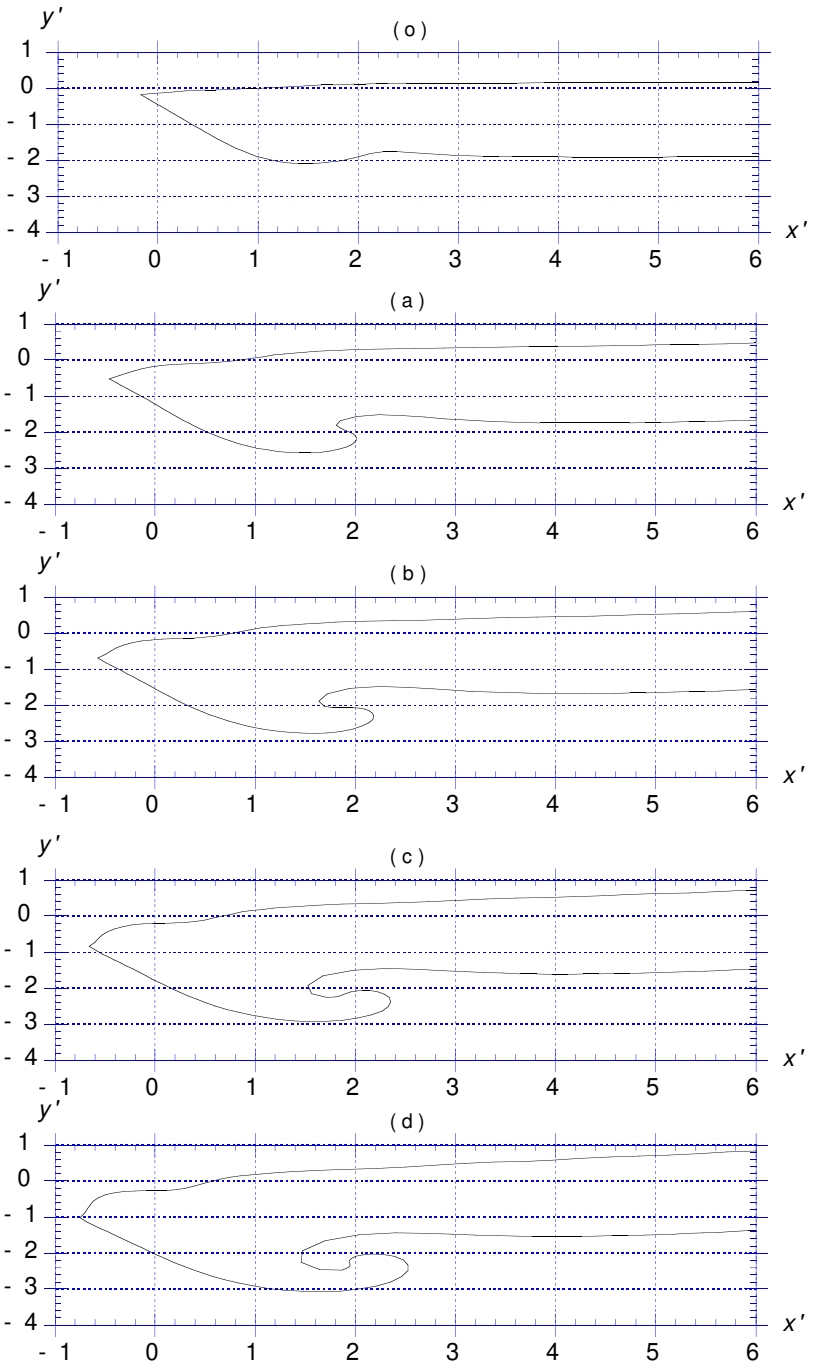

Figure 4.7: Same as in Fig. 4.6 for $\rho_o/\rho_w = 0.75$. Results $(D' = 2, L' = 7.26)$: (o) initial shape of the slick after one time step $t = 0.00109$ s; development of instability for $t =$ (a) 0.59; (b) 0.80; (c) 1.06; and (d) 1.30 10^{-2} s; corresponding to 5, 10, 16, and 22 varying time steps, respectively.

In the present case, however, we simply used the same initial shape as Zalosh's to compare our results to those he obtained.

In the computations, three semi-infinite sheets are used and interfaces are discretized using $N_a = 45$ segments with piecewise-constant vorticity between air and oil and $N_w = 85$ segments between oil and water. For each sheet, in the initial discretization, half the vortices are specified with equal arc-length spacing in the headwave region, i.e., for $0 \leq x \leq L/4$, and the other half are specified with equal arc-length spacing in the rest of the slick, i.e., for $L/4 \leq x \leq L$ (see Fig. 4.5). This provides a finer discretization in the headwave region where the main instability will occur. With this discretization, we have a minimum initial length of vortex elements equal to about $\Delta s_o = L/(2N_w)$ and an initial time step, according to Eq. (3.4), equal to $\Delta t_o = \mathcal{C}_o L/(N_w U_w)$ (assuming an initial maximum velocity of the oil-water sheet equal to $U_w/2$).

Two cases are solved for $s = 0.9$ and 0.75, assuming a surface tension $\sigma_{ow} = 0.0237$ N/m. In both cases, the water velocity is set to U_w = 0.25 m/s, which is above the critical value for oil and water, and the air velocity is set to $U_a = 0$. A length-scale $\lambda = U_w^2/g =$ 0.00637 m is used in the model (defined as in Section 3.2) and the corresponding time scale is $U_w/g = 0.02548$ s. Following Eq. (4.21), the initial slick is specified with depth $D' = D/\lambda = (5, 2)$, and length $L' = L/\lambda = (18.15, 7.26)$, for each test case, respectively. With $\mathcal{C}_o = 0.5$, initial time steps $\Delta\tau_o = \mathcal{C}_o L'/N_w = 0.107, 0.0427$, for each case, or $\Delta t_o = 0.00273, 0.00109$ s, respectively.

Results obtained in Figs. 4.6 and 4.7 are qualitatively similar to Zalosh's results but are better resolved and the developments of instabilities (roll-up) can be computed for a longer time. Model calculations are found to be both stable and accurate, without need for smoothing the interface or surface geometry or for other transformations of model outputs used in earlier studies (e.g., Zalosh, 1974).

Results of other computations (not reported here) are also found to be improved in both resolution and duration of computations when a larger number of vorticies are used on the interface. This confirms the accuracy of the CPV integrals computed for the self-induced velocities and demonstrates both the stability and the accuracy of the time updating procedures used in the present model.

Chapter 5

Conclusions and future developments

The present report dealt with Phase I model development and testing. To do so, the relevant literature and key physical phenomena relative to oil containment were analyzed. Important parameters were isolated and used to develop a numerical model of interfacial instabilities for a two-phase system consisting of a layer of oil on top of a uniform water stream.

This model relied on well-established *Vortex Sheet* dynamics methods with, however, several significant improvements compared to existing work in the literature. Key improvements included,

- the use of piecewise-constant vortex sheets (instead of point vortices) and the inclusion of self-induced velocity terms along the interfaces (with exact calculation of CPV integrals);
- the use of time updating equations for the sheet vorticity that account for inertial, gravity and surface tension effects;
- the use of a piecewise cubic-continuous representation of the geometry allowing for a more accurate calculation of higher-order tangential derivatives along interfaces, and the use of node regridding techniques;
- the use of a more accurate and stable explicit scheme, with exact calculation of vortex sheet accelerations, for time-updating of both the vorticity and the geometry of the interfaces;
- the use of a self-adaptive, time-stepping method, based on a mesh Courant number.

Applications of Phase I model presented in Chapter 4 mostly concentrated on studying two somewhat "academic" problems aimed at both testing the accuracy of the numerical procedures implemented in the model and better understanding the physics of unstable two-fluid systems; namely, the periodic Kelvin-Helmholtz instability and the semi-infinite headwave instability of a two-fluid system. These two applications showed some of the capabilities and efficiency of the model. They also gave us a solid basis for performing more complex studies including a boom and other solid boundaries like the bottom.

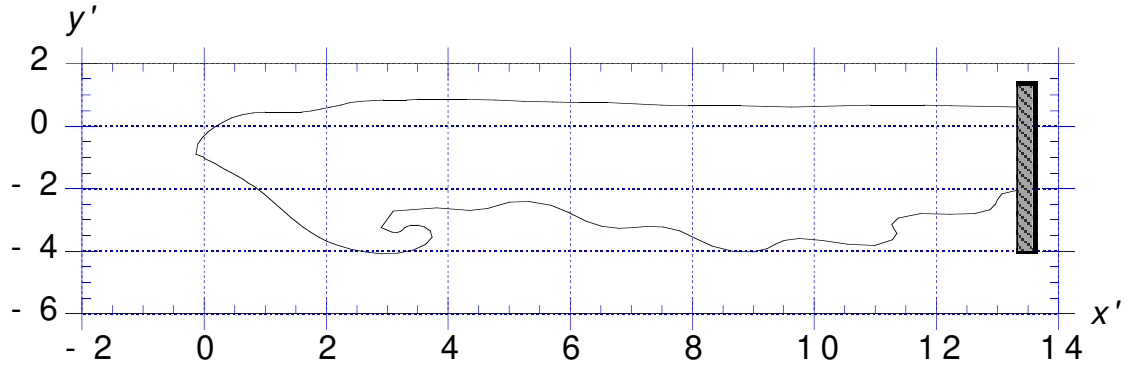

Figure 5.1: Illustration of computations with Phase I model for an oil slick contained by a boom. In this case, both a headwave and interfacial instabilities simultaneously develop.

To carry out the first application (KH problem), model equations had to be re-derived to include the spatial periodicity of the problem. Self-induced velocity terms also had to be expressed for the periodic problem. To our knowledge, such derivations have not been presented in the literature. In the second application to the headwave problem, both for sake of comparison and for simplicity, the initial shape of the oil slick was selected, somewhat arbitrarily, as in the study by Zalosh (1974). This means that the new method, outlined in Section 3.2, for calculating the initial steady-state shape of the slick has not yet been used, nor tested, in this report. It will, however, represent an essential component of the Phase II model which is currently under development and testing.

Future developments for the Phase II model, in particular, will include,

- the study of oil-water-boom systems;
- the initialization of the steady-state oil slick based on the iterative method introduced in Section 3.2;
- a computation of friction along the oil-water interface, both for the initialization of the slick shape and for the time updating of the slick geometry and dynamics; these computations will include both viscous and turbulent diffusion effects within boundary layers close to interfaces;
- using viscous/turbulent vortex sheets combining a local Navier-Stokes solver with turbulent closure models ($k - \varepsilon$ or similar);
- using higher-order vortex elements to provide better accuracy of computations along interfaces (i.e., use of non-constant vortex elements in the BEM);
- performing a broad parametric study of critical accumulation failure modes with validation of computational results by comparison to experimental results; and
- a tentative optimization of boom/barrier systems by varying geometrical and physical parameters of the problem.

To give an idea of future problems addressed in this study, Fig. 5.1 illustrates computations involving a solid boom and an oil slick. These computations had physical parameter values similar to those for the case in Fig. 4.7, with the addition of harmonic "noise", superimposed on the interfacial motion, to represent ocean wave action. Although these computations were performed with the Phase I model, i.e., without both the accurate slick initialization and the numerical improvements planned for the Phase II model, one can see that we obtain quite a realistic picture of interfacial instabilities such as those observed in laboratory experiments (see Chapter 1), namely, the occurrence of both a headwave and interfacial waves propagating along the oil-water interface and reflecting off the boom.

Acknowledgments

This work was supported by the U.S. Department of Transportation Grant No. DTRS-5794-G-00076 under the Oil Pollution Research Grant Program. The able assistance of John Putukian, Volpe National Transportation Systems Center, Boston, Massachusetts, contracting officer's representative, and the enthusiastic support of Ken Bitting, U.S. Coast Guard R&D Center, Groton, Connecticut, are gratefully acknowledged. Andrie Chen, Exxon Production Research, Houston, Texas, served as an industrial technical advisor to the project.

Bibliography

[1] Agrawal, R. K. and Hale, L. A. 'A new criteria for predicting head wave instability of an oil slick by a barrier', *Offshore Technology Conference,* 461-466, 1974.

[2] Bai, K. J. and Kim, J. W. 'A computational model for flow around an oil boom', *Proc. Workshop on Tidal and Oil Spill Modeling,* 5-17, 1993.

[3] Batchelor, G. K. , *An introduction to fluid dynamics* Cambridge University Press, 1967.

[4] Benjamin, T. B. 'Gravity currents and related phenomena', *J. Fluid Mech.* **31** (2), 209-248, 1968.

[5] Brebbia, C. A. , *The Boundary Elements for Engineers* John Wiley and Sons, 1978.

[6] Clavelle, E. J. and Rowe, R. D. 'Numerical simulation of oil–boom failure by critical accumulation', *Arctic Marine Oil Spill Program Technical Seminar,* 409-418, 1993.

[7] Cross, R. H. and Hoult, D. P. 'Oil booms in tidal currents', *Proceedings of 12th Coastal Engineering Conference, ASCE,* 1745-1758, 1970.

[8] Delvigne, G.A.L. 'Barrier failure by critical accumulation of viscous oil', *Proc. Oil Spill Conf.,* USEPA, USCG, and American Petrolium Institute, 143-148, 1989.

[9] Di Pietro, N. D. and Cox, R. G. 'The containment of an oil slick by a boom placed across a uniform stream', *J. Fluid Mech.* **96,** 613-640, 1980.

[10] Drazin, P. G. 'Kelvin-Helmholtz instability of finite amplitude', *J. Fluid Mech.* **42,** 321-335, 1970.

[11] Drazin, P. G. and Howard, L. N. 'Hydrodynamic stability of parallel flow of inviscid fluid', *Advanc. Applied Mech.,* **9,** 1, 1966.

[12] Fink, P. T. and Soh, W. K. 'Calculation of vortex sheets in unsteady flow and application in ship hydrodynamics', *Proc. 10th Symp. on Naval Hydrodynamics* (Office of Naval Research, Washington, D.C.), 463-491, 1974.

[13] Grilli, S. and Subramanya, R. 'Recent Advances in the BEM Modelling of Nonlinear Water Waves'. Chapter 4 in *Boundary Element Applications in Fluid Mechanics* (ed. H. Power), pps. 91-122. Advances in Fluid Mechanics Series. Computational Mechanics Publication, Southampton, UK, 1995.

[14] Grilli, S. and Subramanya, R. 'Numerical Modeling of Wave Breaking Induced by Fixed or Moving Boundaries.' *Computational Mechanics* **17** (in press), 1996.

[15] Johnston, A. J., Fitzmaurice, M. R. and Watt, R. G. M. 'Oil spill containment : viscous oils', *Proc. 1993, Oil Spill Conference,* 89-94, 1993.

[16] Jones, W. T. 'Instability at an interface between oil and flowing water', *J. of Basic Engng.,* **94,** 874-878, 1972.

[17] Kordyban, E. 'The behavior of the oil-water interface at a planar boom', *J. of Energy Resources Technology.* **112** 90-95, 1990.

[18] Lamb, H. *Hydrodynamics* Cambridge University Press, 6th edition, 1932.

[19] Lau, Y. L. and Moir, J. 'Booms used for oil slick control', *J. Envir. Engng.,* **105,** 369-382, 1973.

[20] Lau, Y. L. and Kirchifer, S. A. 'A review of the dynamics of contained oil slicks in flowing water', *J. Hydraul.,* 1974.

[21] Leibovich, S. 'Oil slick instability and the entrainment failure of oil containment booms', *J. Fluids Engng.* **98,** 98-105, 1976.

[22] Milgram, J. H. and Van Houten, R. J. 'Mechanics of a restrained layer of floating oil above a water current', *J. Hydronautics.* **12,** 93-108, 1978.

[23] Moore, D. W. 'A numerical study of the roll-up of a finite vortex sheet', *J. Fluid Mech.* **63** (2), 225-235, 1974.

[24] Rangel, R. H. and Sirignano, W. A. 'Nonlinear growth of Kelvin-Helmholtz instability : Effect of surface tension and density ratio', *Phys. of Fluids.* **31** (7),1845-1855, 1988.

[25] Rangel, R. H. and Sirignano, W. A. 'The linear and nonlinear shear instability of a fluid sheet', *Phys. of Fluids.* **A 3** (10), 2392-2400, 1991.

[26] Robbins, R. J., Hoult, D. and Cross, R. 'Steady state profile for oil barriers', *J. Waterways Harbors and Coastal Engng.,* **97,** 235-238, 1971.

[27] Rottman, J. W. and Olfe, D.B. 'Comment on "discretized simulation of vortex sheet evolution with buoyancy and surface tension effects" ', *J. AIAA* **15**, 1214-1215, 1977.

[28] Song, M., Huh, K. S., Yang, J. Y. and Hyun, B. S. 'Experimental investigation of the evolution of contained oil slick in currents', *Proceedings unknown,* 189–199, 1993.

[29] Subramanya, R. and Grilli, S. 'The state-of-the-art in current-slick interaction' *USCG-FY94, Oil Pollution Research Grant Program* 1st. Quarterly Report, 1994.

[30] Van de Vooren, A. I. 'Numerical investigation of the rolling-up of vortex sheets', *Proc. R. Soc. Lond.* **A 373**, 67-91, 1980.

[31] Von Karman T., *Bull. Am. Math. Soc.* **46**, 615-586, 1940.

[32] Wei, J., Kirby, J.T, Grilli, S.T. and Subramanya, R. 'A Fully Nonlinear Boussinesq Model for Surface Waves. Part1. Highly Nonlinear Unsteady Waves.' *J. Fluid Mech.* **294,** 71-92, 1995.

[33] Wicks, M. 'Fluid dynamics of floating oil containment by mechanical barriers in the presence of water currents', *Proc. API-FWPCA Joint Conf. on Prevention and Control of Oil Spills,* New York, Dec 15-17, 55-106, 1969.

[34] Wilkinson, D. L. 'Dynamics of contained oil slicks', *J. Hydraulic Division,* **HY6,** 1013-1031, 1972.

[35] Wilkinson, D. L. 'Limitations to length of contained oil slicks', *J. Hydraulic Division,* **HY5,** 701-713, 1973.

[36] Zalosh, R. G. 'A numerical model of droplet entrainment from a contained oil slick', *Report No.* **CG-D-65-75**, DOT/USCG, 1974.

[37] Zalosh, R. G. 'Discretized simulation of vortex sheet evolution with buoyancy and surface tension effects', *J. AIAA* **14**, 1517-1523, 1976.

[38] Zalosh, R. G. and Jensen, D. S. 'A numerical model of droplet entrainment from a contained oil slick', *Proc. Fluid Mech. in Petrolium Industry* ASME, 17-27, 1975.

[39] Zaroodny, S. J. and Greenberg, M. D. 'On a vortex sheet approach to the numerical calculation of water waves', *J. Comp. Phys.* **11**, 440-446, 1973.